Numerical and Physical Modeling of Cone Penetration in Unsaturated Soils and Numerical

Simulation of Fracture Propagation in Shale Rock during Brazilian Test

BY

Pegah Jarast Shamsabadi

B.Sc. Isfahan University of Technology, 2009

M.Sc. Isfahan University of Technology, 2012

DISSERTATION

Submitted to the University of New Hampshire

in Partial Fulfillment of

the Requirements for the Degree of

Doctor of Philosophy

In

Civil Engineering

September, 2017

ProQuest Number: 10622976

ProQuest 10622976

This dissertation has been examined and approved in partial fulfillment of the

requirements for the degree of Doctor of Philosophy in Civil Engineering by:

Dissertation Director, Dr. Majid Ghayoomi
Assistant Professor of Civil and Environmental Engineering

Dr. Jean Benoit
Professor of Civil and Environmental Engineering

Dr. Eshan Dave
Assistant Professor of Civil and Environmental Engineering

Dr. Ehsan Ghazanfari
Assistant Professor of Civil and Environmental Engineering
University of Vermont

Dr. Pania Newell
Assistant Professor of Mechanical Engineering
University of Utah

On August 1, 2017.

Original approval signatures are on file with the University of New Hampshire Graduate School.

Dedication

To my Parents, specially my mother, Tahmineh, for her unlimited love.

To my Brother, Pezhman, for his heartfelt support and love

To my kindhearted mentor, Dr. Rouzbeh Yassini, for showing me how to become the greatest I can.

Acknowledgment

I would like to express my immense gratitude to my advisor Dr. Majid Ghayoomi for all his contributions of time, ideas, and funding along these 4 years of my Ph.D. study. His comments and suggestions during development of this research are deeply appreciated

I also have to thank the members of my PhD committee Dr. Jean Benoit, Dr. Eshan Dave, Dr. Ehsan Ghazanfari, and Dr. Pania Newell and also Dr. Hongkyu Yoon from Sandia for their time, support and suggestion which helped me in improvement of my research.

I would like to thank my classmates, Morteza Mirshekari and Amin Borghei for his help and assistance in performing experimental tests as a part of this work.

I would like also like to acknowledge James Abare, John Ahern, Scott Campbell and Kevan Carpenter, for their assistance with the electrical, mechanical, and technical knowledge and contributions to the project.

Additionally, I would also like to thank my friends specially Reyhaneh Rahbar, Afshin Benkaran for their encouragement and friendship which would never be forgotten:

Lastly, I would like to thank my phenomenal family specially my mother and also Dr. Yassini for providing me the much needed support, encouragement, and affection to complete this challenging endeavor.

Table of content

List of Tables

List of Figures

xiii

Abstract

Numerical and Physical Modeling of Cone Penetration in Unsaturated
Soils and Numerical Simulation of Fracture Propagation in Shale
Rock during Brazilian test

By

Pegah Jarast
University of New Hampshire, September 2017

Partially water saturated condition in soils may change the cone penetration resistance comparing with that of dry or saturated conditions. This effect was investigated in this study using numerical finite element modeling and experimental centrifuge testing. The results showed suction in unsaturated soil significantly influenced the soil resistance to cone penetration. Two approaches were implemented to numerically consider the partially saturated soil condition; i.e. modifying simple constitutive models using an apparent cohesion strategy and implementing Barcelona Basic Model for unsaturated soils. Both successfully captured the cone resistance profiles inside a calibration chamber and also in free field. In addition, details of developing a miniature cone set-up capable of for cone penetration inside geotechnical centrifuge was explained. Further, the use of Linear Softening Cohesive Model (LCFM) to predict the fracture growth in shale rocks during Brazilian Test was examined. The application and importance of considering two different compressive and tensile elastic modulus and soil anisotropy during the fracture modeling of shales were demonstrated.

Chapter I

Introduction

1.1 Research Overview

This thesis comprises of two independent research objectives: (I) The effect of degree of water saturation on cone penetration resistance in dry, saturated, and unsaturated soils both using numerical and physical modeling strategies was investigated. Unsaturated soils are widespread throughout the world, especially in surficial parts of the earth and above the water table. Engineers need to deal with unsaturated soils in many geotechnical projects including foundations, fills, embankment, dams, pavements, slopes and landfills. Given the importance of Cone Penetration Testing (CPT) in geotechnical engineering practice it is crucial to understand how water level in soils would affect the penetration resistance. (II) The fracture development in shale rocks during Brazilian Test was numerically simulated. Acquiring a clear understanding of the rock failure mechanism is a key step in addressing many rock engineering problems such as rock cutting, blasting, oil and gas production, geothermal systems, hydraulic fracturing, safety of nuclear waste repositories and geological carbon storage units. This research will pave the path towards better models in predicting the long-term structural performance of various geological systems.

1.2   Dissertation Outline

The thesis starts with research motivations and objectives of investigating cone penetration in unsaturated soils in Chapter 2. A review of literature related to this topic is presented in Chapter 3. It covers the basic concepts of unsaturated soil. The effective stress in partially saturated soils is explained followed by a review of numerical approaches in modeling the unsaturated soils. Then, the experimental technique to control the degree of saturation in calibration chamber and centrifuge is explained and the effect of unsaturated soil condition on CPT results using both numerical and centrifuge modeling is briefly discussed. In Chapter 4, details of numerical modeling, including material constitutive models, contact model, loading and remeshing methods are reviewed followed by the results of the study. In Chapter 5, details of development of miniature piezocone set-up for cone penetration testing in centrifuge is explained. It is followed by presenting the piezocone specifications and calibration procedures. Chapter 6 covers the sample preparation steps and test procedures while in Chapter 7, results of penetration tests in different conditions, including dry, saturated and unsaturated, are presented and discussed. A summary of the procedure and the findings of this investigation are discussed in Chapter 8.

The second part of the thesis starts with Chapter 9 where the research motivations and objectives of investigating shale rock fracture are discussed. A review of literature related to this topic is presented in Chapter 10. It covers the basic concepts of rock fracture and available fracture models for numerical simulation. In addition, Brazilian test and a review of numerical approaches in order to investigate the effect of different parameters are presented as well. In chapter 11, details of experimental Brazilian tests, results of which used for calibration and validation of numerical model, are explained. It includes the rock samples properties, layer identification and experimental Brazilian test results. In Chapter 12, details of numerical modeling, including model geometry,

material constitutive models, mesh properties and loading are reviewed followed by the results of numerical simulation. A summary of the procedure, the findings of this investigation and recommendations for future work are discussed in Chapter 13.

Finally the references used in this dissertation are presented in Chapter 14; alphabetically ordered while separated for the two different research topics.

Numerical and Physical Modeling of Cone Penetration in Unsaturated Soils

Chapter II

Cone Penetration in Unsaturated Soils: Motivation and Approach

2.1 Research Motivation

Unsaturated soils are widespread throughout the world, especially in surficial parts of the earth and above the water table. Engineers need to deal with unsaturated soils in many geotechnical projects including foundations, fills, embankment, dams, pavements, slopes and landfills. The behavior of unsaturated soils is complex and differs from that of dry or saturated conditions. It is influenced by several factors such as stress state, soil type, soil fabric, mineralogy, density, and most importantly, inter-particle suction stresses within the pore space due to the surface tension across air-water interface (Loret and Khalili 2002). Suction increases the effective stress acting on the soil and alters strength and stiffness of geomaterial (Lu and Likos 2006; Ghayoomi and McCartney 2011). Characterization of unsaturated soils has been a challenging task due to the difficulties in testing soils under suction-controlled environments. Thus, recent studies have mainly focused on small-scale laboratory experimentation, which left a gap in fundamental understanding of unsaturated soil behavior, especially in field testing applications or scaled model systems.

Cone Penetration Testing (CPT) is one of the popular field investigation methods to evaluate the physical and mechanical properties of soils. There are many mechanics-based or

5

empirical correlations that link the measured cone resistance (q_c) and sleeve resistance (f_s) to soil properties such as density, shear strength, stiffness, in situ stress state, and soil dynamic properties (Schmertmann 1978, Baldi et al. 1982; Robertson and Campanella 1983; Been et al. 1986; Jamiolkowski et al. 2001). Also, with the use of piezocones (CPTu), it is possible to measure the induced excess pore water pressure (u) to correct the test results and estimate the hydraulic conductivity through dissipation tests (Keaveny and Mitchell 1986; Jamiolkowski et al. 2003). CPT results (q_c, f_s) are in fact controlled by soil shear strength, stiffness, compressibility, and permeability (Robertson 2009). Suction stresses can be significant in unsaturated soils and influence CPT results directly or indirectly by changing the effective stress, and in turn, affecting the cone resistance (Hryciw and Dowding 1987; Lehane et al. 2004; Russell and Khalili 2006b). However, there is an absence of correlations for the CPT that takes into account the effect of unsaturated condition which may lead to misrepresentation of soil properties and requires further scrutiny.

Numerical simulation of the cone penetration process is complex because of large deformations in the model and severe mesh distortion. There have been attempts to model cone penetration numerically, all of which involved challenges both in mesh generation and solution schemes (Kiousis et al. 1988; van den Berg 1994; Markauskas et al. 2002; Susila & Hryciw 2003; Huang et al. 2004; Ahmadi et al. 2005; Nazem et al. 2006; Sheng et al. 2009; Yi et al. 2012; Kouretzis et al. 2014). In all previous studies, simulations were limited to dry or saturated soil conditions. Thus, implementing an appropriate numerical technique to model cone penetration in unsaturated soil requires further examination. In the numerical part of this research, a Finite Element model was developed to model the cone penetration in unsaturated soils. Two different

approaches including modification of a standard constitutive relation and implementing an elastoplastic constitutive model were used to model the unsaturated condition in the soil.

Centrifuge testing is a powerful technique to model many geotechnical problems. In several studies miniature cones have been used to investigate the effect of different parameters on CPT results such as container size, boundary condition, penetration rate (Corte et al. 1991; Bolton et al. 1999; Balachowski 2007; Liu and Lehane 2012). Other studies were also performed to investigate the effect of soil layering on CPT results and the efficiency of using CPT results to predict the liquefaction or lateral response of the soil (Silva and Bolton 2004; Sharp et al. 2010; El-Sekelly et al 2014). However, none of the previous studies have been focused on the effect of unsaturated condition on CPT results which is the focus of experimental part of this research.

2.2 Research Objectives/ Approach

The objective of this research is to investigate the effect of unsaturated soil condition on CPT results. This study consists of both numerical modelling and centrifuge testing.

In the numerical part, a finite element model was developed using Abaqus/Explicit simulating the cone penetration process in soil inside a calibration chamber. The unsaturated condition was considered using two different approaches: incorporating an apparent cohesion in standard constitutive relations and implementing an elastoplastic constitutive model for unsaturated soils. After proving the efficiency of the modified constitutive model to incorporate the unsaturated condition by comparing the results with experimental data in the literature, the study was extended by simulating the cone penetration in a free-field soil layer inside a centrifuge with various ground water levels. In this case, material parameters were updated according to the initial stress state and suction profile in depth using a user-material subroutine (UMAT).

Accordingly, a new miniature piezocone was designed, built and calibrated to be used for penetration tests on partially saturated soils. The miniature piezocone is capable of measuring the cone tip resistance, sleeve friction and pore water pressure. The performance of the miniature cone during penetration tests in dry, saturated and unsaturated condition was examined and the challenges for the appropriate performance of the miniature cone set up was discussed.

Synthesizing the results from numerical and experimental models will help the understanding of the behavior of unsaturated soil during penetration.

Chapter III

Cone Penetration in Unsaturated Soils: Background

3.1   **Unsaturated Soils**

The ground water location is formed based on the difference between downward and upward flux of water and is influenced by changes of climate. Soil layer underneath the ground can be divided into two zones with regards to the water table; saturated and unsaturated zone. Figure 3.1 shows the profile of saturated and unsaturated zones in the hydrologic cycle. The pore water pressure is negative in unsaturated zone and degree of saturation can vary between 0 and 100%. Unsaturated condition can exists in other situations such as soils with equal evaporation and precipitation or dried soil due to taking up of water by plants. Figure 3.2 shows the change of degree of saturation and pore water pressure through the soil profile.

A representative element of soil volume consists of solid particles, water and air. Three groups of forces can be considered within the soil (Lu and Likos, 2016):

- Skeletal forces (active forces between soil grains)

- Local forces (active forces concentrated at the inter-particle contacts)

- Passive particle contact forces that counterbalance the first two groups of active forces.

In saturated soil, the local forces include van der Waals attraction, electrical double-layer repulsion and net attraction at the grain contacts due to chemical cementation. In unsaturated soil, attractive forces and surface tension at air-water interface can be created by negative pore water pressure in addition to physiochemical forces (Lu and Likos 2006). These forces act in different phases of the soil element:

- Water pressure which acts on wetted areas of the soil

- Air pressure which acts on dry portions of the soil grains

- Surface tension which acts in air-water interface

The magnitude of the tensile strength is different for different soil types as it is inversely proportional to the diameter of particle (Lu 2007). So, for fine grained soil, tensile stress can be several kilo-Pascals while for coarse grained soil, it is only tens of Pascals.

Combined effects of particle-pore water interaction (attractive forces) and capillary forces (Surface tension at air-water interface) is called matric suction which is, in other word, the difference in air pore pressure and pore water pressure $(u_a - u_w)$. In addition to matric suction, solutes that can be dissolved in water can produce suction which is called "Osmotic suction". However, in common geotechnical engineering problems, the changes in osmotic suction are almost negligible comparing to the matric suction and changes of matric suction are considered to be equal to the total suction change.
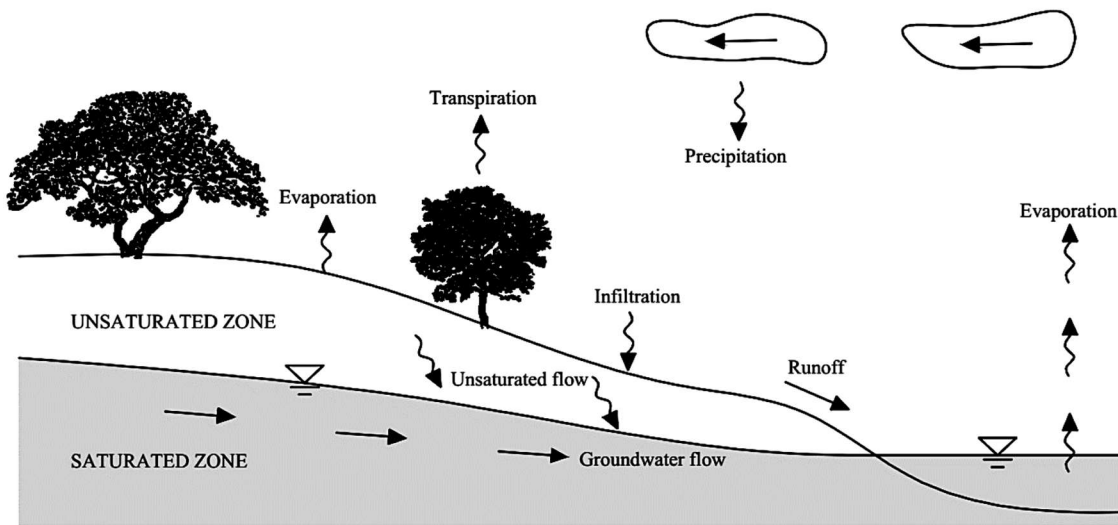
Figure 3-1 Saturated and unsaturated soil profile zone in the hydrologic cycle (Lu and Likos 2004)
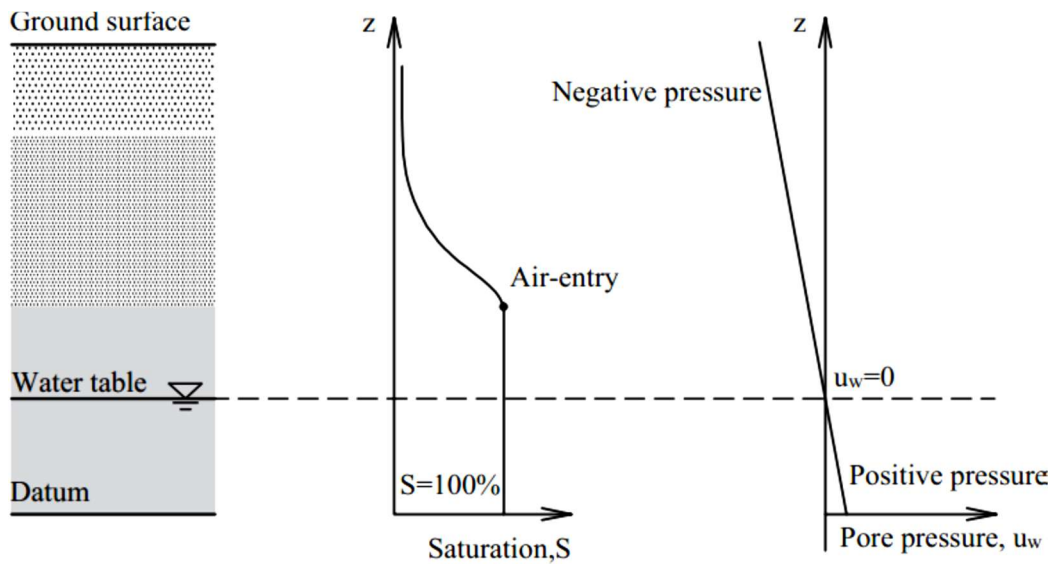
Figure 3-2 Degree of saturation and pore pressure profile for unsaturated soil zone (After Lu and Likos, 2004)

3.2 Soil-Water Characteristic Curve

As explained in the previous section, suction in unsaturated soil is related to physical and physicochemical forces which are influenced by the soil water content. Soil Water Characteristic Curve (SECC) or Soil Water Retention Curve (SWRC) show the relation between the soil water content and matric suction. SWRCs can be determined using different methods and devices including hanging Column, Pressure Extractor, Chilled Mirror Hygrometer, or Centrifuge methods (ASTM D 6836-02). Figure 3.3 shows a schematic SWRC curve of a soil. It is actually a hysteresis loop which describes wetting and drying process of the soil sample. Based on this curve, in drying process (ex. evaporation and drainage), soil tends to retain more water than that of the same suction level under a wetting process (ex. capillary rise or infiltration). This hysteresis behavior is a result of inter-particle mechanisms that happen in the soil which are related to nonhomogeneous pore size distribution, swelling and shrinkage in fine grained soil or entrapped air.
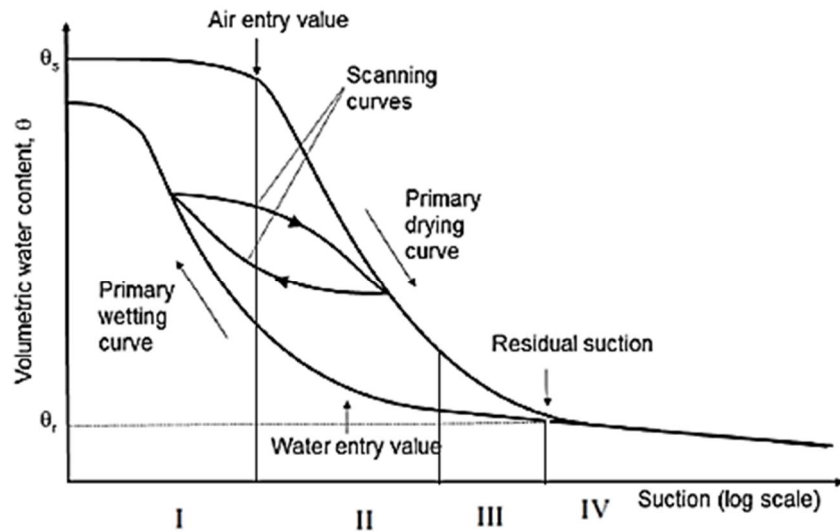
Figure 3-3 Schematic of soil-water characteristics soil (after Lu and Likos 2006)

The shape of SWRC is affected by soil properties such as density, pore size and grain size distribution, mineralogy and clay content and it could be divided into four regimes as it is shown in Figure 3.3.

In regime I, soil remains saturated regardless of the negative pore pressure and it could be considered as an equivalent continuum medium. The upper boundary of this zone is known as air-entry pressure and it shows the maximum matric suction that soil can stand while saturated.

In regime II, water in soil pores is mostly controlled by capillary forces and there is a rapid reduction of water content under increasing suction which is affected by pore size and pore size distribution of soil.

Regime III represents when the water decrease to the small film at the surface of particles.

And, regime IV is known as "Residual" regime and represent small amount of pore water that is held as hydration of soil particles. In this regime, large increase in matric suction would not result in significant water content change. For coarse-grained soils, this water can be extracted only under high temperature, e.g. drying the soil sample in oven. However, this method would not remove water in fine grained soil.

3.3 Effective stress in unsaturated soils

The stress state of unsaturated soil is different than dry or saturated soil as the soil element consists of three phases: solid, water and air despite the saturated soil which only consists of the first two phases. Two most known approaches to explain the stress state in unsaturated soils are: (1) Modified effective stress approach, which is developed based on the work of Bishop (1959); (2) Two stress state variable approach, which is originated by Fredlund and Morgenstern (1977).

In modified effective stress approach, the matric suction and net stress are combined and as a result, a single effective stress is required to characterize the behavior of unsaturated soil.

13

Equation 3.1 shows the Bishop's effective stress approach which is a modified version of Terzaghi's classic effective stress.

$$\sigma' = \sigma - u_a + \chi(u_a - u_w) \qquad\qquad Eq.\,3.1$$

Where, u_a is the air pressure, u_w is the water pressure, $\sigma - u_a$ is net normal stress and $(u_a - u_w)$ is matric suction and χ is the effective stress parameter which is a function of the degree of saturation and varies between zero and one. It is equal to zero in case of completely dry soil, while it is 1 for fully saturated soil. Several equations are suggested in order to estimate the effective stress parameter, χ, describing the dependency of the effective stress parameter, χ, on degree of saturation (Khalili and Khabbaz 1998, Vanapalli and Fredlund 200, Loret and Khalili 2002, Lu and Likos 2006, Russell and Khalili 2006a).

In two stress state variable approach, the net stress and matric suction are defined as independent variables for which different conjugate material properties are evaluated in order to describe the macroscopic behavior of soil. For example, shear strength maybe described as:

$$\tau_f = c' + (\sigma - u_a)tan\varphi' + (u_a - u_w)\tan\varphi^b \qquad\qquad Eq.\ 3.2$$

In which $\emptyset^b$ is an additional friction angle to capture the contribution of matric suction to shear strength.

In recent years, the effective stress approach gained more attention due to its advantages over the two stress state approach. Superiority of this approach is that a single variable, effective stress, is required to describe the soil behavior comparing to two stress variable approach in which two variables, net stress and matric suction, are required. So, it is easier and less time consuming to evaluate the soil properties in terms of effective stress rather than two independent stress variables from laboratory results.

There are studies which have been done to include the behavior of unsaturated soils in constitutive materials based on both approaches. For instance, Alonso et al (1990) included the volumetric strain due to matric suction in critical state framework. Cui and Delage (1996) presented a model for compacted silt in which the size of the yield surface was a function of matric suction as an independent variable. Loret and Khalili (2002) developed a model using conventional plasticity theory and the effective stress approach in which suction was combined with mean net stress. In addition, the effective stress and the isotropic hardening was assumed to occur due to suction changes as well as plastic volumetric strains. Gallipoli et al (2003), also considered a stress variable in elastic-plastic analysis which depends on both the degree of saturation and matric suction.

3.4   Effect of Partial Saturation on CPT Results

Recent studies on cone resistance in unsaturated soils revealed that suction may change the cone penetration response significantly. For example, based on CPTs in sands, Hryciw & Dowding (1987) and Lehane et al. (2004) reported that cone resistance (q_c) in an unsaturated soil condition can be increased up to two times compared with the resistance in dry and saturated soils under certain circumstances. Later, Vanapoli & Fathi (2013) conducted several CPTs in a specially designed tank and demonstrated a meaningful influence of suction on cone resistance and bearing capacity of sand. Russell and Khalili (2006) also showed that the pressure required to expand a spherical cavity in an infinite sand mass is related to cone penetration resistance, and it could be increased in an unsaturated condition due to the presence of suction. Later, Pournagiazar et al. (2013) conducted CPTs in saturated and unsaturated sands in a suction-controlled calibration chamber. They developed a semi-analytical procedure to convert the penetration resistance measured in the calibration chamber to equivalent field values based on a solution for spherical

cavity expansion in soils of finite radial extent considering the effect of chamber size and boundary conditions (Pournaghiazar et al. 2012). In addition, based on their results, the effect of suction is more significant in soils with low relative density and under low chamber confining stress. This emphasizes the importance of suction in cone penetration into the shallow ground where soils are mostly unsaturated. An expression was developed in which the effect of suction was considered in an empirical resistance formula. Thus, more accurate relative density and friction angle values could be estimated for an unsaturated soil, given the suction-dependency of cone resistance. Recent laboratory suction-controlled CPT results in unsaturated silty sand with hardening suction conducted by Yang and Russell (2016) and site CPT data by Holmsgaard et al. (2016) were also showed the meaningful influence of suction on the measured cone resistance.

3.5   Numerical Modeling of CPT

Numerical simulation of the cone penetration process is complex because of large deformations in the model and sever mesh distortion. There have been attempts to model cone penetration numerically, all of which involved challenges both in mesh generation and solution schemes. As one of the first attempts, Kiousis et al. (1988) modeled the cone penetration test considering artificial node relocation technique. Later, van den Berg (1994) combined interface elements with an Eulerian formulation to model a volume of soil mass passing by a fixed cone. Although this approach avoided mesh distortion, it was not able to track material history and material flow at the boundaries. Markauskas et al. (2002) used small strain finite element method that didn't allow reaching limit load during cone penetration, thus, it could not adequately describe the stress-strain state around the cone tip. Susila & Hryciw (2003) used an auto adaptive meshing technique to model the problem more accurately. Their results show soil-cone separation and oscillation anʲd unrealistic values for sleeve friction. Also, the constitutive model used in their

16

study increased cohesion as a result of increased plastic strain which is not an observed behavior in sand. Huang et al. (2004) simulated the penetration problem using the auto adaptive remeshing method and a frictional model (elastic stick-plastic slip) based on penalty method. The results were highly dependent on allowable plastic slip limit and caused some doubts. Ahmadi et al. (2005) used the large strain finite difference method without remeshing. The instability was avoided in their model by using a small central cavity and applying artificial nodal displacement. However, this approach was not capable of modeling the friction at interfaces. Later, Nazem et al. (2006), Sheng et al. (2009), Yi et al. (2012), Kouretzis et al. (2014), and Jarast and Ghayoomi (2016) used Arbitrary Lagrangian-Eulerian (ALE) method to overcome the mesh distortion in numerical modeling of penetration problems in soils. Thus far, this technique combined with adaptive remeshing has been the most successful approach and showed the most stable responses.

Also, few studies have been carried out using Discrete Element Method (DEM) for modeling CPT in granular soils (Huang and Ma 1994; Calvetti and Nova 2005; Jiang et al 2006; Butlanska et al 2010; Arroyo et al. 2011; Falagush et al. 2015; Butlanska et al. 2014). These studies mainly focused on investigating the effects of particle shape, particle crushing, and radial boundary condition on cone tip resistance. For instance, Butlanska et al (2014) developed a 3D discrete element model and examined the mesoscale and microscale effects of radial boundary conditions, initial stress state, and initial average density on cone penetration response. Falagush et al. (2015) showed that prohibiting particle rotation increases the tip resistance while permitting particle crushing (by replacing a broken particle with two new equal-sized smaller particles) considerably reduces the cone tip resistance.

In all previous studies, simulations were limited to dry or saturated soil conditions. Thus, implementing an appropriate numerical technique to model cone penetration in unsaturated soil requires further examination.

3.6   Suction Control Techniques

There are different methods of controlling suction in the soil. Axis-translation technique used in the calibration chamber tests borrowed for this study and the steady state infiltration which was used in the centrifuge testing are explained briefly.

3.6.1   Axis-translation technique

Axis-translation technique (Hilf 1956) is one of the popular techniques to determine or apply suction to the soil specimen in laboratory. Figure 3.4 shows the concepts of this method. In this method, the soil sample is placed over a high air-entry value disk (HAEV disc) which is previously saturated. The HAEV disk acts as an interface that separates air and water phases up to the air entry value of disk. In fact this value refers to the maximum matric suction that can be subjected to the disk before free air passes through the disk. Then, the sample is allowed to be saturated by opening the inlet valve and letting the water flow into the soil. When the water reached some height above the soil sample, the water is allowed to follow out by opening the outlet valves until the water table is reached to the top of the soil sample and a saturated sample is achieved. Then the air pressure is increased to the desired value from top of the sample which causes the water to be drained to reach the equilibrium. The equilibration time depends on type of soil, size of specimen and air-entry value of the disk.
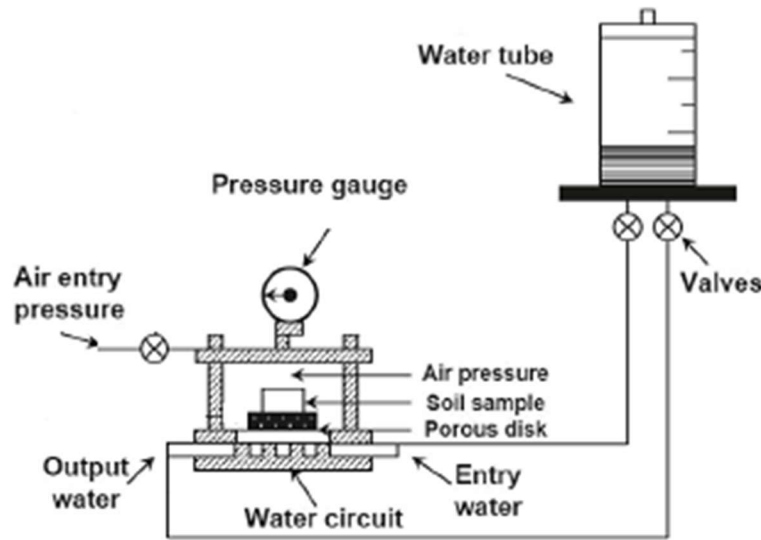
Figure 3-4 Schematic of Axis-translation technique (Norambuena-Contreras 2015)

3.6.2 Steady State Infiltration

Infiltration technique can be used in order to produce a profile of matric suction with height in the soil layer. This method is referred to as the Drainage-Recharge Method (Yegian et al. 2007) or the Steady State Infiltration Method (McCartney and Zornberg 2010). Figure 3.5 shows the schematic set up of an infiltration system. During the steady state infiltration process in the geotechnical centrifuge, at first, the soil specimen is saturated by letting the water flow into the soil from the bottom. Then, the saturated specimen is allowed to be drained by opening the drainage line at the bottom of the specimen. In the next step, water from a pressurized storage tank is sprayed uniformly onto the upper surface of the soil through a series of fine-mist spray nozzles and drained from the drainage line at the bottom. The changes in volumetric water content in the soil layer can be measured using dielectric moisture probes which are placed horizontally at different depth to check the degree of saturation profile. Pore pressure sensors can be also embedded to measure suction in depth. Imposing different infiltration rates, different uniform

degree of saturation profiles can be achieved in the soil depth. The detail of instrumentation and procedure is explained in chapter 5.
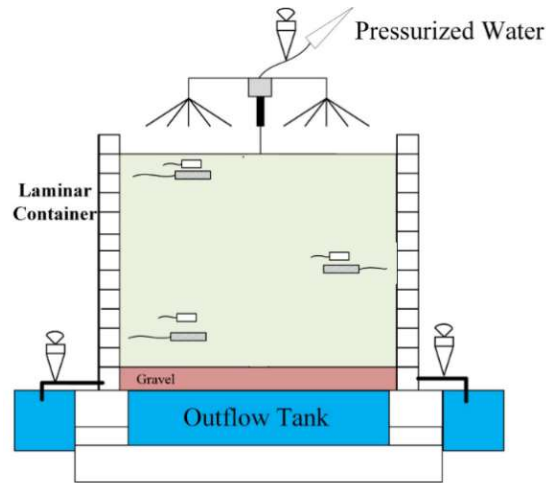
Figure 3-5 Conceptual schematic of infiltration system

3.7 Miniature cone application in geotechnical centrifuge

Centrifuge testing is a powerful technique to model many geotechnical problems. In many of these tests, having an estimation of cone penetration resistance profile is necessary to characterize the soil and link with field data. In addition, CPT profiles can be used in order to check the uniformity and repeatability of the specimen. In order to have reliable data, the effect of different parameters on CPT results such as container size, boundary condition, and penetration rate should be investigated which is the subject of many researches.

Esquivel and Ko (1994) developed a miniature piezocone for centrifuge testing at University of Colorado at Boulder. The cone was 12.7 mm in diameter and 305 mm in length and was capable of measuring tip and total resistance and water pressure. A porous stone with pore size of 5 μm was used as filter and glycerin was used as saturating fluid. Tests were performed on soft clay specimens at the rate of 20 mm/s and results were compared with vane shear tests.

Bolton et al. (1999) analyzed the results of CPTs performed on very dense sand with three different diameter mini-cones (19 mm, 10 mm and 6.35 mm) in five European centrifuge centers: Cambridge University Engineering Department (CUED); the Technical University of Denmark (DIA); the Instituto Sperimentale Modelli e Strutture (ISMES); the Laboratoire Central des Ponts et Chaussees (LCPC); and Ruhr-Universitat (RUB), and showed that no scale effect on cone resistance was found for medium and coarse sand when the ratio of size of the model to the average grain size (B/d50) is higher than 20.

Silva & Bolton 2004 performed piezocone penetration tests in saturated layered sands to investigate the sensitivity of penetration resistance to layering and grain size. A 12 mm diameter piezocone capable of measuring the tip resistance, sleeve friction and pore water pressure was used and tests were performed at centrifuge acceleration of 50 and penetration rates between 0.4 to 8 mm/s and cone was stopped at 10 cm above the bottom of the sample to avoid the base boundary effect (Lee, 1989).

Balachowski (2007) performed CPTs with a 12 mm mini-cone in L.C.P.C. centrifuge at 30g, 60g and 100g in two uniform quartz sands of different grain size to analyze the effect of particle size and stress level on the cone resistance. The results showed an additional increase in cone resistance when (B/d_{50}) falls below 17.

Sharp et al. 2010 performed Centrifuge tests at Rensselaer Polytechnic Institute to evaluate the liquefaction and lateral spreading response. Different cones with diameters of 4, 8, and 12 mm were used which were capable of measuring the cone tip resistance but not the sleeve friction or pore pressure. The tests were performed at different centrifuge accelerations of 3 to 9g and penetration rate of 0.5 to 10 mm/s. Results showed that the measured cone tip resistance could

predict the liquefaction and lateral spreading response well and confirm the penetration-based seismic liquefaction charts.

Liu and Lehane (2012) examined the effect of particle shape on cone resistance by performing CPTs on different silica materials using a 5 mm miniature cone at different g-levels of 50, 100 and 200. Results shows the particle shape has a significant effect on cone resistance and revised expressions for estimating the friction angle based on CPT results considering the effect of particle shape should be used.

However, none of the studies have been focused on conducting miniature cone penetration tests on unsaturated soil inside a centrifuge which is the aim of this study.

Chapter IV

Cone Penetration in Unsaturated Soils: Numerical Modeling

4.1 Introduction

The goal of numerical modeling part of this research was to develop a cone penetration model in unsaturated soil. Two approaches were pursued for considering the behavior of unsaturated soil: 1) Modifying a relatively simple constitutive model to incorporate unsaturated soil condition; 2) Adapting Barcelona Basic (Alonso 1990) model which is developed for unsaturated soils. The results from these two methods were compared and the differences were discussed. In order to develop such a numerical model, the following steps were required to be taken:

1. Based on the available triaxial tests and CPT data inside a calibration chamber (CC) from the literature in both saturated and unsaturated conditions from the work of Pournaghiazar (2013), an Abaqus model was developed. The geometry and material properties were selected similar to that of Pournaghiazar (2013) while the two constitutive model strategies were taken into account.

2. The work was extended by developing a model for CPT in Fontainebleau sand inside a centrifuge with different water table levels in which the first material model strategy was

used. The model properties were selected based on the study by Kouretzis et al. (2014) that replicated the centrifuge tests on dry sand carried out by Bolton and Gui (1993) at the Cambridge Geotechnical Centrifuge Center. In addition, the model was improved by updating the material parameters according to the initial stress state and suction profile in depth using a user-material subroutine (UMAT).

4.2 Material models

Two basic material constitutive models, i.e. Mohr-Coulomb (MC) and Drucker-Prager (DP), were chosen for the FEM analysis of the soil. In addition, a Cap-Plasticity (CP) constitutive model for unsaturated soil based on Barcelona Basic (BB) model by Alonso et al. (1990) was adjusted to be used in Abaqus as well. These three models and their implementation procedures are discussed in the following.

4.2.1 Mohr-Coulomb and Drucker-Prager Models

Two very common and well established material models, i.e. MC and DP models, in geotechnical engineering were modified for this study. In order to consider the unsaturated condition in the sand, suction was indirectly incorporated in the base MC and DP models using a relatively simple approach. This method is based on the modified effective stress approach derived from Bishop's (1959) equation by introducing suction stress concept (Lu and Likos 2006). The additional shear strength resulted from suction stress was considered as an apparent cohesion parameter and used as an input in the material constitutive model.

Bishop's effective stress in unsaturated soil is a modified form of Terzaghi's classic effective stress equation and can be written as follows:

$$\sigma' = \sigma - u_a + \chi(u_a - u_w) \qquad\qquad Eq.\,4.1$$

where 'χ' is the effective stress parameter, which is a function of degree of saturation and varies between zero and unity, '$(u_a - u_w)$', also shown a 's' or 'ψ', is the matric suction (i.e. the difference between pore air and pore water pressure), and '$(\sigma - u_a)$' is the net normal stress. In fact, $\chi(u_a - u_w)$, is the contribution of matric suction to the effective stress; so called suction stress (Lu and Likos 2006).

This modified effective stress formula can be used within the established framework of saturated soil mechanics to explain the behavior of unsaturated soil. For example, the Mohr-Coulomb failure criterion can be modified as follows for unsaturated soils (Lu and Likos 2006).

$$\tau_f = c' + [(\sigma - u_a) + \chi(u_a - u_w)] \tan \varphi' \qquad Eq. 4.2$$

where 'c'' is effective soil cohesion and φ' is the effective angle of internal friction. This equation is shown in Figure 4.1. Rewriting this equation, will result in two terms contributing to overall shear strength; i.e. "$c'' = c' + \chi(u_a - u_w) \tan \varphi'$", and "$(\sigma - u_a) \tan \varphi'$". The value of c'' defined as an apparent cohesion can be applied in regular constitutive models alongside the effective friction angle, φ'.
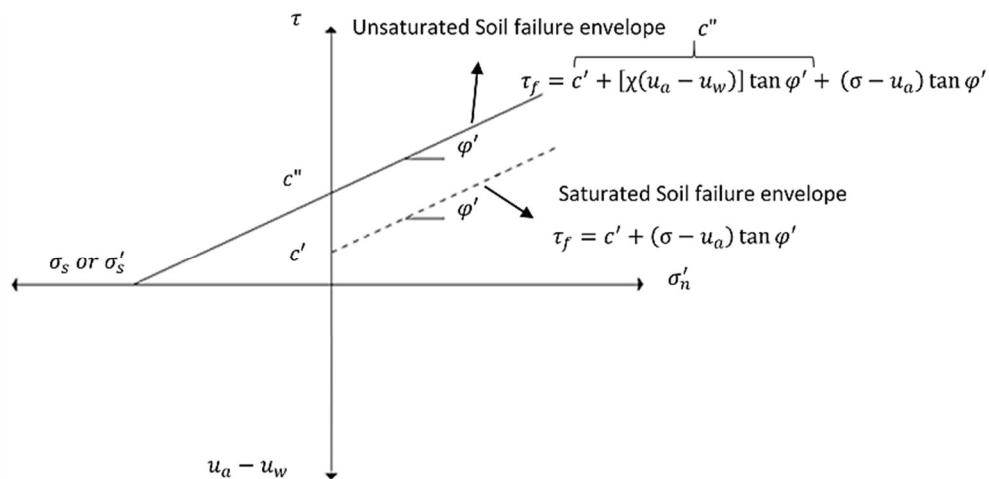
Figure 4-1 Modified Mohr-Coulomb failure criterion for unsaturated soil

Several equations have been suggested in the literature to estimate χ. For example, Lu and Likus (2006) defined χ based on Soil Water Characteristic Curve (SWCC) and Suction Stress Characteristic Curve (SSCC), and associated fitted functions. Similarly, Russell and Khalili (2006a) suggest an expression for χ as follows:

$$\chi = \begin{cases} 1 & for \ \left(s/s_e\right) \leq 1 \\ \left(s/s_e\right)^{-0.55} & for \ 1 \leq \left(s/s_e\right) \leq 25 \\ 25^{0.45}\left(s/s_e\right)^{-1} & for \ \left(s/s_e\right) \geq 25 \end{cases} \qquad Eq.\,4.3$$

where 's_e' is suction value separating saturated from unsaturated states, i.e. the air entry value. This expression was found based on laboratory strength and volume change data where s/s_e ratios were less than 70 for Sydney quartz sand containing no fines and less than 12 for fine grained soils.

Furthermore, it should be mentioned that the soil properties such as elastic modulus can also be influenced by the change of effective stress induced by suction stresses. However, based on sensitivity analyses that were done on the model, it was found that the effect of changes in elastic modulus due to suction stress on the cone resistance is negligible. As a result, the same elastic modulus for both saturated and unsaturated condition was considered in this work.

4.2.2 Barcelona Basic model

Barcelona Basic (BB) model is an elastoplastic constitutive model for unsaturated soils developed by Alonso (1990). The model has been widely used and intended mainly for fine-grained soil, but excluding those containing highly expansive clay minerals. In this model, the mean net stress (p), deviator stress (q), and suction (s), are the state variables. When reaching the saturated condition (s=0), the model converges to a modified cam-clay model (Roscoe and Burland

1968). In this model, the isotropic normal compression lines for different values of suction are defined by:

$$v = N(s) - \lambda(s) \ln\left(\frac{p}{p^c}\right)$$
Eq. 4.4

Where v is specific volume, p^c is a reference pressure (a soil constant) while the intercept $N(s)$(defined at the reference pressure,p^c) and gradient $\lambda(s)$ are both functions of suction, s. The variation of $N(s)$ with suction is presented as:

$$N(s) = N(0) - \kappa_s \ln\left(\frac{s+p_{atm}}{p_{atm}}\right)$$
Eq. 4.5

where $N(0)$ is the value of $N(s)$ at zero suction, κ_s is the elastic stiffness parameter for changes in suction, and p_{atm} is atmospheric pressure.

Also, $\lambda(s)$ can be shown as a function of suction as follows:

$$\lambda(s) = \lambda(0)[r + (1 - r)\exp(-\beta s)]$$
Eq. 4.6

where $\lambda(0)$ is the value of $\lambda(s)$ at zero suction and r and β are two soils constants. This equation shows that $\lambda(s)$ varies from $\lambda(0)$ at zero suction to a limiting value of $r\lambda(0)$ as suction tends to infinity while β controls the rate of exponential approach to this value.

In the model formulation, the elastic volumetric strain increments are given by:

$$d\varepsilon_v^e = d\varepsilon_{vp}^e + d\varepsilon_{vs}^e = \frac{\kappa}{v}\frac{dp}{p} + \frac{\kappa_s}{v}\frac{ds}{(s+p_{atm})}$$
Eq. 4.7

where p is the mean net stress (excess of mean total stress over pore air pressure), v is specific volume, κ and κ_s are two elastic soil constants and p_{atm} is atmospheric pressure included in the equation to avoid finite elastic volumetric strain as suction tends to zero. The first term represents the elastic volume changes caused by variation of mean stress and the second term represents the elastic volume changes caused by variation of suction. The elastic shear strain increments are also given by:

27

$$d\varepsilon_s^e = (\frac{1}{3G})dq \qquad\qquad \text{Eq. 4.8}$$

where G is the elastic shear modulus.

For an isotropic stress state, there are two yield curves; i.e. the Loading Collapse (LC) curve and the Suction-Increase (SI) yield curve. The LC yield curve predicts the onset of plastic volumetric strains during isotropic loading (increase of p) while SI yield curve predicts the plastic volumetric strains when the suction increases beyond the maximum past the suction ever experienced by the soil (s_0).

The volumetric plastic strain increments can be given by

$$d\varepsilon_v^p = d\varepsilon_{vp}^p + d\varepsilon_{vs}^p = \frac{\lambda(s)-\kappa}{v}\frac{dp_0}{p_0} + \frac{\lambda_s-\kappa_s}{v}\frac{ds_0}{s_0+p_{atm}} \qquad\qquad \text{Eq. 4.9}$$

where p_0 is the yield value of p at a suction s. Although some dependence of λ_s and κ_s on the net mean stress may be suspected but, for simplicity, they have been taken mostly as constants. In this study, the simulations did not include any stress paths in which the suction was changing. Thus, the SI yield curve did not play any role and Equation 4.9 could be shortened to the following form:

$$d\varepsilon_v^p = d\varepsilon_{vp}^p = \frac{\lambda(s)-\kappa}{v}\frac{dp_0}{p_0} \qquad\qquad \text{Eq. 4.10}$$

In a triaxial stress state, a third stress parameter, $q = (\sigma_1 - \sigma_3)$, has to be incorporated to include the effect of shear stresses. The LC yield curve forms a yield surface in q: p: s space converging to the modified cam-clay yield surface at zero suction (saturated soil). Accordingly, the yield curve at constant suction will be described by an ellipse that exhibits an isotropic pre-consolidation stress given by a previously defined p_0 value which lies on the LC yield curve; as in Equation 4.11.

$$q^2 = M^2(p + ks)(p_0 - p) \qquad\qquad \text{Eq. 4.11}$$

Where M and k are two soil constants.

A Cap-Plasticity (CP) model was developed and adapted for unsaturated soils based on BB model and implemented in Abaqus/Explicit. It was an elastoplastic model with the capability to define the yield surface as a function of volumetric strain similar to the one in BB model. A Cap hardening table was introduced using Equation 4.10. Having different initial void ratio and different confining pressures, different tables can be populated as an input to the CP model.

4.3 Calibration of Material Models

In this research, two different sands were used for modeling purposes. Sydney sand was used as the material in the calibration chamber models. Triaxial and CPT data from Pournaghiazar (2013) were used for calibration of the model. Fontainbleau sand was used for the preliminary free field model in which the CPT results in dry condition was used for calibration of the model based on the study by Kouretzis et al. (2014). In the following, properties of these two different sands and the calibration of material constitutive models are explained.

4.3.1 Sydney sand

The MC and DP model parameters were estimated first based on the properties of Sydney sand used during CPTs in the calibration chamber tests (Table 4.1) and then by matching the q-ε_q (deviator stress-deviator strain) and ε_p-ε_q (volumetric strain-deviator strain) curves of two triaxial compression tests with confining pressures of 50 kPa and 100 kPa reported by Pournaghiazar et al. (2013) which is shown in Figure 4.2. In addition, in order to develop the CP model, the cap hardening table was needed to be calibrated for both saturated and unsaturated conditions. Thus, triaxial test results of both saturated and unsaturated sand (at 200 kPa suction only) were used for

calibration of this model which is shown in Figures 4.2 and 4.3, respectively. The estimated MC

and DP model parameters and CP model parameters are shown in Tables 4.2 and 4.3 as well.

Table 4-1 Summary of geotechnical properties of Sydney sand (Pournaghiazar et al. 2013)

USCS classification	Particle density $Gs(gr/cm^3)$	Maximum void ratio e_{max}	Minimum void ratio e_{min}	Minimum dry density ρ_{min}	Maximum dry density ρ_{max}	critical state friction angle $\emptyset'_{cs}$	Poisson's ratio v
SP	2.65	0.92	0.6	1.38	1.66	36.3	0.3
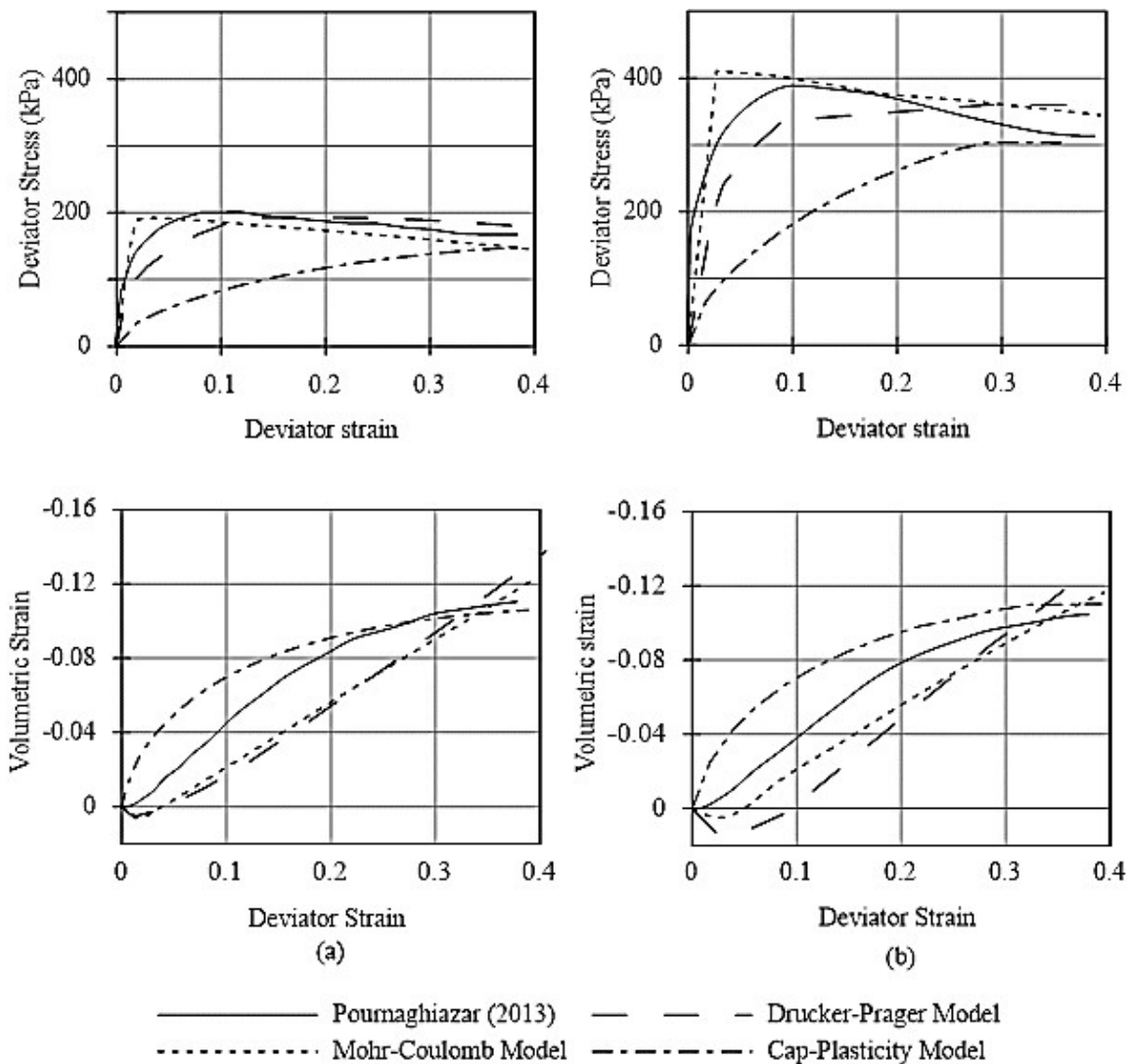
Figure 4-2 Results of triaxial test on saturated Sydney sand predicted using three material models, i.e. MC, DP, and CP model in comparison with experimental results, for (a) P=50 kPa, (b) P=100 kPa.

30
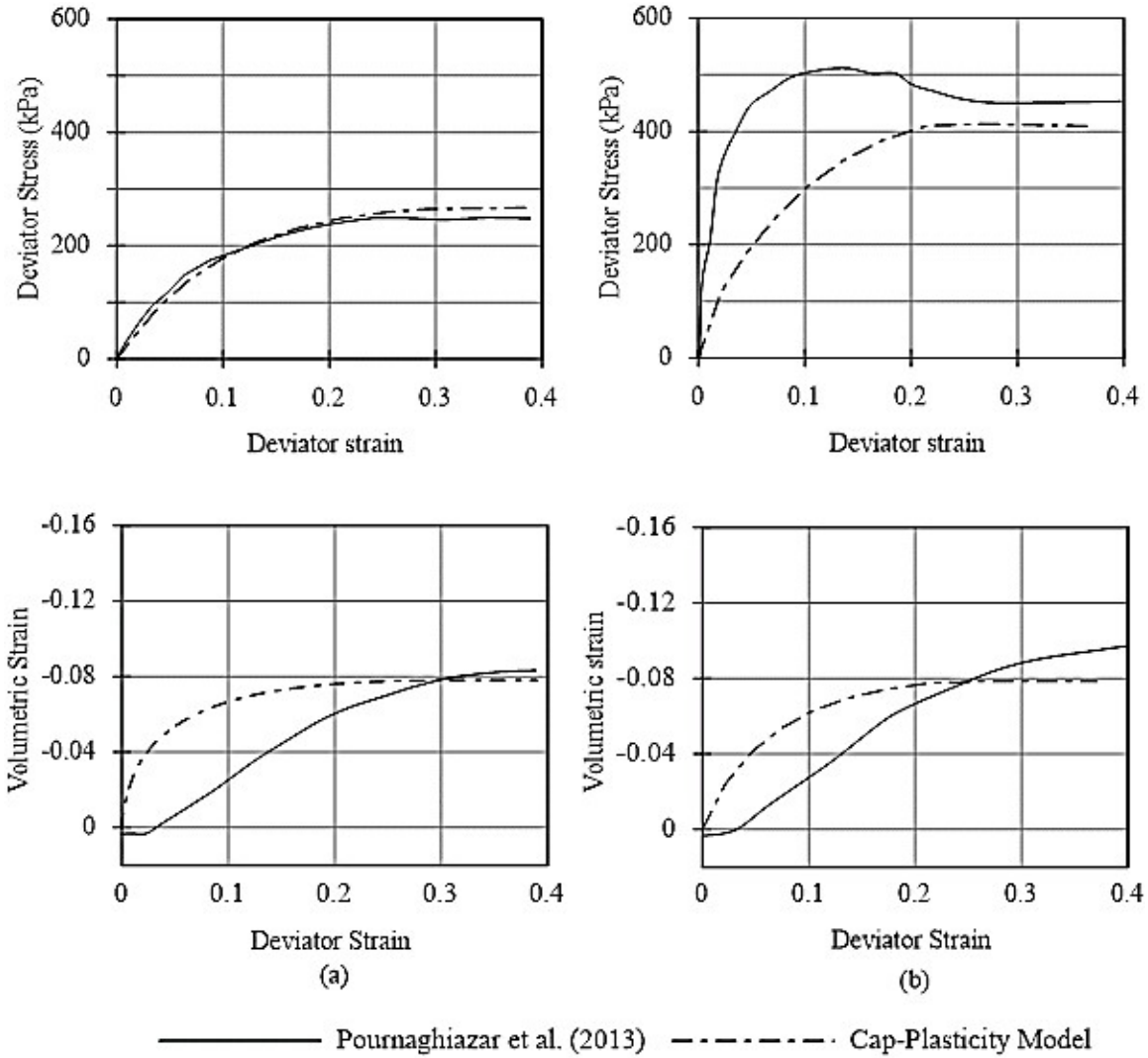
Figure 4-3 Results of triaxial test on unsaturated Sydney sand with s=200 kPa, predicted using CP model in comparison with experimental results, for (a) P=50 kPa, (b) P=100 kPa

Table 4-2 Mohr-Coulomb (MC) and Drucker-Prager (DP) models parameters of calibration chamber model

Parameter	Constitutive model	Value P=50kPa	Value P=100kPa
Density	MC, DP	1593 kg/m^3	1593 kg/m^3
Elastic modulus, E	MC, DP	10 MPa	20 Mpa
Poisson's ratio, ν	MC, DP	0.3	0.3
Dilation angle, ψ	MC, DP	5°	5°
Friction angle, φ	MC	41.6°	40.4°
Cohesion, C	MC	0.0000001 Pa	0.00000001 Pa
Angle of yield surface in p-t stress plane, β	DP	50	50
Flow stress ratio, K	DP	1	1

Table 4-3 Cap-Plasticity model parameters

Parameter	Value P=50kPa	Value P=100kPa
Density	1593 kg/m3	1593 kg/m3
Elastic modulus, E	10 MPa	20 Mpa
Poisson's ratio, ν	0.3	0.3
Dilation angle, ψ	5°	5°
Friction angle, β	60°	60°
Cohesion, d	0.0000001 Pa	0.00000001 Pa
Cap excentricity (R)	1	1
Initial yield surface position $\left(\varepsilon_{vol}^{pl}|0\right)$	0	0
Transition surface radius parameter (α)	0	0
Flow stress ratio, K	0.778	0.778

The very small value of cohesion for this sand was selected to avoid numerical instability in the system. In addition, equation 4.12 proposed by Bolton (1986) was used to update soil friction angle for different confining pressures.

$$\emptyset' - \emptyset'_{cs} = 3\left\{Dr\left[3.7 - ln\left(^{p'}/_{p_a}\right)\right] - 0.9\right\}$$ Eq. 4.12

where $\emptyset'_{cs}$ is critical state friction angle, Dr is the soil relative density, p' is the mean effective stress before shearing and p_a is the reference atmospheric pressure.

As it can be seen, the MC model has an elastic-perfectly plastic behavior while the CP model has an elasto-plastic behavior. The volumetric strain changes were better predicted by the CP model, which can be related to the cap hardening table definition in the CP model. However, all models can predict the ultimate strength of soil close to experimental results which showed the capability of models to represent the soil behavior in high deformations.

For unsaturated condition, Considering s_e equal to 7 kPa for Sydney sand, the effective stress parameter, χ, and the apparent cohesion c'', and friction angle values for each suction level under different confining pressures can be calculated, which are shown in Table 4.4.

The required parameters for populating the hardening tables of CP model can also be calculated using Equations 4.6 to 4.11 which are summarized in Table 4.5.

Table 4-4 Apparent cohesion and friction angle of MC and DP models for different confining pressures and suction values

Confining pressure (kPa)	Suction value (kPa)	Apparent cohesion (kPa)	Friction angle (degree)
50	25	11	41.6
	200	26.5	41.6
100	25	10.6	40.4
	200	25.4	40.4

Table 4-4 Cap hardening table parameters

Parameter	Value			
	P=50 kPa Saturated	P=100 kPa Saturated	P=50kPa Unsaturated (S=200 KPa)	P=100kPa Unsaturated (S=200 KPa)
$\lambda(0), \lambda(s)$	0.17	0.17	0.1	0.1
κ	0.06	0.06	0.06	0.06
e_0	0.677	0.685	0.78	0.697
p^c	90 kPa	90 kPa	90 kPa	90 kPa

4.3.2 Fontainebleau sand

The MC parameters for dry sand were estimated based on the properties of Fontainbleau sand which was used in Kouretzis et al. (2014) study, which is presented in Table 4.6.

Table 4-5 Fontainbleau sand properties

Parameter	Value
G_s	2.65
Dry density ρ (gr/cm^3)	1663
Void ration, e	0.59
Poisson's ratio, v	0.3
Critical state friction angle, $\emptyset'_{cs}$ (degree)	26.6
Cohesion, C (Pa)	0.0000001

In this case, the concept of applying the apparent cohesion was the same as CC model and the only difference was that the suction stress and as a result, the apparent cohesion was changing in depth. The apparent cohesion was calculated having the suction profile in depth and using the effective stress parameter from Equation 4.3. The air entry value, s_e, of Fontainbleau sand was

assumed 5 kPa using the suggested typical graphs by Lu and Likos (2004) based on the grain size distribution. Then, a user defined subroutine, VUMAT, was used to relate the vertical coordinate of the soil element to the corresponding apparent cohesion induced by suction based on the distribution of the suction in depth with regards to the water table level, shown in Figure 4.4.

Water table at 2 m below the ground		
$d_1 = 0.5$ m	$\chi_1(u_a - u_w) = 4.9$ KPa	$c_2' = 3.9$ KPa
$d_2 = 1.5$ m	$\chi_1(u_a - u_w) = 9.35$ KPa	$c_2' = 7.3$ KPa

Water table at 3m below the ground		
$d_1 = 0.5$ m	$\chi_1(u_a - u_w) = 4.9$ KPa	$c_2' = 3.9$ KPa
$d_2 = 2.5$ m	$\chi_1(u_a - u_w) = 11.2$ KPa	$c_2' = 8.4$ KPa
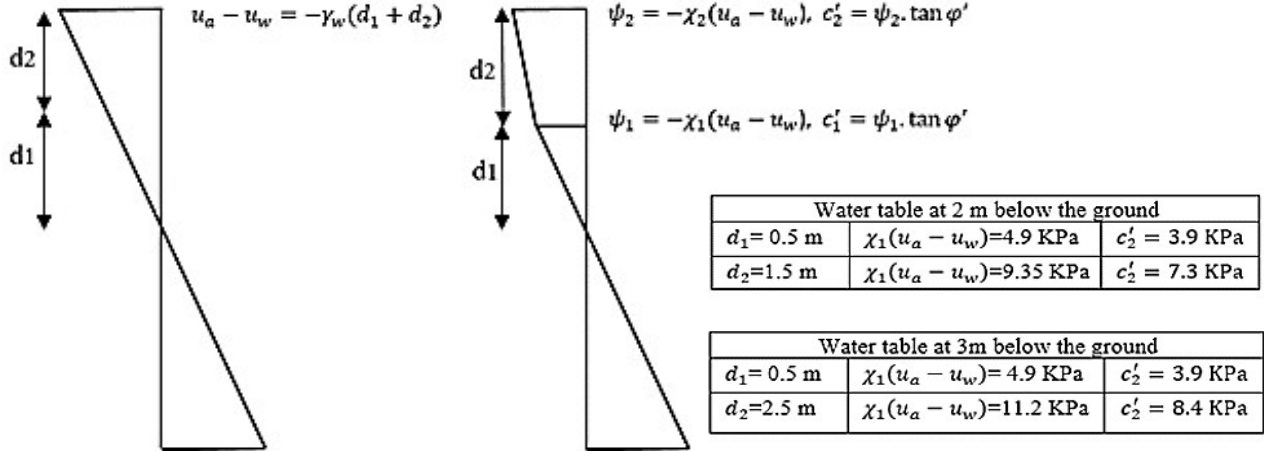
Figure 4-4 Suction, suction stress, and apparent cohesion profiles in the sand layer with different water table levels

4.4   Mesh Properties

4-node bilinear, axisymmetric quadrilateral reduced integration elements (CAX4R) were used for both soil domain and cone and they were both considered as deformable bodies. To prevent mesh distortion problem in soil elements, the remeshing method, ALE, was used which keeps the mesh size fine enough during penetration and allows independent movement of mesh from material while maintaining the topology (the element and connectivity) of the mesh.

4.5   Interaction Model

When surfaces are in contact, they usually transmit shear as well as normal forces across their interfaces. The relation between these two force components is known as friction and can be

considered using a contact model. Different interaction models are available in Abaqus such as general contact model and surface to surface model. In this analysis, a pure master-slave relation was used to model the cone-soil interaction in which a surface-to-surface contact was defined. In this contact model, the master surface can penetrate the slave but not the reverse, and the slave object can be a surface or a node region. The cone was chosen as the master surface, and the soil domain was considered to be the slave node region. With this model, the soil nodes cannot penetrate the cone, whereas the nodes on the cone's surface can penetrate the soil region. The mesh configuration can affect the performance of the contact model. As an example, the mesh should be fine enough so that during the penetration, several elements of cone and soil would be in contact. Otherwise, the simulation will be terminated due to mesh overlap.

The contact model was defined in tangential direction using the penalty method with no limit for the magnitude of the transmitted shear stress. The friction coefficient at the cone-soil interface was assumed to be constant, and was determined from the back-analysis of CPT test results equal to $\mu=0.43$ for MC and DP models and $\mu=0.45$ for CP model. Assuming this value for friction coefficient resulted in an interface friction angle of $\delta=\tan^{-1}\mu=25^{\circ}$, which was consistent with the suggested value of soil-pile friction angle for medium sand (API 1993). For tracking contact nodes, "finite sliding algorithm" was used, in which the nodes and elements paired between master and slave surfaces are tracked and kept linked until the calculation stops. This approach gives more accurate results compared to "small sliding algorithm".

4.6   Remeshing Method

One of the challenging tasks in modeling the penetration process is mesh distortion due to the large deformation of elements around the cone. To avoid this problem, very fine mesh was implemented in the soil zone near the cone, complemented by an adaptive remeshing technique.

ALE remeshing approach has shown satisfactory results in addressing the mesh distortion and large deformation problems. ALE is an efficient method to maintain a high quality mesh when large none-recoverable deformation occurs. It combines the features of pure Lagrangian analysis and pure Eulerian analysis. In pure Lagrangian analysis, mesh follows the material, but in Eulerian method, the material flows through the mesh while the mesh is fixed. This adaptive remeshing technique allows the mesh to move independent of material while it doesn't alter the topology (element and connectivity) of the mesh. In the present study, ALE was used for soil elements and the 'improve aspect ratio' was considered as remeshing algorithm. To maintain the quality of mesh, the regeneration of mesh was set to be at every time step, although it involves a high computational cost. It should be mentioned that the final actual cone resistance profiles included some oscillation due to frequent remeshing. Thus, in order to remove the noise from the data, these curves were filtered and smoothed.

4.7 Cone Penetration Model Verification

4.7.1 Calibration chamber model

Penetration of a 500 mm long cone with a 16 mm diameter into a sandy soil inside a calibration chamber was modelled. Model geometry, boundary conditions, and mesh configuration are shown in Figure 4.5. Soil domain is 160 mm-wide and 800 mm-high. The side boundary was located at radial distance of 20 times the cone radius to reduce the boundary effects (Bolton et al. 1999). The bottom boundary was completely fixed while a constant normal stress boundary, equal to the confining pressure in a calibration chamber, was considered for the top and sides of the model. Two confining pressures of 50 and 100 kPa were considered in this study to be consistent with Pournaghiazar (2013) study. In order to model the penetration process, a downward vertical

velocity of 250 mm/s was imposed to the cone's top nodes, which were all coupled together. Penetration was considered to begin from the soil surface.
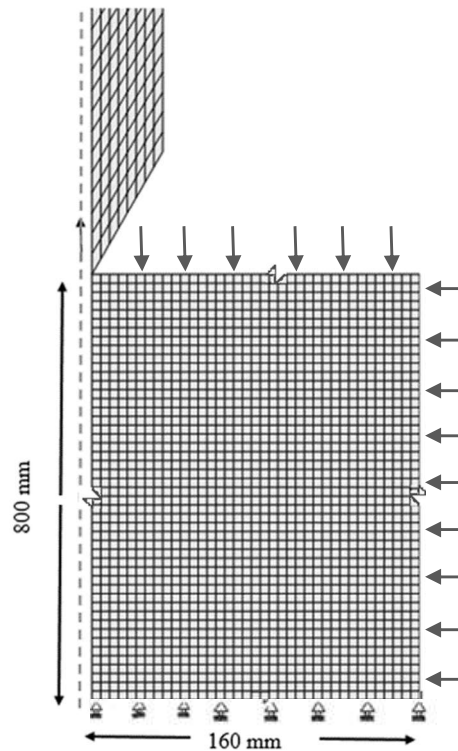
Figure 4-5 Geometrical schematic of Abaqus models

The performance of the constructed numerical model was verified based on experimental calibration chamber test results for saturated Sydney sand with a relative density of 61% and confining pressures of 50 kPa and 100 kPa (Pournaghiazar et al. 2013); according to the modeling details discussed in previous sections. Results of these two models are plotted in Figure 4.6 compared with the experimental results from Pournaghiazar et al. (2013) calibration chamber tests. Further, q_c profiles were also compared with two cone resistance empirical equations. Jamiolkowski (1985) proposed an empirical equation based on cone resistance (q_c), vertical effective stress (σ'_v), and relative density (D_r), obtained from CPT tests on five predominantly silica sands with different compressibility; e.g. Equation 4.13 for a sand with moderate compressibility.

38

$$\left(\frac{q_c}{\sigma_v'^{0.5}}\right) = 10^{\left(\frac{Dr+98}{66}\right)} \qquad\qquad Eq.\,4.13$$

Similarly, Baldi et al. (1986) proposed Equation 3.14 to predict q_c value of soils with different relative densities and vertical stresses.

$$q_{c=C_0}(\sigma_v')^{C_1}.\ e^{C_2.Dr} \qquad\qquad Eq.\,4.14$$

where C_0, C_1, and C_2 are constant parameters equal to 157, 0.55 and 2.41 for normally consolidated sand, respectively.

Figure 4-6 Comparison of Cone penetration profiles obtained experimentally and numerically using MC, DP, and CP material models for saturated sand inside a calibration chamber with Dr=61%); (a) P=50 kPa, (b) P=100 kPa

The ultimate q_c value of numerical results associated with CPTs under both confining pressures were consistent with the reference calibration chamber results and close to the empirical equations values. This confirms that all three models with evaluated parameters were able to effectively capture the soil's behavior. As seen in Figure 4.7, the experimental calibration chamber data reported by Pournaghiazar et al. (2013) shows an increase in q_c before reaching a peak and then dropping to a relatively constant value. The peak is considered to be mostly due to the interaction of the chamber rigid top platen with the cone-induced zone of plasticity (Pournaghiazar et al 2013). Thus, the relevant q_c value for comparison is the lower steady portion of the profile. Despite the boundary condition in the chamber, the soil top boundary is free in numerical model which prevented this peak in the numerically predicted q_c profile. The q_c in numerical model gradually increased until it reaches a constant value in depth. After reaching the uniform resistance profile the numerical penetration model was stopped to save computational effort and the final steady value was chosen as the cone resistance.

4.7.2   Free field model

An axisymmetric Finite Element (FE) model was developed in Abaqus/Explicit to simulate the cone penetration. It replicated the penetration of a 10 mm diameter cone into a sandy soil inside a geotechnical centrifuge spun at 70g. The base model included a soil layer in dry condition while models with saturated and unsaturated soil layers with water table level at depth of 2 m and 3 m were considered consecutively. The model properties were chosen based on a study by Kouretzis et al. (2014) that replicated the centrifuge tests carried out by Bolton and Gui (1993) at the Cambridge Geotechnical Centrifuge Center. The results of this study was used to validate the efficiency of the penetration model in dry condition.

Soil domain was modeled as a 100 mm-wide and 250 mm-high domain. The bottom boundary was completely fixed while the side boundary was fixed in radial direction. A body force with magnitude of $B = \rho.g.N$, where ρ is the soil density and N is the centrifuge acceleration level in g's (here N=70), was applied on the soil elements. Thus, the same geostatic effective stresses as in a free field soil model was achieved. The soil lateral stresses were also calculated by considering the earth pressure coefficient at rest equals to $k_0 = 1 - \sin\varphi$.

After model validation with dry test results, water table was raised to the soil surface simulating a fully saturated soil. Then, water table location was lowered in the following simulations where the water table level varied from zero in saturated soil to 1 and 2 m from the ground surface in unsaturated soil models. The soil below the water table was considered fully saturated while the soil above the water table was considered unsaturated with a variable hydrostatic suction profile in depth. The penetration process was modeled by imposing a downward vertical velocity of 25 mm/s to the cone's top nodes, which were all coupled together.

The mesh properties, contact model and the remeshing method were similar to the calibration chamber model which was discussed earlier.

In addition, A VUMAT subroutine was used in Abaqus/Explicit to update soil friction angle with the stress state using Equation 4.12 proposed by Bolton (1986). In the model, the stress state at element level was automatically saved in each time step and then the friction angle was updated accordingly.

The constitutive model parameters will be either directly adapted from Table 4.6 or calibrated using the centrifuge test results carried out by Bolton and Gui (1993) at the Cambridge Geotechnical Centrifuge Center on dry Fontainbleau sand with relative density of 89%.

The cone penetration result in the centrifuge is presented in Figure 4.7 shows the cone resistance, q$_c$, versus the corrected prototype depth, Z_{pc}, which was calculated based on the following equation:

$$Z_{pc} = Z_p \left[1 + \left(\frac{Z_m}{2R}\right)\right] \qquad\qquad Eq.\,4.15$$

where Z_p is the prototype penetration depth ($Z_p = N.Z_m$), Z_m is the model penetration depth, and R=0.3755 m is the average radius to the surface of the sand specimen.

Due to the frequent remeshing, the numerical results contained numerical noise, which were smoothed using a moving average function. It can be observed that the numerical model results are close to measured cone resistance profile of centrifuge testing which indicates the success of the numerical CPT model in implementing the abovementioned constitutive model, penetration simulation techniques, and stress-dependent friction angle.
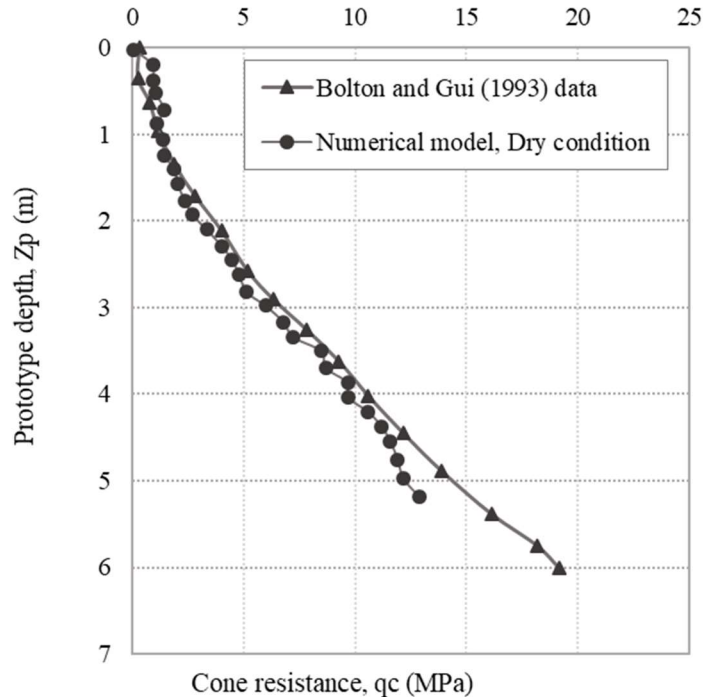
Figure 4-7 Comparison of the results from the numerical model and reported experimental centrifuge cone penetration by Bolton and Guie (1993)

4.8 Results in Unsaturated Condition

Results of numerical model in unsaturated condition are presented in the following. It includes results of calibration chamber model and results of free field model.

4.8.1 Calibration chamber results

4.8.1.1 Cone resistance

Cone resistance, q_c, profiles for CPT in unsaturated sand were numerically estimated using MC, DP and CP material models and compared with the reported profile by Pournaghiazar (2013). Figure 4.8 shows the results of MC and DP models for degree of saturation corresponding to a suction value of 25 kPa while Figure 4.9 shows the result of all three models for degree of saturation corresponding to a suction value of 200 kPa. The CP model was not considered for the suction value of 25 kPa due to the lack of triaxial test data to produce the cap hardening table at this suction value. All models had initial relative density of 61% and confining pressures of either 50 kPa or 100 kPa. The results show that suction influenced q_c considerably and caused an increase in cone resistance from saturated to unsaturated conditions. The effect of suction was more significant in low confining pressures, which is evident, where suction has more influence on the effective stress and consequently on the overall resistance. This is expected in shallow depth where the soils are mostly unsaturated and suction-induced gain of strength is more pronounced. For example, for the confining pressure of 50 kPa, the q_c was increased by 20 % and 30 % for suction values of 25 kPa and 200 kPa, respectively, while for confining pressure of 100 kPa, q_c was only increased by 9% and 26%, respectively.
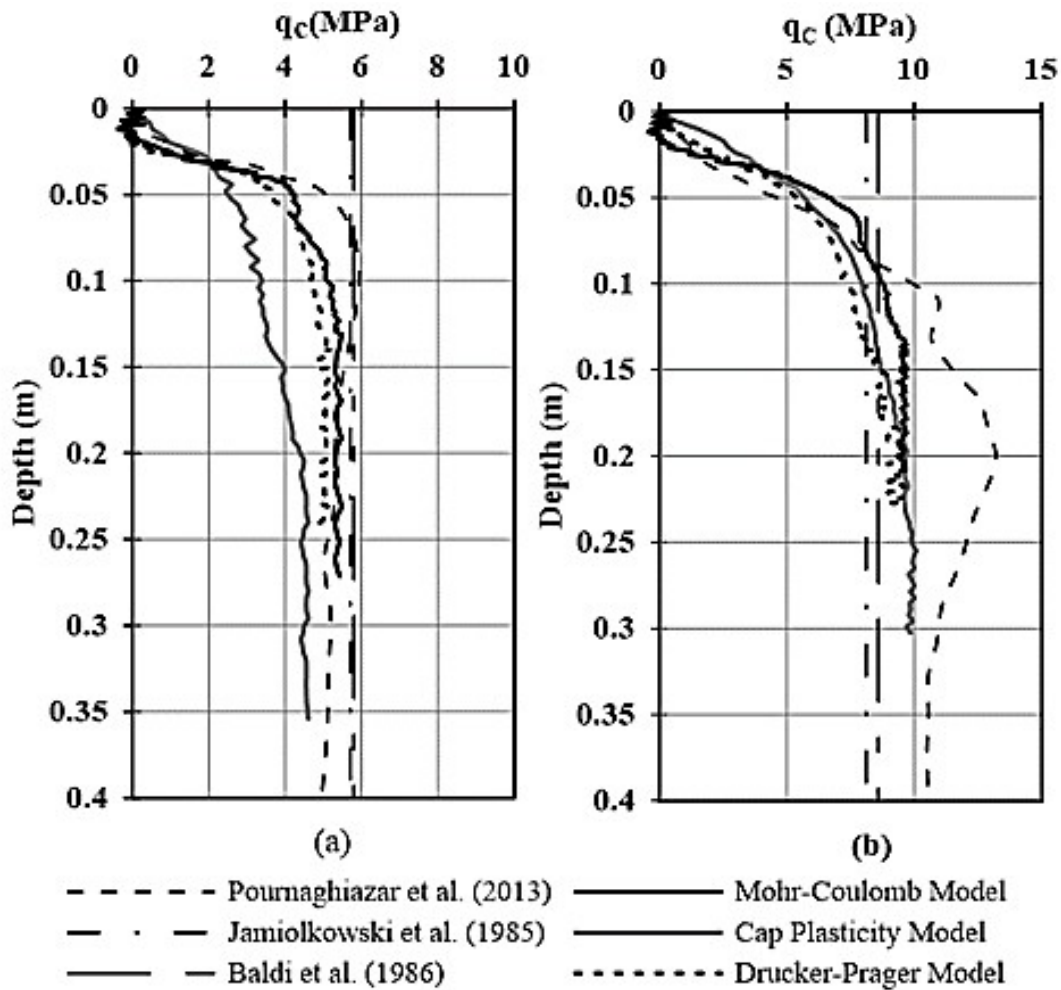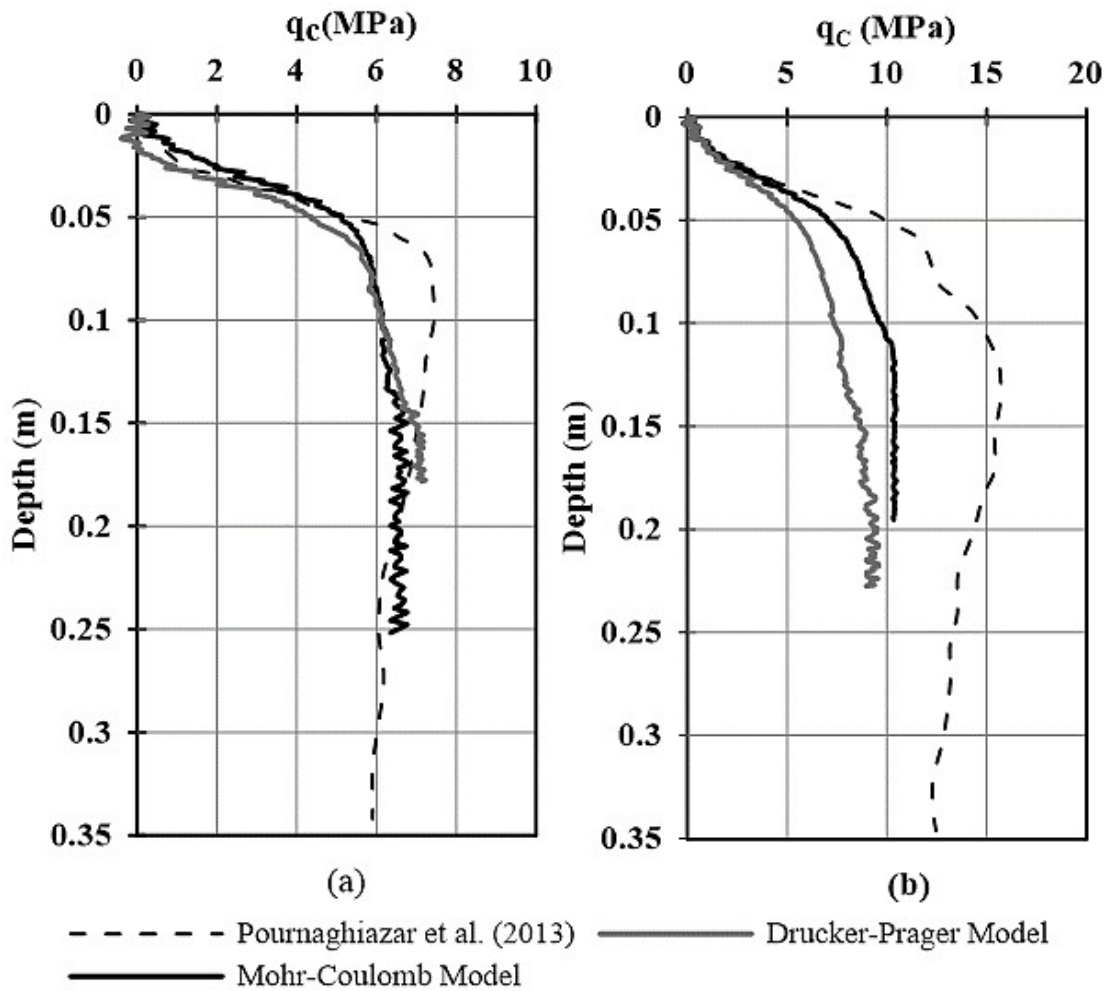
Figure 4-8 Comparison of cone penetration profiles obtained experimentally and numerically

using MC and DP material models for unsaturated sand with s=25 kPa inside a calibration

chamber with Dr=61%; (a) P=50 kPa, (b) P=100 kPa
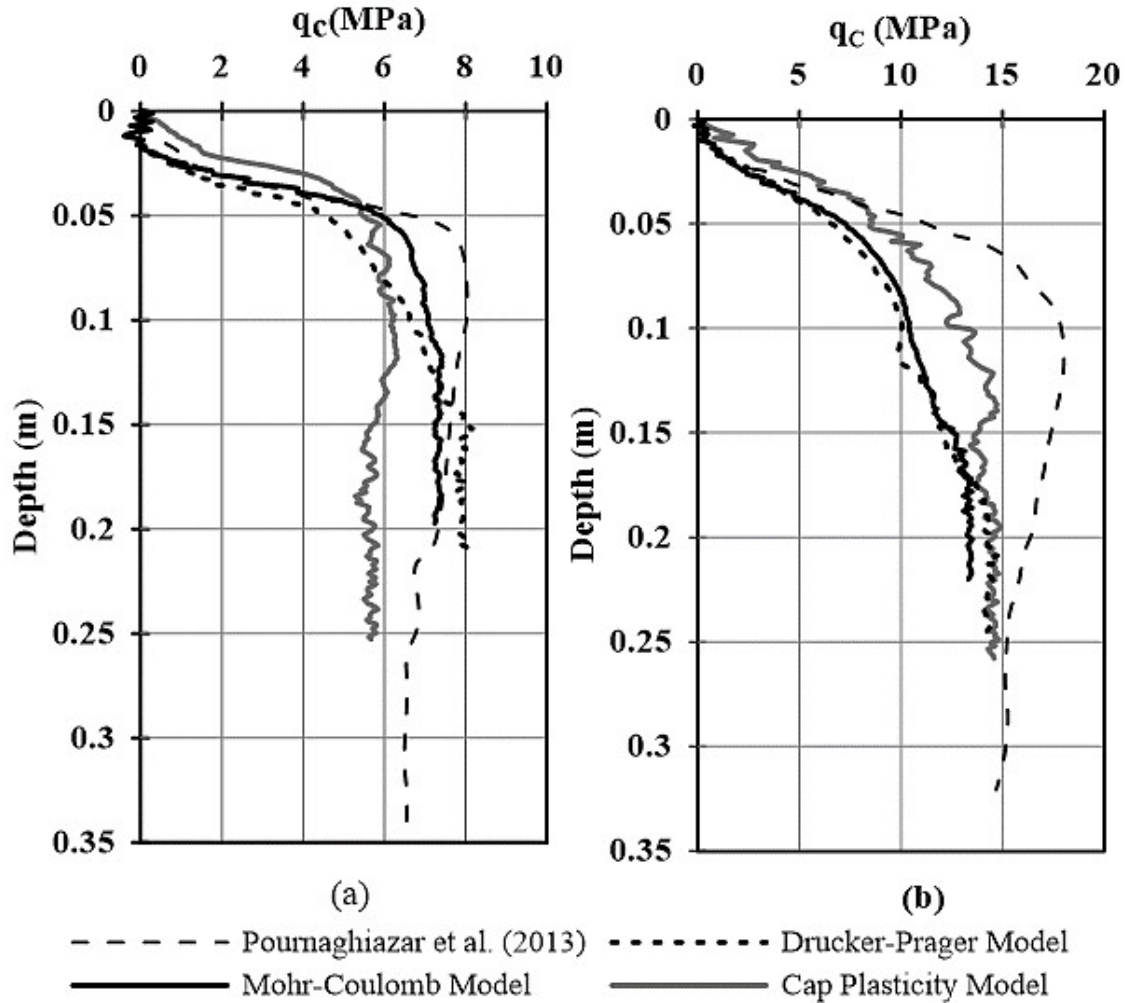
Figure 4-9 Comparison of cone penetration profiles obtained experimentally and numerically using MC, DP, and CP material models for unsaturated sand with s=200 kPa inside a calibration chamber with Dr=61%; (a) P=50 kPa, (b) P=100 kPa

Comparing the numerical estimates and calibration chamber data (Pournaghiazar et al 2013), the MC and DP models slightly overestimated the ultimate value of q_c in 50 kPa confining pressure while they underestimated the q_c in 100 kPa confining pressure. The CP model also underestimated q_c in confining pressure of 50 kPa, which was the case even in saturated condition. However, all three models could predict close q_c values to experimental ones. This confirms the efficiency of indirect application of suction and degree of saturation in the material models in the

MC and DP model as oppose to a more detailed CP model. For example, simple MC model relatively better predicted the experimental results. This might be attributed to the type of the problem in which the ultimate condition and not the deformation path is critical. Also, the q_c profile in the CP model was more similar to the experimental results. It showed an initial increase and then decrease of q_c value before it became constant while in the MC and DP models, the q_c profile had a graduate increase until it reached the constant value. This can be related to the definition of this model in which the yield surface is related to the plastic volumetric strain by defining a hardening table in the model which allows the yield surface to expand and contract. In contrast, the yield surface in the MC and DP models only depends on the stress state.

4.8.1.2 Stress distribution

The contours of stress distribution after 50 mm of cone penetration in unsaturated sand with confining pressure of 100 kPa and suction value of 200 kPa from MC model (as an example) are shown in Figure 4.10. The stress distribution indicated that the vertical and horizontal stresses surrounding the cone tip increased greatly due to the penetration and were higher near the upper end of the cone in comparison with the ones near the tip. This shift of stress to the upper end of the tip was likely because of the frictional interface between the cone and the sand and the geometry of the cone, which resulted in a stress built-up; similarly reported by Susila and Hryciw 2003.
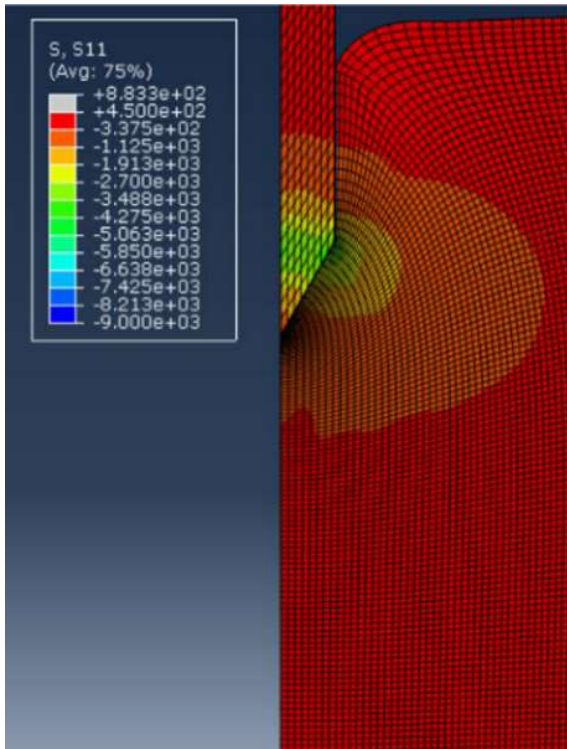
(a)
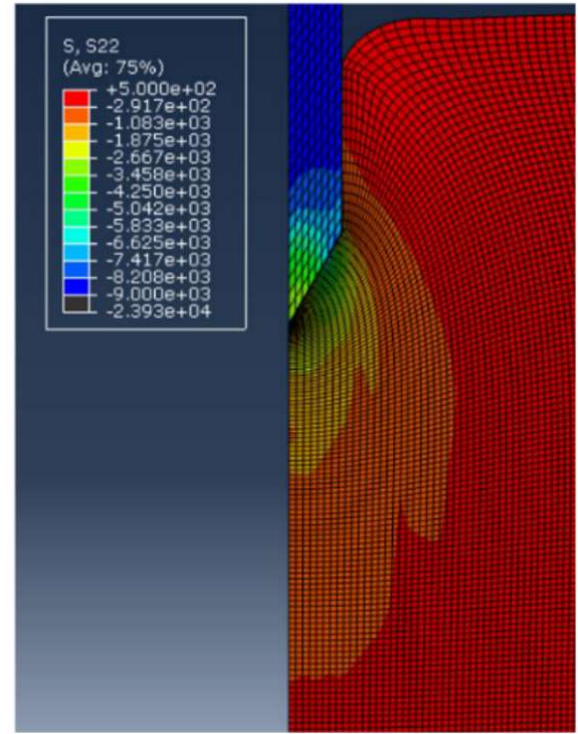
(b)
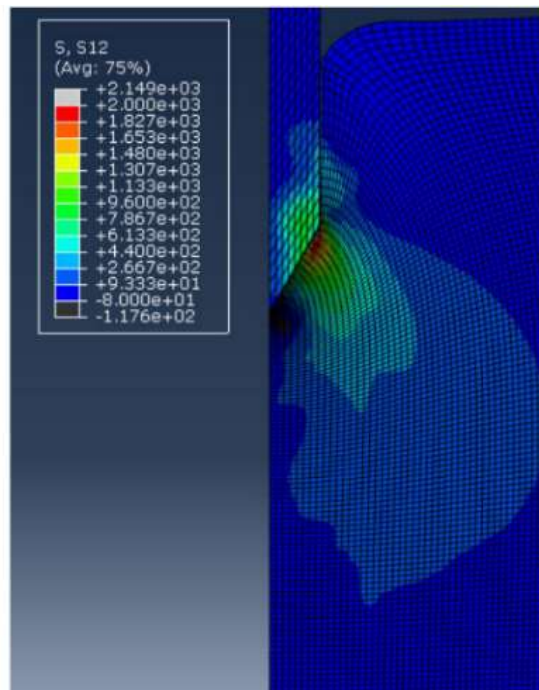
(c)

Figure 4-10 Stress distribution contours after 50 mm of cone penetration obtained from MC model with P=100 kPa and s=200 kPa; (a) horizontal stress, (b) vertical stress, (c) shear stress (the legend values are expressed in kPa)

To evaluate the stress distribution in sands with different degrees of saturation, the generated horizontal stresses were examined away from the cone tip. Horizontal stress-distance curves for 150 mm deep cone penetration under different confining pressures and saturation conditions from the MC model are presented in Figure 4.11. Presence of suction in unsaturated sand increased the induced horizontal stress inside the zone of influence while the stress values converged outside this zone. For all confining pressures and degrees of saturation, the induced horizontal stress stayed constant at and beyond a distance approximately 6 times the cone radius.
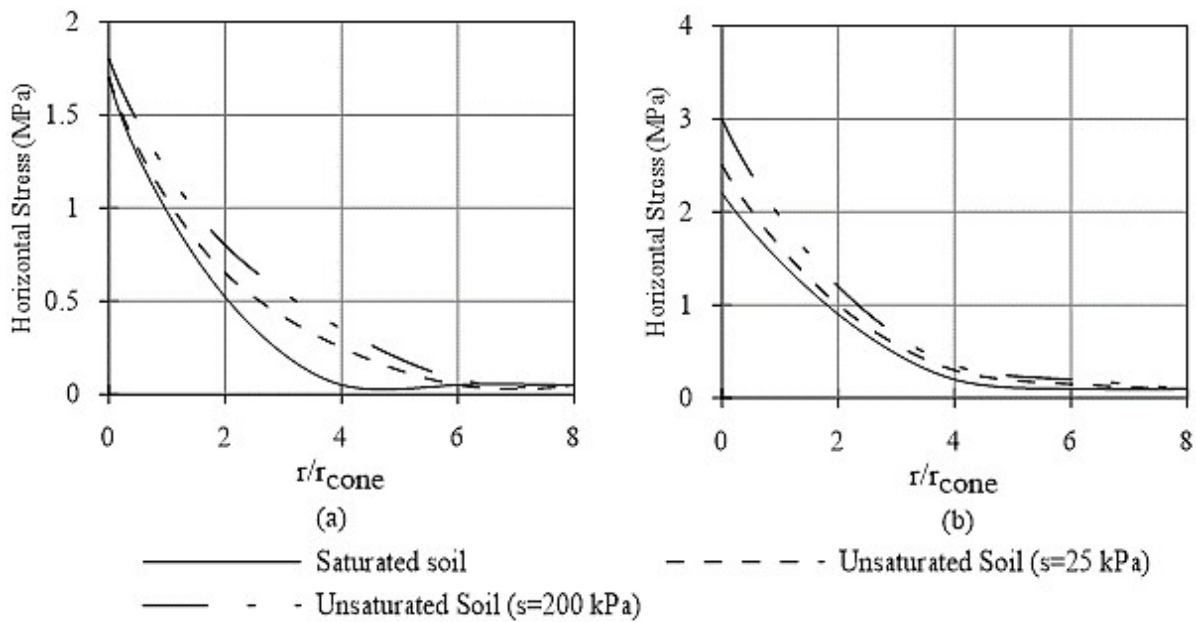
Figure 44-11 Comparison of horizontal stress gradient for penetration in saturated and unsaturated soils using MC models with (a) P=50 kPa, (b) P=100 kPa shown versus normalized distance (ratio of the distance from the cone tip to the cone radius)

4.8.1.3 Soil strength parameters

Many soil properties have been commonly estimated using CPT data through empirical correlations. However, neglecting the effects of degree of saturation and suction may result in misinterpretation of these properties. To better demonstrate this possible inaccuracy, four

48

parameters including relative density (Dr), friction angle (φ'), lateral earth coefficient at rest (k_0), and elastic modulus (E) were examined using the available relations with and without considering the degree of saturation. A summary of these values are presented in Table 4.7.

Table 44-6 Soil strength parameters estimation based on empirical equations

Soil condition	p=50kPa				p=100kPa			
	Dr (%)	Φ (degree)	k₀	E (MPa)	D_r (%)	Φ (degree)	k₀	E (MPa)
Saturated (S=0)	61	40.7	0.65	15	61	40.1	0.61	27
Unsaturated (S=25kPa) Neglecting suction stress	69	42.2	0.71	16.5	65.4	41	0.63	28.9
Unsaturated (S=25kPa) considering suction stress*	66	41	0.66	19.8	63.7	40.3	0.61	29.4
Unsaturated (S=200kPa) Neglecting suction stress	71	42.5	0.72	19.25	72.6	42.3	0.63	33.75
Unsaturated (S=200kPa) Considering suction stress*	64	40	0.61	21	69	40.9	0.6	37.1

$^*\sigma'_{v0} = (\sigma - u_a) + \chi(u_a - u_w)$

The relative density (Dr) was estimated using a well-established formula resulted from interpretation of a large number of calibration chamber test results for different sands (after Jamiolkowski et al. 1985), as in Equation 4.16, in which C can vary between -78 and -128 depending on the soil compressibility. Having the relative density of 61% in all simulated tests, C is assumed -94 and -101 for P=50 kPa and P=100 kPa, respectively, consistent with that of saturated condition.

$$D_r = C + 66 \, log_{10} \frac{q_c}{[\sigma'_{v0}]^{0.5}} \qquad\qquad Eq.\,4.16$$

The friction angle was predicted using the following expression developed by Kulhawy and Mayne (1990).

$$\emptyset' = tan^{-1}\left[0.1 + 0.38 \log\left(\frac{q_c}{\sigma_v'}\right)\right] \qquad Eq.\,4.17$$

Lateral earth coefficient at rest (k_0) was also estimated based on the recommendation by Mayne (1991) as follows:

$$k_0 = \frac{\left(p_a/\sigma_{v0}'\right) \cdot \left(q_c/p_a\right)^{1.6}}{145 exp\left[\left(\frac{q_c/p_a/\left(\sigma_{v0}'/p_a\right)^{0.5}}{12.2\,(OCR)^{0.18}}\right)^{0.5}\right]} \qquad Eq.\,4.18$$

Finally, Secant Young's modulus (E_s') was determined using charts, developed based on calibration chamber data, that relate modulus to relative density, over consolidation ratio, and current mean stress level (Baldi et al 1989) as shown in figure 4.12.
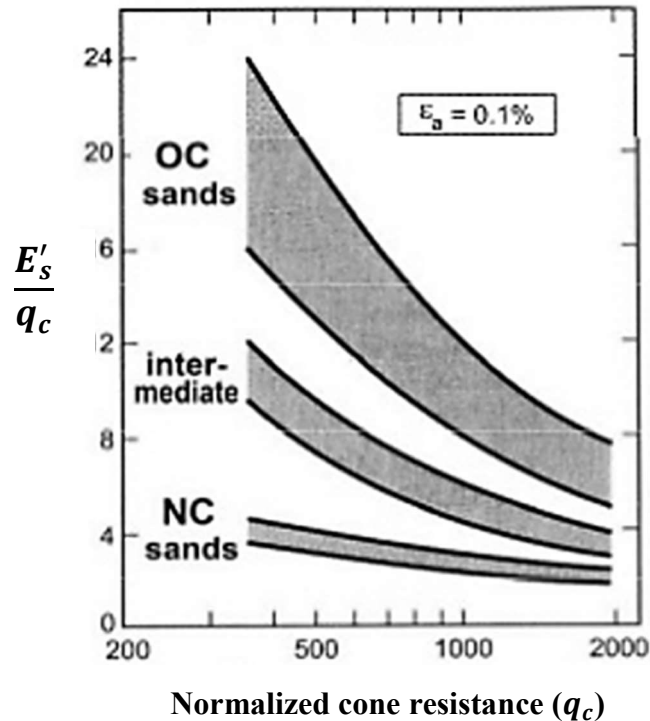
Figure 4-12 Evaluation of drained Young's modulus from CPT for silica sands (from Baldi et al., 1989)

50

The data listed in Table 4.7 illustrate that using empirical equations relating the q_c value and soil properties without considering the degree of saturation underestimated the soil strength parameters in most cases. This effect was more pronounced for D_r , k_0 and E, which were underestimated as low as 10 degrees, 10 %, and 30%, respectively. The friction angle, however, was less sensitive to unsaturated soil condition. In addition, the saturation effect was not the same for different confining pressures and suction values. For example, D_r was more affected in high suction values while k_0 was more influenced in low confining pressures. However, applying suction stress in the calculation of the effective stress for unsaturated soils used in these empirical relations can decrease the offset in these parameters except in the modulus where it was further increased as a result of suction stress contribution. Overall, it can be concluded that adapting these empirical relations that have been mostly developed based on test results from saturated or dry soils and using them in unsaturated soil condition may cause misestimating the soil parameters. Modified effective stress values using suction stress may help to some extent. However, new empirical equations, developed and verified for unsaturated soil conditions, or numerical simulations as shown in this paper will provide more accurate predictions.

4.8.2   Free-field model results

Cone resistance (q_c) profiles associated with fully dry and fully saturated soil layers are shown in Figure 4.13. Comparing these profiles, one can see that the cone resistance values in saturated soil zones were less than the ones in dry soil layer. For instance, the cone resistance value in the saturated soil at 4 m depth was about 6 MPa while it was about 10 MPa for the same depth in the dry soil layer. This was expected as the effective stresses in dry soil were higher than in saturated soil condition for a given depth resulting in a stiffer soil due to the effective-stress dependency of the shear strength.
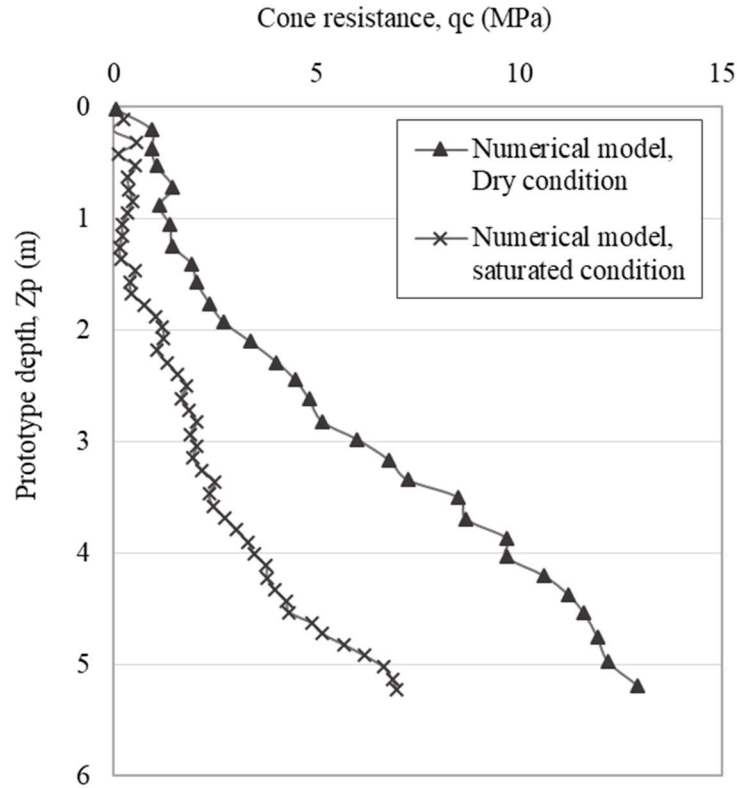
Figure 4-13 Cone resistance profiles of fully dry and fully saturated sand layers

Figure 4.14 shows the cone resistance profiles in fully saturated and two partially saturated soil layers (water table at 2 and 3 m depth). Comparing the q_c profiles of soil layers with different levels of water table (i.e. unsaturated and saturated soils) one can see that the cone resistance values in unsaturated soils are higher than the ones in saturated condition up to a certain depth. For instance, at the depth of 3 m, the cone resistance for saturated soil layer (where the water table was at the ground surface), unsaturated soil layer with water table level at 2 m depth, and unsaturated soil layer with water table level at 3-m depth, are 3.7 MPa, 4.5 MPa and 5.5 MPa respectively. This clearly signifies the increase in cone resistance due to the presence of suction in unsaturated soils. However, in depths more than 5 m, the cone resistance in soil layers with lower water table levels became closer to the one in fully saturated soil layer. This can be attributed to a change in the governing parameter in the cone resistance as the cone passes the water table. For instance,

52

above the water table level, the response was controlled mainly by the suction stress as it increased the effective stress and consequently the strength in the soil. However, the soil body force would be less in saturated soil that resulted in lower confining stresses in deeper depths, which in turn, resulted in changes of the slopes in the cone resistance profiles. Thus, numerically, changes of density and presence of suction acts simultaneously, which can contribute to different overall resistance at different depths.
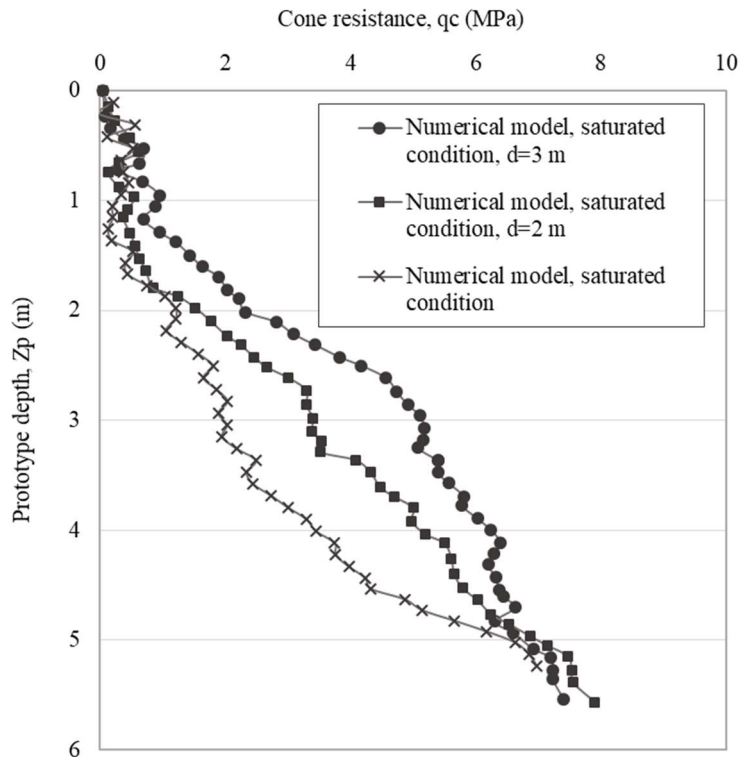
Figure 4-14 Cone resistance profiles of fully saturated and partly saturated sand layers with water table at 2 and 3 m depth

Chapter V

Development of a Miniature Piezocone Setup

5.1 Introduction

This chapter presents details of development of a new miniature piezocone set up for conducting cone penetration tests inside the UNH geotechnical centrifuge. The equipment was designed and manufactured in collaboration with Geokon Inc. Details of miniature piezocone design are explained in section 5.2. It is followed by explaining the driving apparatus in section 5.3. The load cells calibration procedure is discussed in section 5.4 and the saturation and calibration procedure of the pore pressure transducer is discussed in section 5.5.

5.2 Miniature Piezocone Design

A miniature piezocone was designed and constructed adaptable for testing in unsaturated soils to meet the size and capacity requirements of the geotechnical centrifuge at UNH (Ghayoomi and Wadsorth 2014). The developed piezocone is 95 mm in length and 12.7 mm in diameter (projected area of 126.6 mm^2) with an apex angle of 60º. Figure 5.1 shows the piezocone components. It includes cone tip, filter, friction sleeve, upper rod, load cells, pore pressure transducer and connecting tube. The cone tip is removable and makes it possible to use different

porous stones with different air entry values based on the need. The available ones in the laboratory are sintered stainless steel one with 60 micron pore sizes and ceramic ones with 6 micron pore size (air entry values of 50) and 2.5 micron pore size (air entry value of 100 kPa). For this study, the ceramic porous stone with 6 micron pore size (air entry values of 50) was used. The cone body consists of two parts, friction sleeve and upper rod. The friction sleeve is 40 mm long and the upper rod provides the required space for the load cells.
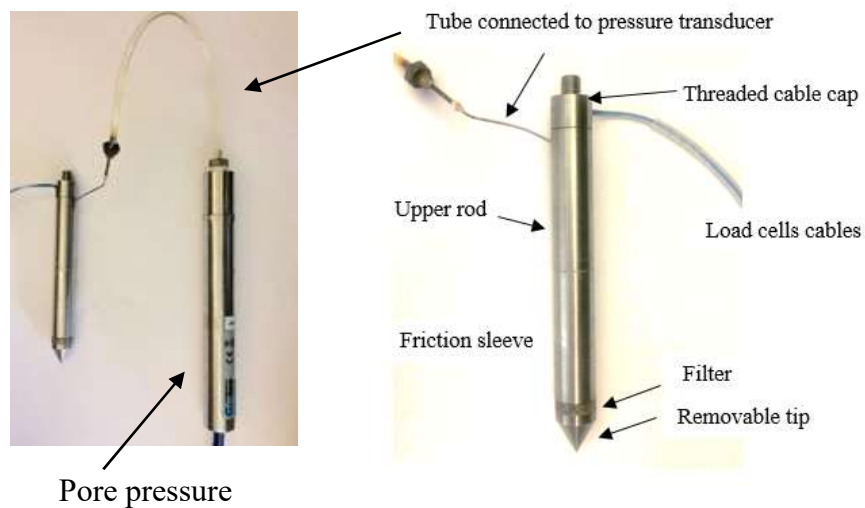
Figure 5-1 Miniature piezocone components

Two vibrating wire force gages, designed by Geokon Inc., measure the tip resistance and total resistance. The front force gage, located inside the shaft, measures the tip resistance while the rear force gage, located at the base of the shaft, measures the total load which makes it possible to evaluate the skin friction (f_s) along the piezocone shaft by subtracting the two. A commercial vibrating wire pore pressure transducer (model 4500S-1MPa) developed by Geokon Inc. was used for measuring the pore water pressure during the penetration (Figure 5.2). The transducer is placed outside the cone and connected to the water chamber behind the cone porous stone with a narrow tube (Figure 5.1).
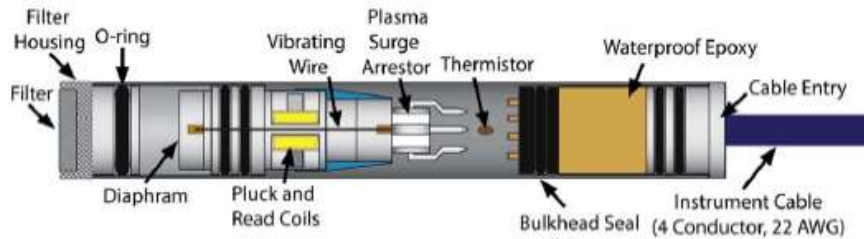
Figure 5-2 Pore Pressure transducer 4500S-1Mpa (Geokon Instruction Manual)

Considering the maximum expected penetration depth of 7.5 cm due to the space limitation in the centrifuge overhead, the potential spin acceleration of 40g (which provides an equivalent prototype penetration depth of 3 m) and having the effective stress of the soil in this depth, the expected cone tip resistance was predicted to be about 2-10 MPa. This stress produces about 0.25-1.25 kN (60- 300 lbf) force on the cone tip which is below the capacity of the load cells.

A container with an inside length of 360 mm, width of 180 mm, and depth of 270 mm was used for the penetration tests. The container dimension to the cone diameter ratio (B/d) is 14 and 28 for each side. According to recommendation by Bolton *et al*. (1993), the penetration of a probe with diameter of d would not affect the properties of soil outside a 20d diameter cylinder. However, in the case of having a larger ratio in one side, this ratio can decrease into 10 (Phillips and Valsangkar 1987). Thus, there is no side boundary effect in penetration tests. In addition, the maximum penetration depth of 75 mm provides 190 mm distance between the cone tip and the bottom of the container at maximum penetration. Lee (1989) showed for a 12 mm diameter probe, 10 cm distance is enough to prevent any bottom boundary effect. Thus, there is no base boundary effect in penetration tests as well.

Ottawa sand used in this investigation has a mean grain size (d_{50}) of 2 mm that results in the cone diameter to the mean soil particle ratio (d/d_{50}) of 63 which is greater than the critical ratio of 30 that avoids particle size effect (Bolton 1990).

56

5.3 Driving Apparatus and Data Acquisitions System

A custom-made version of "L16 series mini linear actuator" by Graig Kackert Design Technology Inc. was used as the cone driving tool. It meets the dimension limits in the centrifuge space while fulfilling the criteria of maximum required force. The actuator is 110 mm long and provides maximum penetration displacement of 75 mm. The position and the motion of the piezocone were controlled remotely using a National Instrument VI. Figure 5.3 illustrates the schematics of the actuator and its load capacity at different speeds. Based on the graph, it is possible to push the cone with a rate of 0.12- 0.18 in/sec (3- 4.6 mm/sec). Based on the study by Corte et al (1991), the rate of penetration in the range of 0.5 to 10 mm/sec doesn't have a notable effect on the tip resistance. Thus, this range of penetration is acceptable. The piezocone driving system was mounted on the same frame used for infiltration system (Figure 5.4).
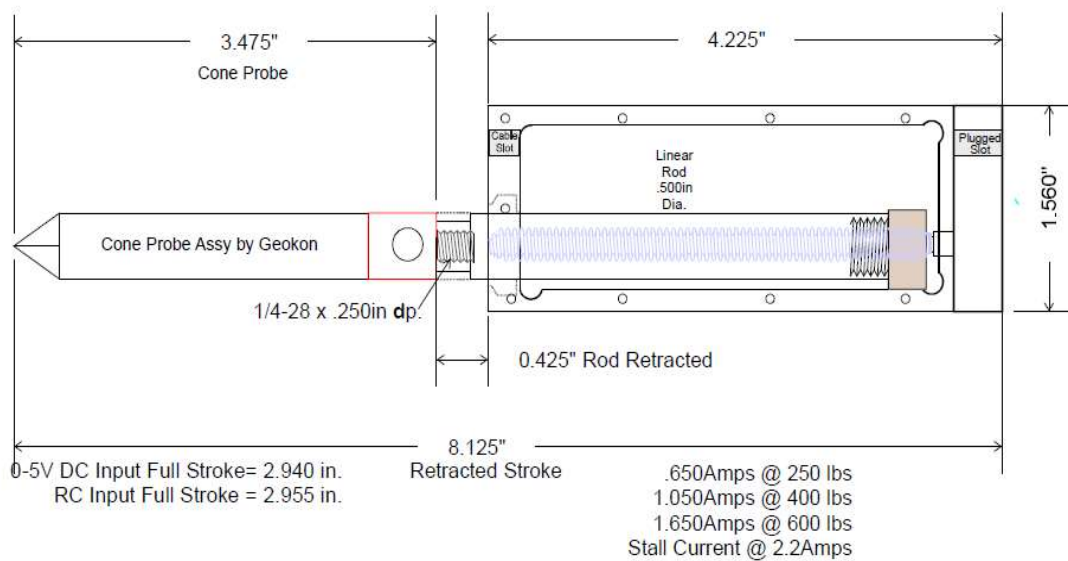
(a)
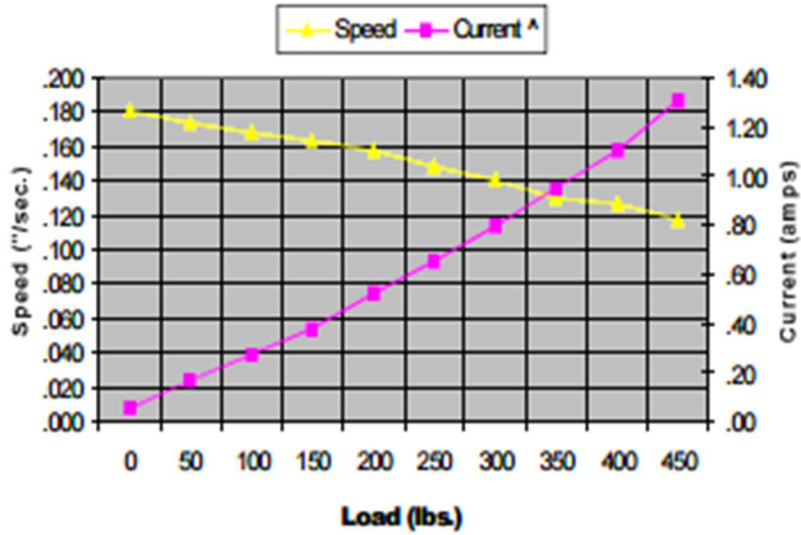
(b)

Figure 5-3 Actuator (a) Schematic (b) Load capacity at different speeds
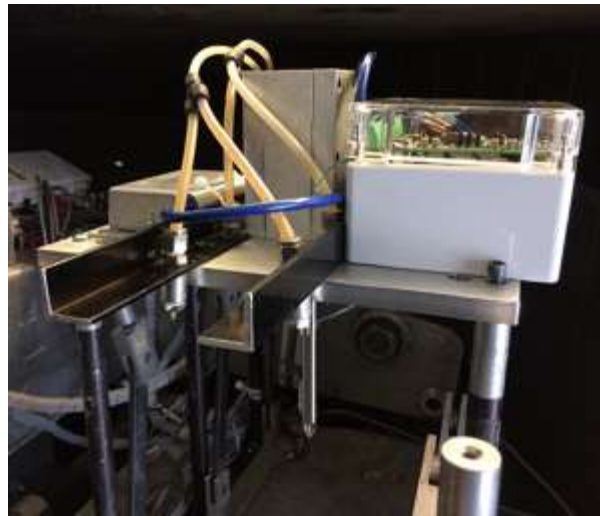
Figure 5-4 Piezocone guiding frame

The data acquisition system of the centrifuge facility was mounted on the center of arm and communicates to a computer located in the control room through a National Instrument PXI/CXI system with an embedded controller, which was running in LabView realtime module to control the output signal generation (cone penetration and infiltration system control) and input data measurement (PPTs, dielectric and cone load-cells measurement).

5.4 **Calibration of Load Cells**

It was necessary to calibrate the piezocone load cells prior to penetration tests. The raw reading of these load cells is called digit. It doesn't have any physical meaning and is just a deviation of the range of the force that load cell is capable of measuring. Thus, using a linear relation, it can be converted into the actual force. Calibration of these vibrating wire force gages were done in three steps. First, the cone was loaded through the gage tip which resulted in both front gage (tip resistance) and rear gage (total resistance) readings (Figure 5.5). In the second step, the skin friction was loaded throughout the front and rear gages segments, which showed that the tip load is decoupled from the skin friction load (Figure 5.6). In the third step, several loading-reloading loops were applied both to front gage and rear gage which made it possible to generate the relation between force gage readings and the actual force (Figure 5.7). These relations will be used later during CPTs to transfer the readings into the actual measured force.
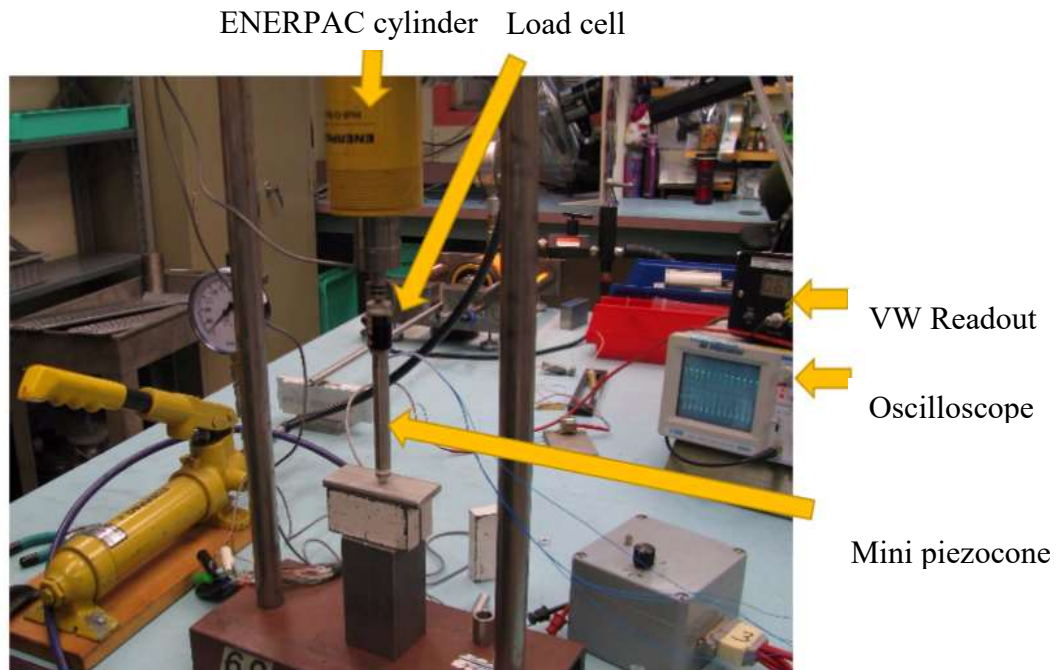
(a)
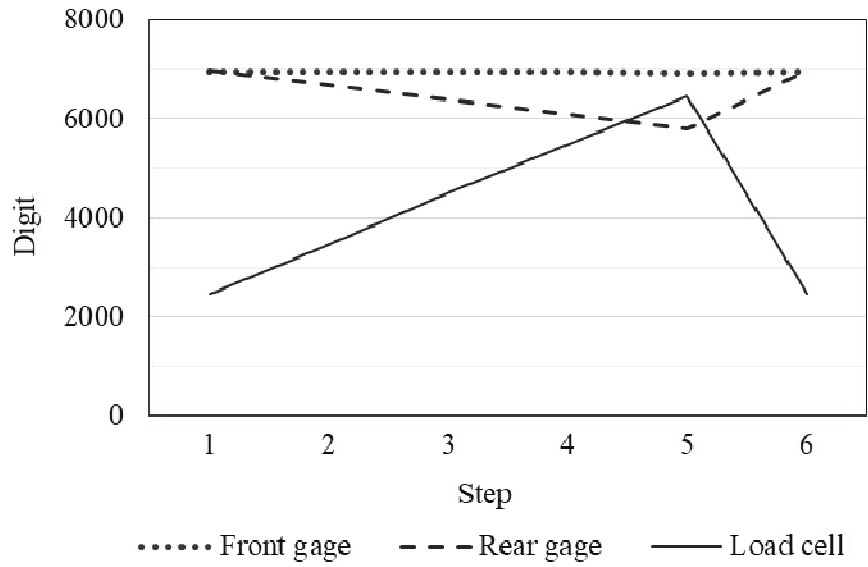
(b)

Figure 5-5 Load cells calibration (axial loading through gage tip) (a) set-up (b) generated graph

(a)
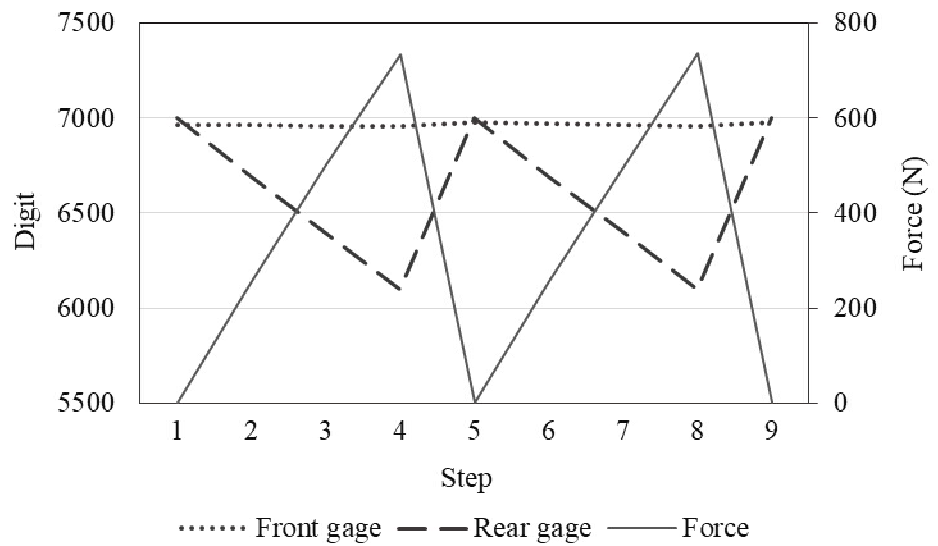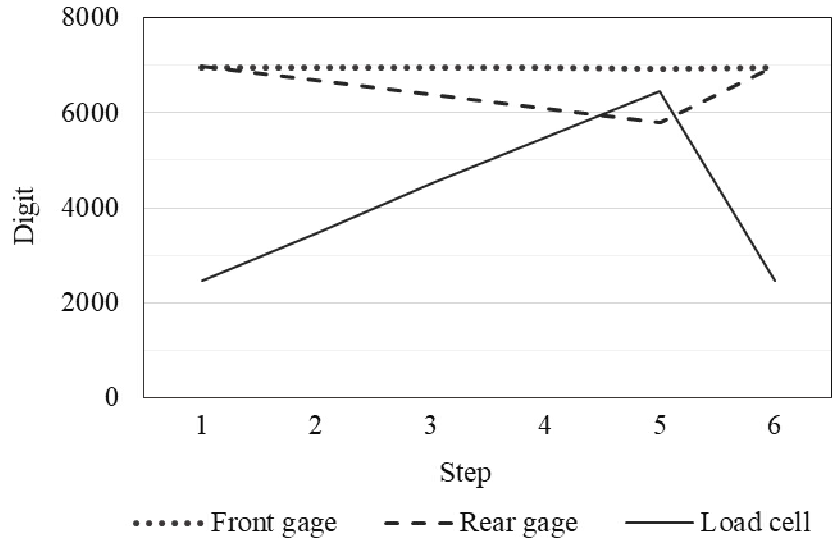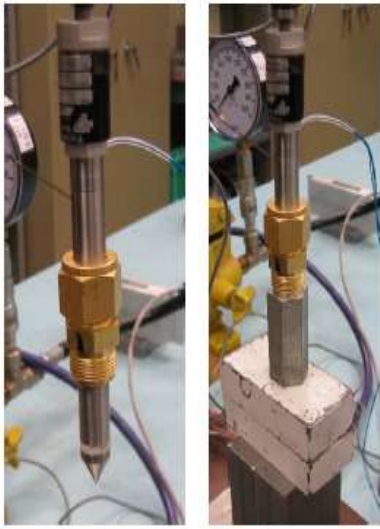
(b)

Figure 5-6 Load cells calibration (a) skin friction loading from front segment (b) skin friction loading from rear segment
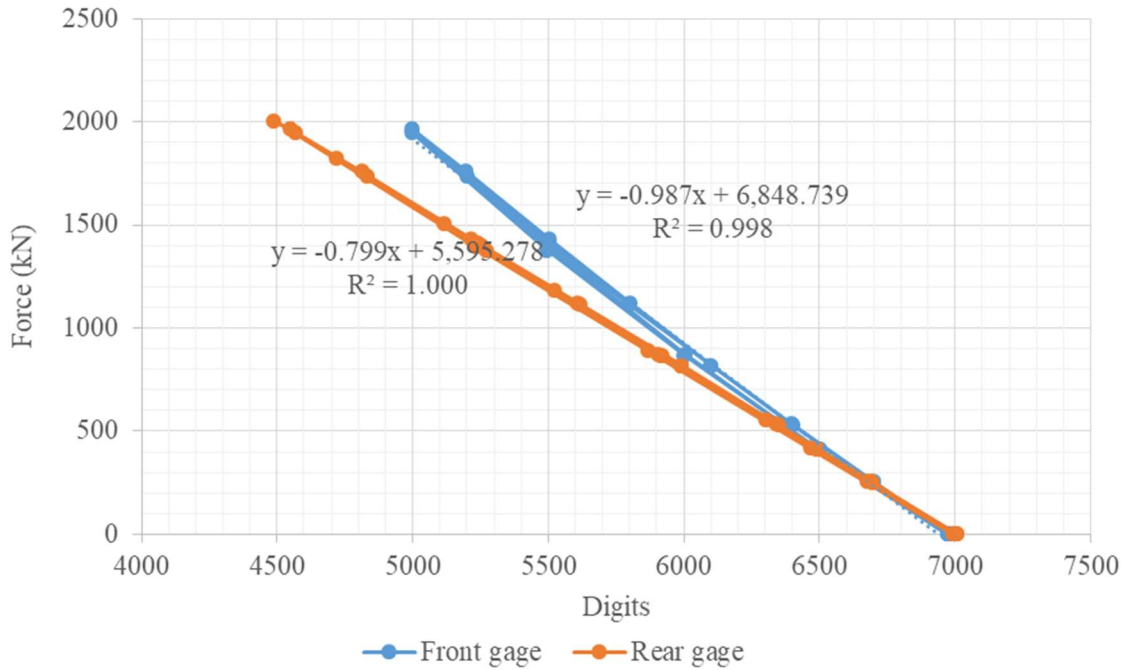
Figure 5-7 Vibrating-wire force gage calibration graph

5.5 Saturation and Calibration of Pore Pressure Transducer

Before any calibration, the transducer should be saturated. In the following sections, the saturation and calibration processes of this transducer are explained.

5.5.1 Saturation of transducer

As explained before, the cone porous stone is connected to the transducer with a narrow tube. In order to make an accurate measurement of water pressure the whole pressure transfer path including the water chamber, the tube, and the transducer itself should be saturated. The saturation includes de-airing and filling all the path from the porous stone to the transducer with de-aired water. Figure 5.8 shows the cone saturation set up. This task was done in three steps. In the first step, the cone was placed inside a sealed chamber connected to the vacuum. The vacuum was applied until the air in the chamber and the porous stone and connecting tube were removed. In the next step, the chamber was filled with de-air water up to 50% of its volume and vacuum was applied so that any air in the water or in the cone were removed. In the last step, pressure was applied to the chamber to make the water flow into the cone. In addition, there was a screw on the transducer which should be opened a little bit so that water could flow out and extract any trapped air bubble. This made the saturation process much faster and more efficient (Figure 5.9). However, it was possible that some air bubbles were trapped in the tube and in this case, the pressure was disconnected and instead vacuum was applied to make the air bubbles removed from the porous stone. It may be needed to do this procedure (step two and three) several times until no air bubbles exist.

Connected to vacuum and pressure

Cone tip
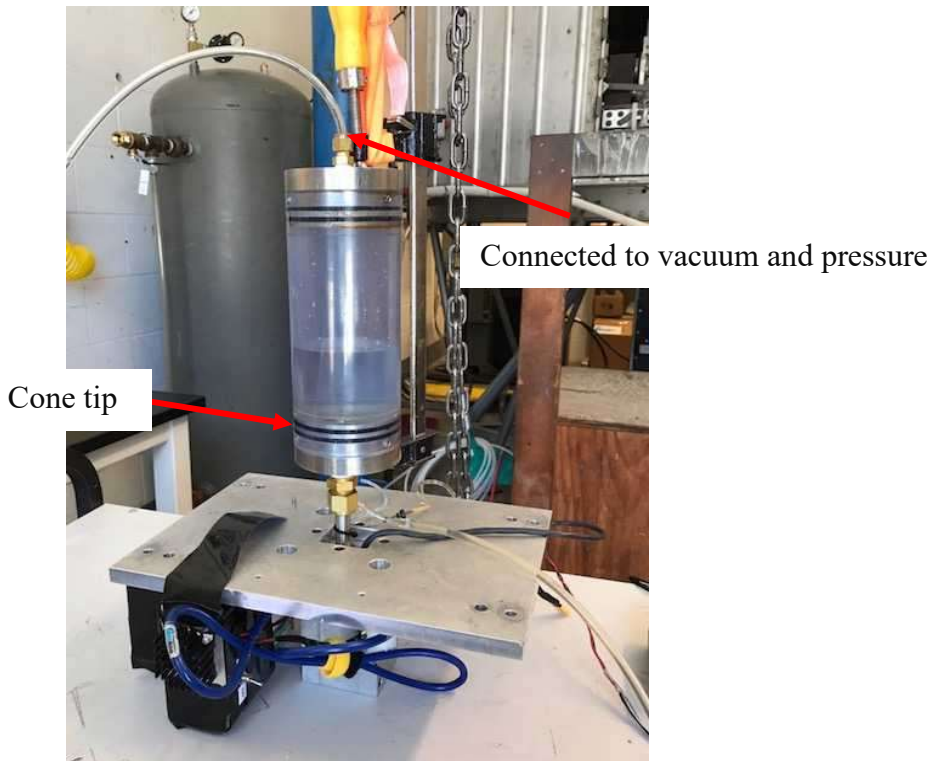
Figure 5-8 Saturation set up of the miniature piezocone

Figure 5-9 Small screw on transducer

5.5.2 Calibration of transducer and evaluation of porous stone performance

Before explaining the calibration procedure, there are couple of points that should be explained. The first point is about pressure correction. As explained before, the pore pressure was measured using a transducer outside the cone. Thus, the distance between the cone tip and the transducer is included in the measurements as well. Figure 5.10 shows this relation. The reading includes both porous stone pressure and the pressure due to head difference between the cone porous stone and transducer (Eq. 4.1). Thus, readings should be corrected accordingly to have the actual pressures at cone tip using Equation 5.1.

$$P_{reading} = P_{porous\ stone} - P_{(transducer-porous\ stone\ distance)} = \gamma_w.d_1 - \gamma_w.d_2 \rightarrow$$

$$P_{porous\ stone} = \gamma_w.d_1 = P_{reading} + \gamma_w.d_2 \qquad \text{Eq. 5.1}$$

where, $P_{reading}$ is the transducer reading, $P_{porous\ stone}$ is the actual pressure at cone porous stone, $P_{(transducer-por\ \ stone\ distance)}$ is the pressure due to distance between the cone porous stone and transducer, d_1 is the pressure head at porous stone, d_2 is the distance between cone porous stone and transducer and γ_w is the unit weight of water.
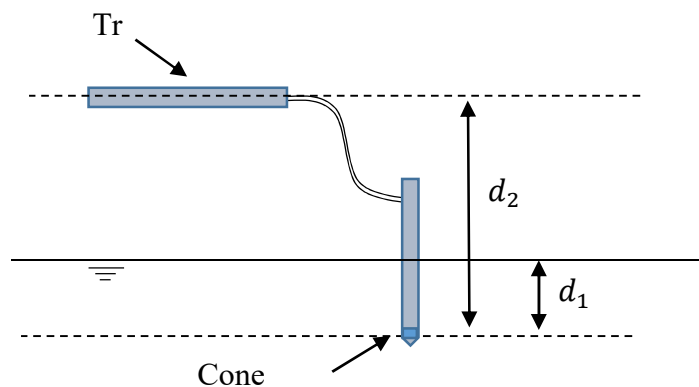
Figure 5-10 Transducer – porous stone distance

It should be mentioned that in centrifuge testing the unit weight of water is not constant due to g-level change in depth, and so the hydrostatic water pressure distribution is not linear any more. In addition, the distances between the cone tip and transducer is affected with the g-level change as well. Thus, these effects should be considered when using Equation 5.1 for correction of data. The correction procedure is explained in more detail in section 6.1.1.

The second point is about porous stone adjustment. The cone porous stone is shown in Figure 5.11. It should be glued from bottom side to the cone tip and completely sealed. However, the top side of the porous stone which is fastened into the cone body, shouldn't be glued as it would obstruct the water flow into the cone. Meanwhile, the air should be prevented to flow into the cone to keep it work properly and measure the pore pressure. It was challenging to find a solution for this issue, detail of which is explained in the following.
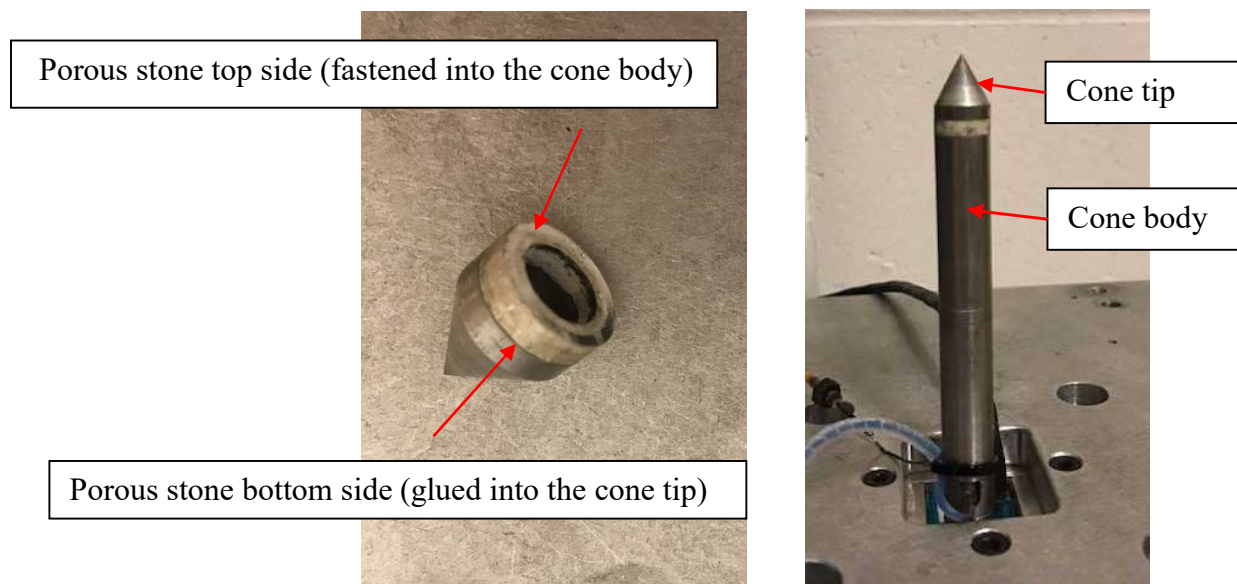
Figure 5-11 Cone porous stone adjustment

5.5.2.1 Transducer calibration

The calibration of transducer was done in 3 steps. First, applying positive pressure, second, changing the water head and third, changing the porous stone to transducer distance.

As the first step, positive pressure was applied up to transducer capacity (1MPa) incrementally and the measurements were recorded. The calibration graph was developed relating the reading into the corresponding pressure. This graph is shown in Figure 5.12.
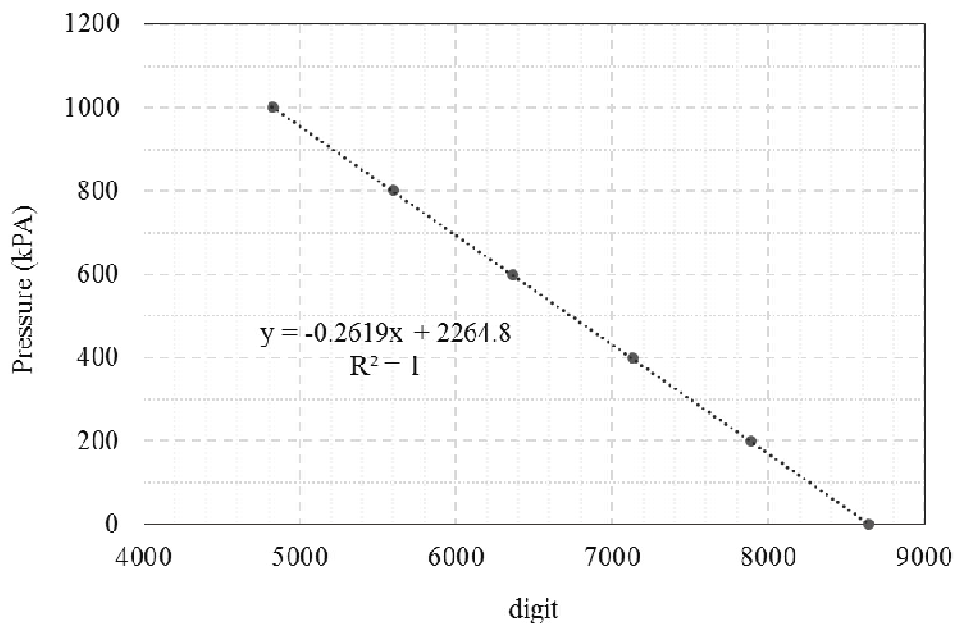
Figure 5-12 Transducer calibration graph for positive pressures

Second, water head was changed while the cone was submerged in a chamber filled with water and both cone and transducer were kept in place so that the distance between the cone and transducer was kept constant. The water head was changed by connecting the chamber to a hanging column. The relation between the transducer reading and the generated pressure is shown in Figure 5.13.

As it is shown, both the slope and x-intercept of the graph is similar to the previous calibration graph. In addition, it proves that the transducer is able to read negative pressures with a good accuracy which is required for tests in unsaturated soils.

The graph shows Pressure (kPA) on the y-axis (from -4 to 8) versus digit on the x-axis (from 8610 to 8660), with a fitted line:

$$y = -0.264x + 2{,}283.445$$
$$R^2 = 1.000$$
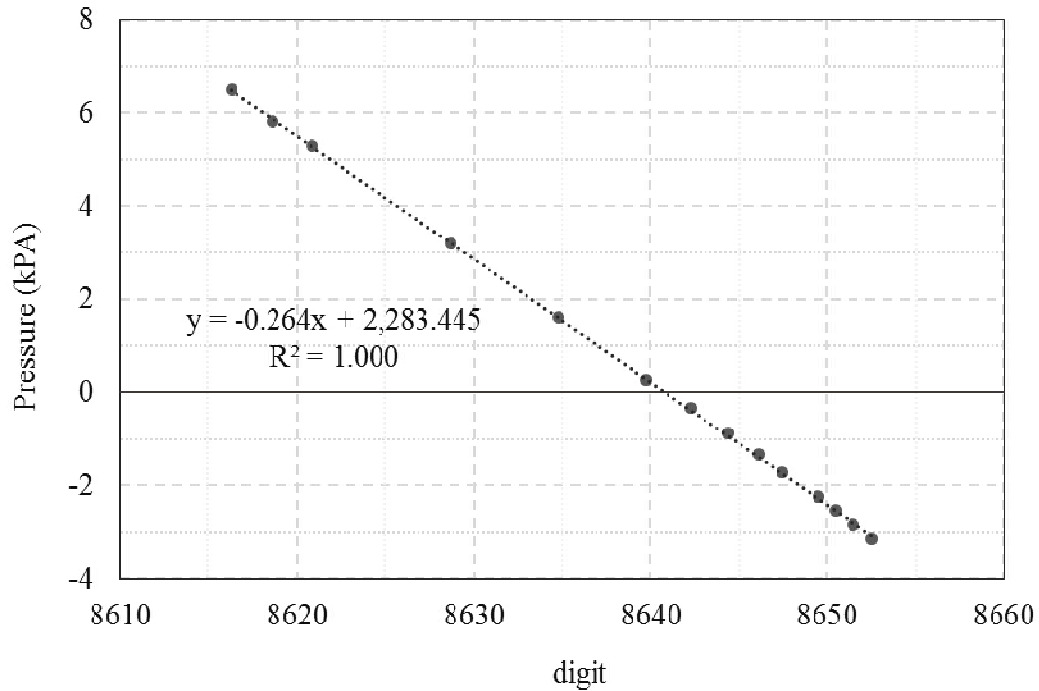
Figure 5-13 Transducer calibration graph (changing the water head)

And finally, the transducer elevation was changed while the cone was submerged in the water. The transducer readings were compared with the generated hydrostatic pressure and the process imposed both positive and negative pressures.
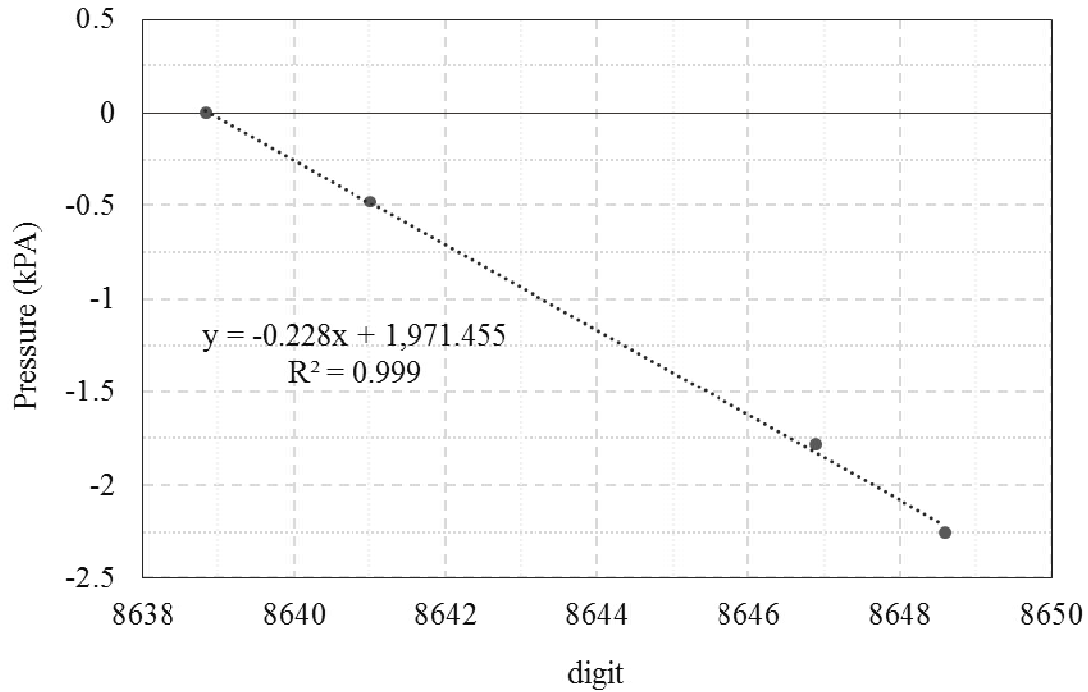
Figure 5-14 Transducer calibration graph (changing transducer elevation)

5.5.2.2 Evaluation of porous stone performance

Two methods were examined to find an efficient way to prevent air flow into the cone from the gap between the top side of the porous stone to the cone body (Figure 14).

The first option was using an O-ring shape geotextile with small thickness. The thickness should be small enough so that the cone tip could be fastened completely to the cone body and load cells work properly. However, by trying this, it was observed that the geotextile was moving into the cone inner area during the tests and clog the water flow path. In addition, it was not possible to glue the geotextile into the cone as there was not enough area and there was possibility of covering the whole porous stone area with glue and seal the water flow path. Thus, this option was not used.

The second option was using vacuum grease to seal the top side of the porous stone to the cone body. A tiny amount of vacuum grease was applied on porous stone top surface (about half

68

of the ring-shape area) and also the outer surface of the cone where the porous stone is fastened into the cone body (figure 4.15). Then, the cone performance was examined by performing tests in water at 40g to check if porous stone remain saturated during spinning and before the test starts and if vacuum grease doesn't clog the water flow path.
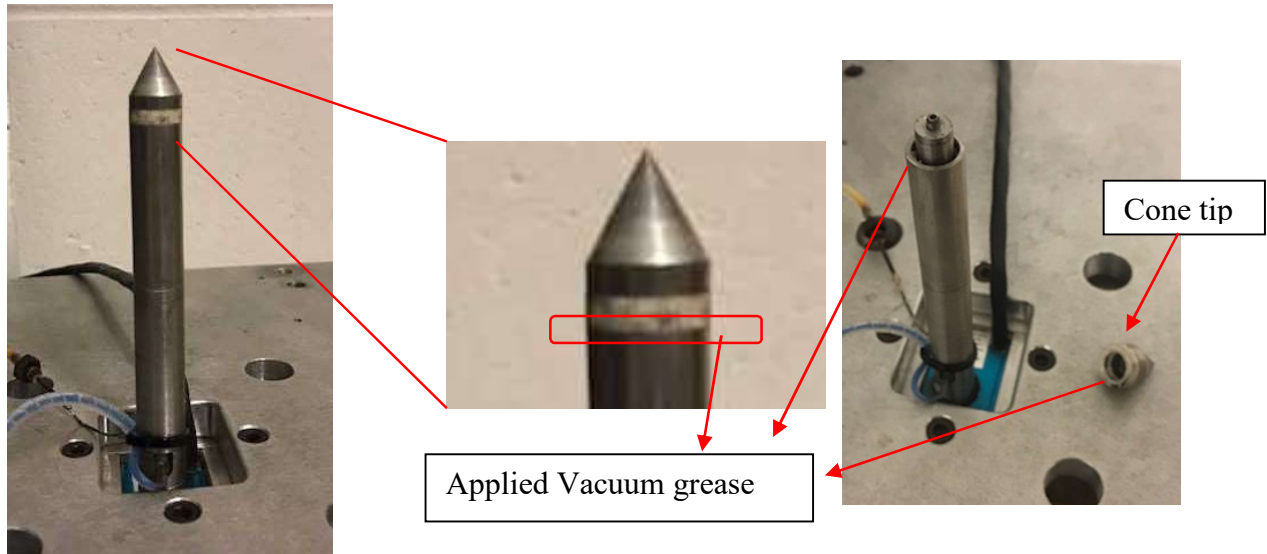
Figure 5-15 Porous stone sealed area with vacuum grease

For the penetration test in water, a flexible plastic bag was put inside the container and it was filled with water. One pore pressure transducer (PPT) was put at the bottom of the container to record the hydrostatic pressure in order to check if any leakage happens. The detailed information about this sensor is presented in section 5.4.

The cone was outside the water during spinning and was penetrated into the water after reaching 40g (at 1 m radius). Figure 5.16 shows the transducer reading raw data. As it is shown, the transducer responds to the change of the hydrostatic pressure. It should be mentioned that the negative value of pressure readings is due to second term in Equation 5.1. Using Equation 5.1, the readings are corrected and presented in Figure 5.17. As it is shown, the transducer is capable of

measuring the hydrostatic pressure and the predicted response is close to hydrostatic pressure. This proves that centrifuge spinning doesn't cause any drying of the porous stone and using vacuum grease for sealing is fine and it doesn't affect the cone response.

However, there is small difference between the measured pressure and the hydrostatic pressure. For clarification, the results are shown as a function of penetration depth in Figure 5.18. As it is shown, the transducer predicts the pressure with 2 kPa difference at the maximum penetration depth. Using a transducer with lower maximum capacity (the current transducer has a capacity of 1 MPa) may increases the accuracy of measurement and decreases this error.
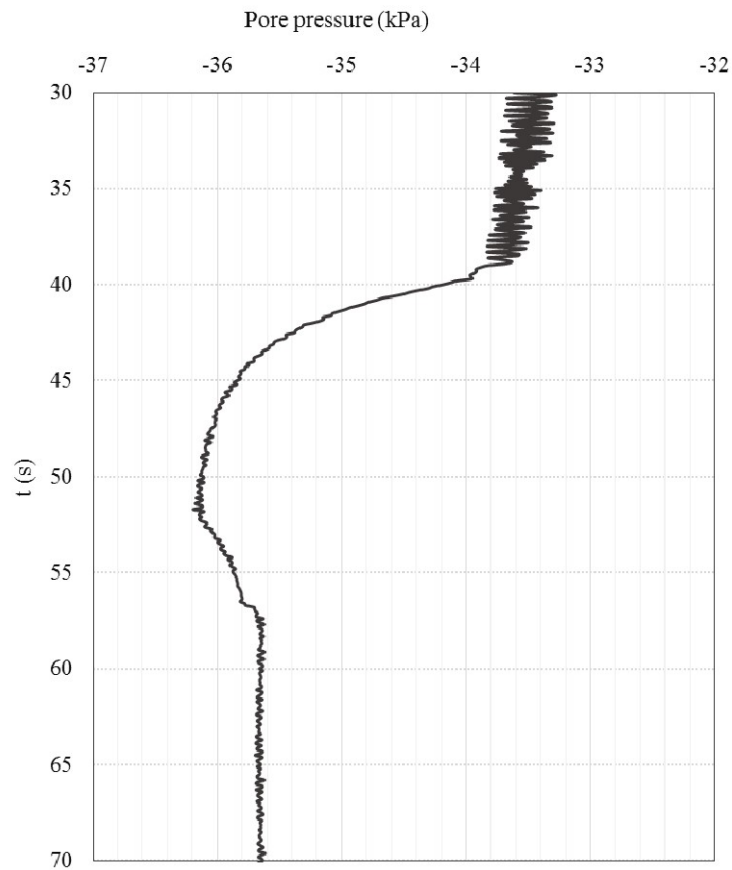
Figure 55-16 transducer reading raw reading data
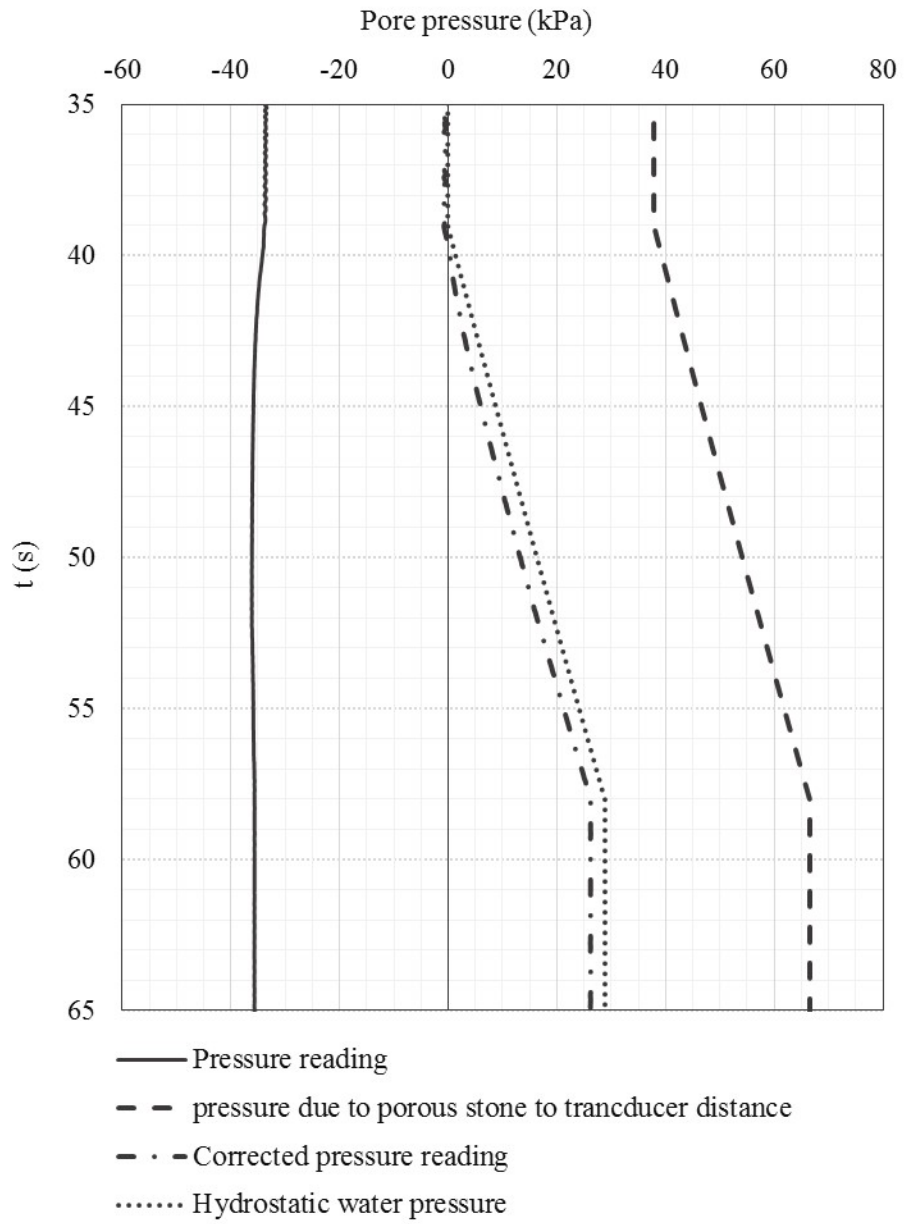
Figure 5-17 Transducer pressure reading correction procedure compared with hydrostatic water
pressure
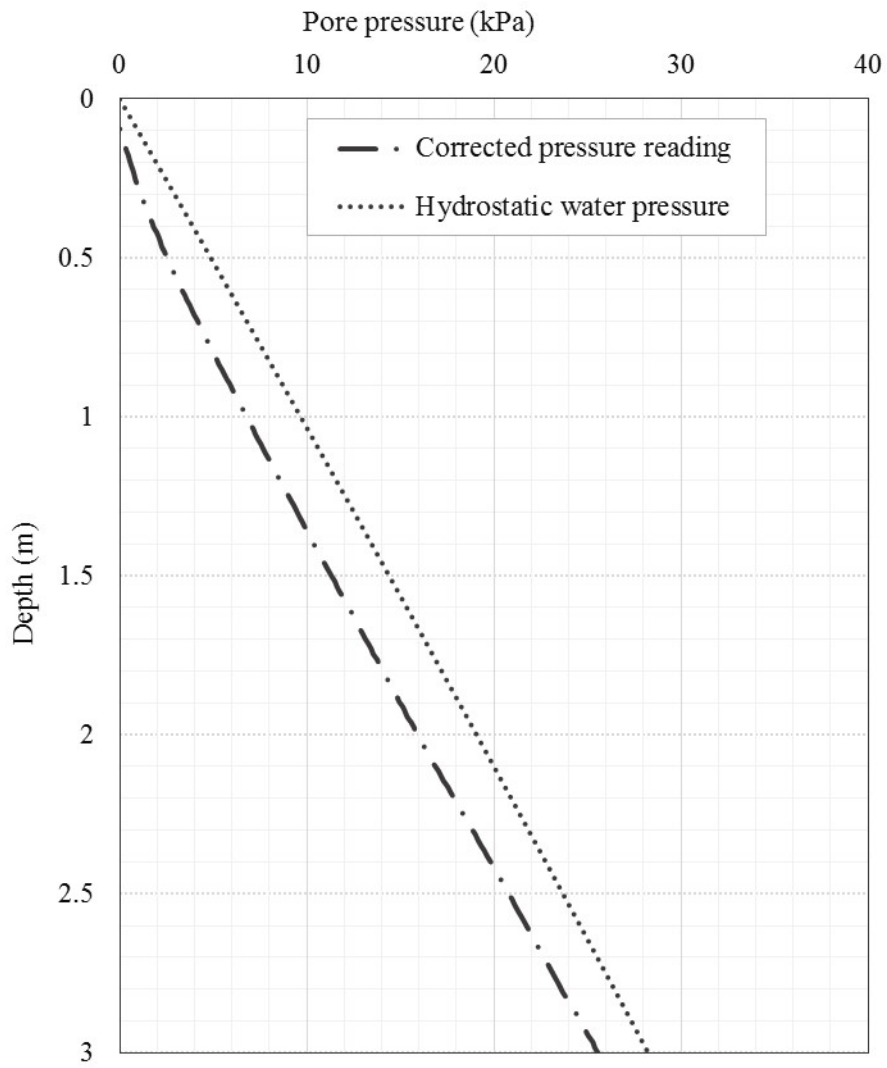
Figure 5-18 Transducer corrected pressure reading in comparison with hydrostatic water pressure profile

Chapter VI

Centrifuge Penetration Testing Procedure

6.1   **Centrifuge Facility**

The 5 g-ton centrifuge facility at the University of New Hampshire was used for this study (Figure 6.1). The centrifuge is a Model A1030 Genisco g-accelerator and consists of an aluminum-alloy rotor arm with a hanging platform at one end and counterbalance weight on the other. The radius of center of the rotation to the platform in fully extended position is 1 m. The absolute acceleration of the basket is 175g and it is capable of carrying 100 kg or 30 kg payload up to 50g or 175g respectively using the 0.46 by 0.59 m magnesium mounting frames at both end of the arm. The power supply is from Sabina Electric and Engineering RG 2600 and the control system is National Instrument PXI/SCXI system with an embedded controller, which is running in LabView real time module. Detailed information on this facility can be found in Ghayoomi and Wadsworth (2014).

Figure 6-1 Centrifuge facility of University of New Hampshire

6.2 Soil Container

A laminar container with an inside length of 36 cm, width of 18 cm and depth of 27 cm was used in this study. In order to allow free drainage of water, the container base plate was replaced with an outflow control aluminum plate with a network of 14 drainage ports. The outflow control plate has a 6.35 mm thick indentation at its top surface where a gravel layer was placed as the drainage layer and was overlain by a 10-mil nonwoven geotextile filter to separate the gravel and overlying sand layer.
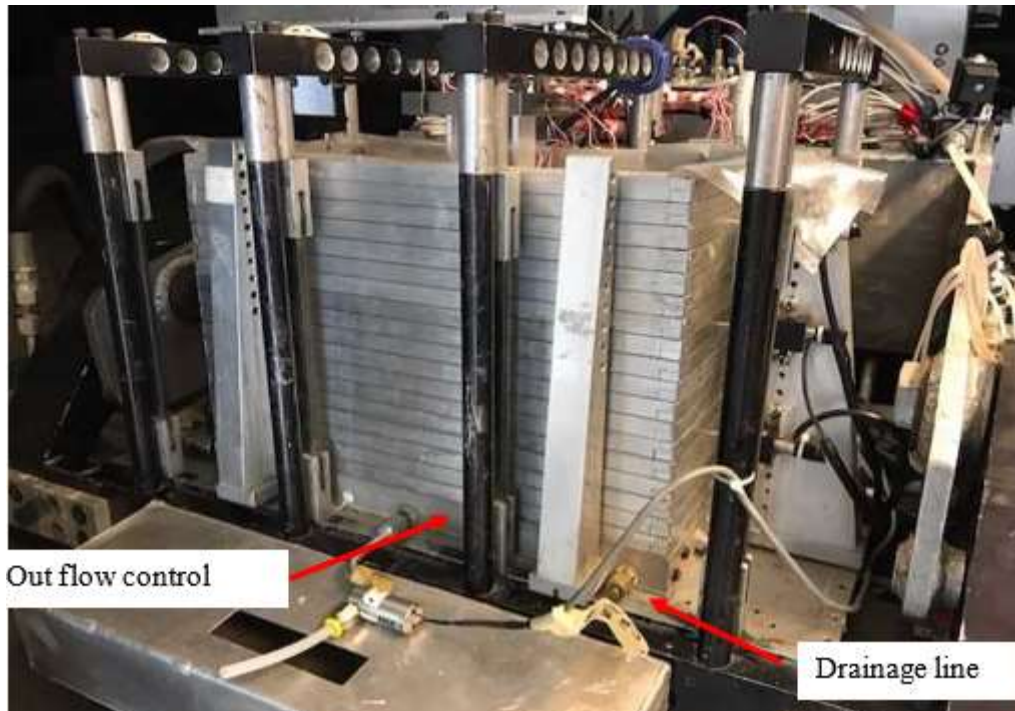
Figure 6-2 laminar container and drainage system

6.3   Infiltration System

The infiltration set up consists of eight fog-spray nozzles mounted on two horizontal steel brackets which are suspended across the length of the container above the container. Each spraying nozzle supply a cone of mist and they are arranged on the steel bracket so that the spray covers the whole area of soil surface and uniform coverage of flow. The produced spray distribution from the nozzles is shown in figure 6.3. Having different nozzles, different water discharge can be achieved. For this study, 1/8 PJ20 nozzle which produces degree of saturation between 45% and 60% was used. This nozzle is shown in figure 6.4.
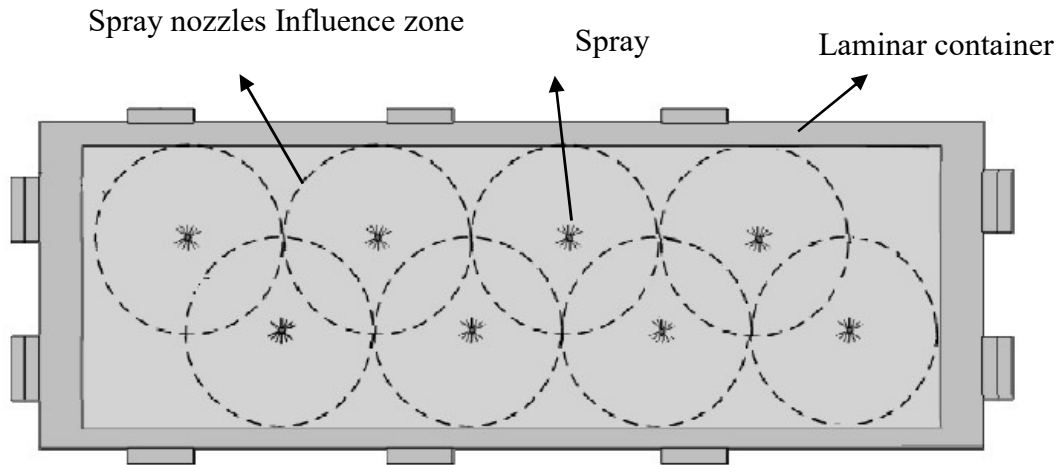
Figure 6-3 Schematic of nozzle arrangement and sprayed water distribution

Figure 6-4 Spray nozzles 1/8 PJ20 used for this study

6.4 **Instrumentation**

In this study, two types of instruments including dielectric sensors and pore pressure transducers (Model EPB) were used for measuring the volumetric water content and pore water pressure, respectively. Figure 6.5 shows the schematic of the most complete set of instrument arrangement. Some tests missed one or more of these sensors depending on the desired results and availability of sensors at the time. The close-up pictures of these instruments are shown in Figure 6.6.

The dielectric sensors are from Decagon Device, model EC-5 which are used to measure the change of volumetric water content with depth in the sand layer. The sensors were placed

horizontally at three depths of 7.25, 5 and 2.75 in from the container top edge and with distance of 3 in from the container sides.

Pore Pressure Transducers (Model EPB) were used to measure the hydrostatic pore pressure and generation and dissipation of excess pore pressure in the soil layer due to the cone penetration. This modified version of pore pressure transducers could be used to measure the values of matric suction as long as the matric suction magnitude is less than 60 kPa and the sensor porous stone is initially well-saturated (Muraleetharan and Granger 1999). Theses sensors should be saturated every time before application and calibrated once in a while before performing a set of tests. The saturation includes placing the sensors inside a chamber filled with water and applying vacuum for about three hours. The calibration includes connecting the saturation chamber to the hanging column and recording the pore pressure transducers readings in different water heads. Having those data, calibration graph could be estimated for each sensor. Figure 6.7 shows the saturation and calibration set up. It should be mentioned that, although the slope of the calibration line remains constant in time, the x-intercept value might change. Thus, before placing the sensor in the soil, the zero pressure should be read again and the x-intercept value should be corrected accordingly.

PPTs were placed similar to the dielectric sensors in three depths of 7.25, 5 and 2.75 in, from the soil surface.
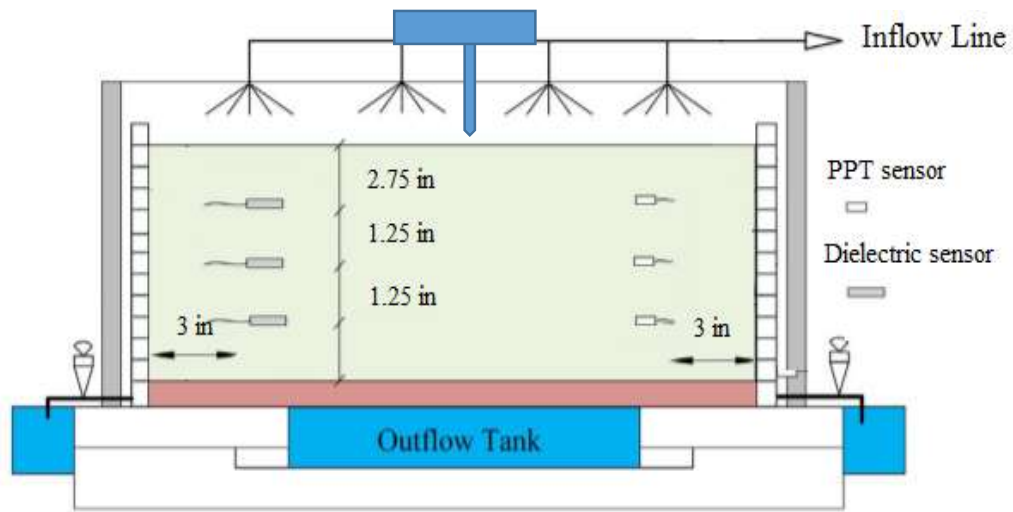
Figure 6-5 Schematic of instruments arrangement
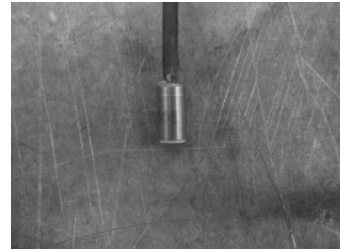
(a)   (b)

Figure 6-6 Measurement instruments (a) EC-5 Dielectric Sensor (b) PPT

(a)   (b)

Figure 6-7 Pore pressure transducers (PPTs) saturation and calibration set up (a) saturation chamber (b)

hanging column

6.5 Tested Material

Ottawa F75 sand was used for this study. It is a fine grained sand with high amount of silicon dioxide ($SiO_2 > 98\%$). It was originally obtained from the sandstone in Ottawa, Illinois. However, it is currently industrially manufactured. The sand is naturally rounded and composed of nearly pure quartz. Figure 6.8 shows the grain size distribution curve of the sand of two different batches which were used for this study. The properties of the two are almost the same but they are a little different in their fine content. Table 6.1 summarizes the physical properties of this sand while Soil-Water Characteristic curve (SWRC) of Ottawa sand is also shown in figure 6.9.
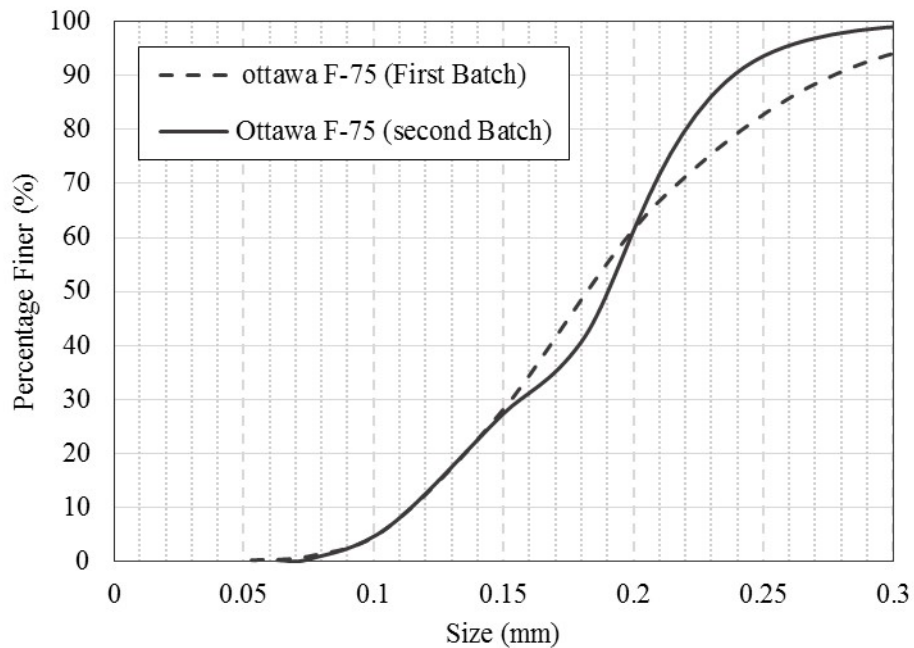
Figure 6-8 Grain size distribution curve of two different batches of F75 Ottawa sand

Table 6-1 Geotechnical properties of Ottawa sand

Property	value
Specific Gravity	2.65
e_{min}, e_{max}	0.486, 0.805
ρ_{min}, ρ_{max} (kg/m^3)	1468, 1781
Coefficient of Uniformity	1.83
Coefficient of Curvature	1.09
Friction Angle (°)	40
Poisson ration	0.38
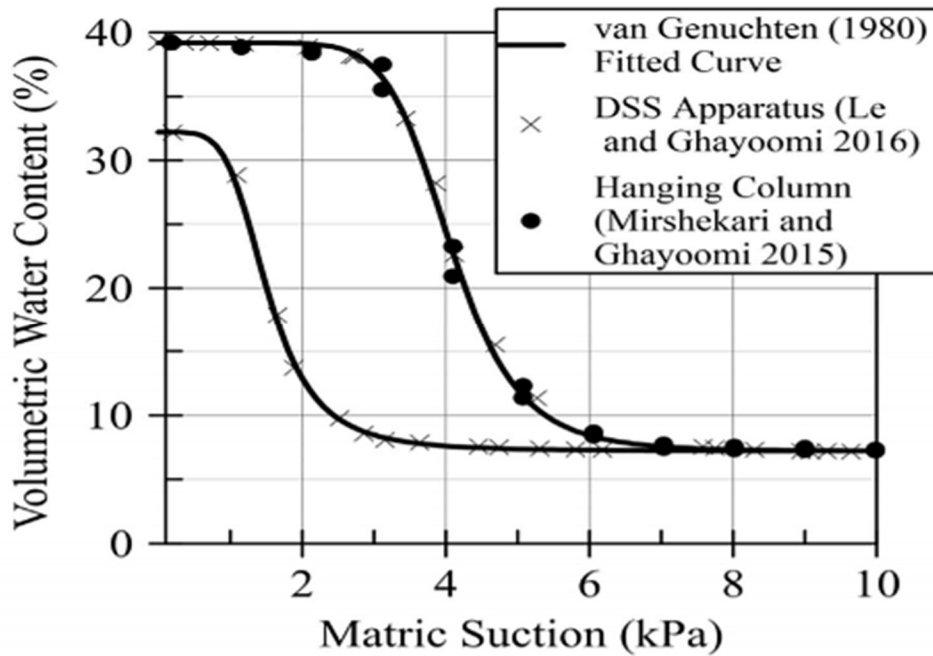
Figure 6-9 Soil-water retention curve of Ottawa F75 sand (Mirshekari & Ghayoomi 2017)

6.6   Specimen Preparation

The container explained in Section 6.2 was used for the tests. However, in saturated tests, any leakage of water should be prevented. A flexible plastic bag was used for this purpose which is shown in Figure 6.10.a. In unsaturated tests, it is needed to avoid any leakage from the side of the container while having water drainage from the bottom of the container. For this purpose, a

flexible plastic sheet was glued to the inside of the bottom drainage plate using E6000 industrial

adhesive with 48 hours curing which is a water proof glue suitable for both aluminum and plastic

(Figure 6.10.b).

(a)

(b)

Figure 6-10 Sealed container for (a) dry, saturated tests (b) unsaturated tests

Dry pluviation method was used in order to prepare the soil samples. Detail description of

this method can be found in ASTM D4253-83. A funnel was used for this purpose and different

openings and heights of sand raining were tried. Having the dimensions of the container and the weight of the soil, it is possible to calculate the relative density of each specimen. Based on these data, for preparing the sample with a relative density of 26%, it is needed to rain the sand through the funnel with an opening of 5 mm, from 100 mm above the soil surface.

Different instruments including dielectric sensors and PPTs were placed at different depths during pluviation. This procedure is shown in Figure 6.11. The connecting wires were passed out of the top of the box, and were taped to the sides of the container. When placing the PPTs, the placement area should be saturated locally to avoid desaturation of the porous stone on the tip of the pore pressure transducer. Then, pluviation was continued to reach another level of instrument placement.
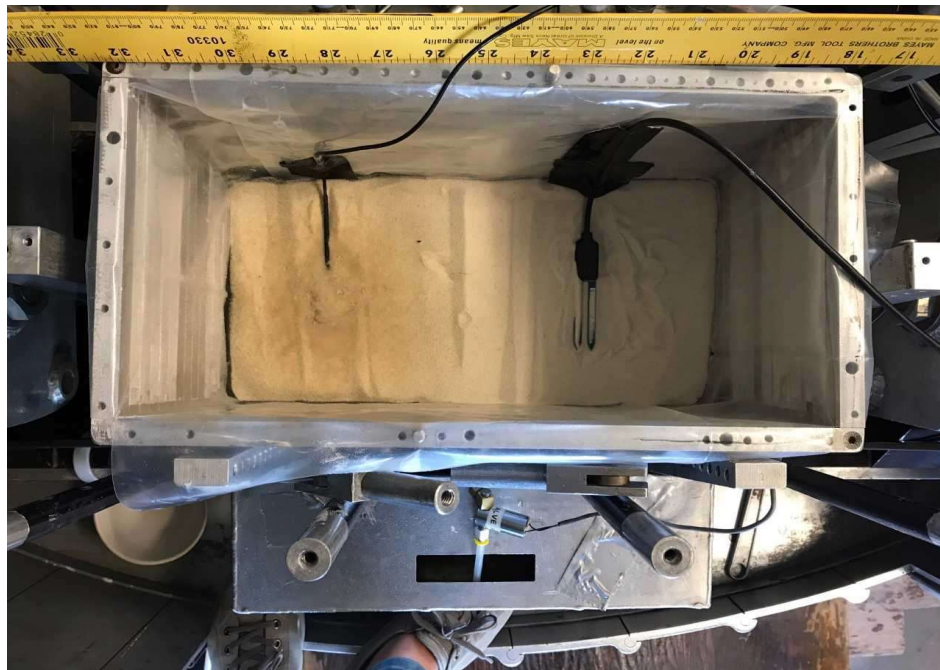
Figure 6-11 Placement of dielectric and PPT sensors

After preparing the sand layer and placing the instruments, the soil surface was leveled to obtain the desired specimen depth. For saturated and unsaturated tests, it is needed to make the

specimen saturated before the tests. The saturation was done from the bottom of the sample. In saturated samples, a tube was placed at the bottom of sample and was taped to the side of the container which was connected to water reservoir. In unsaturated samples, saturation was done by connecting the drainage line into the de-air water reservoir. It should be mentioned that the height of water in the water reservoir should not be more than two times of the soil sample height to avoid sand boiling. The saturation can be monitored by checking the dielectric sensors' readings embedded at different depths. After the saturation was completed (the water reached the sand surface, the water reservoir was disconnected and the sample was placed inside the centrifuge using a crane and high strength straps. Figure 6.12 shows the saturation set up used in this study and Figure 6.13 shows the crane system.

Figure 6-12 Saturation set up
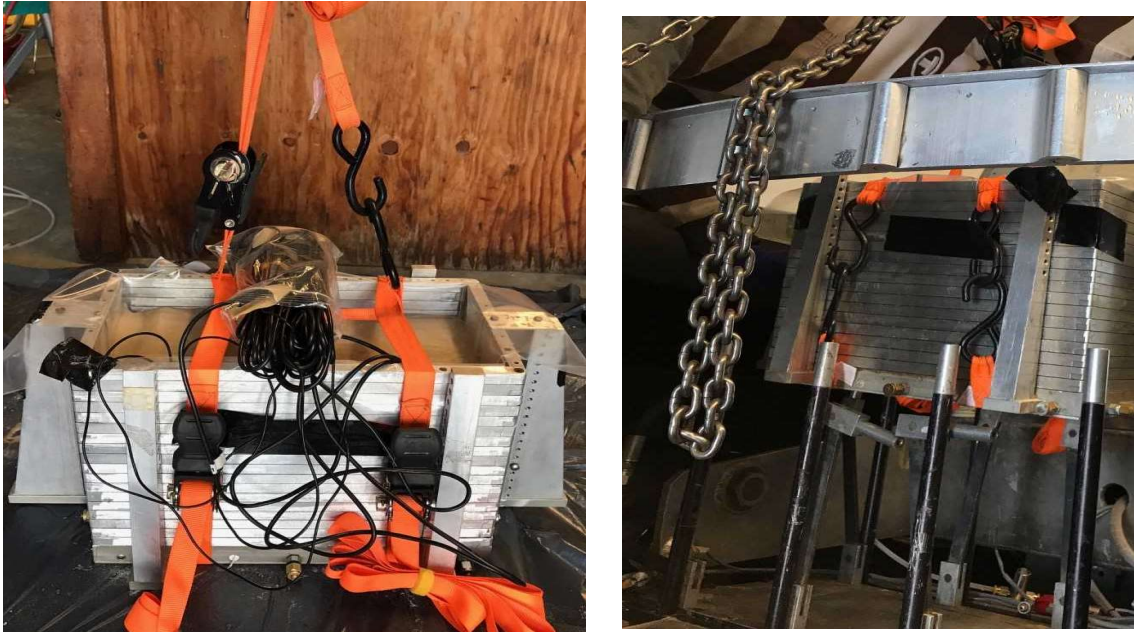
Figure 6-13 placement of soil sample in the centrifuge using crane system

After preparing the sample and placing it inside the centrifuge, the miniature cone was placed on top of the sample and all wires were connected. Then pizeocone load cells were checked for proper response on the data acquisition system computer. A small force was applied by hand and the response of load cells was checked in the computer. Any hardware failure will be readily noticed. After checking the performance of pizeocone, it was fastened and all wires were organized to be tight in place during centrifuge spinning. In unsaturated tests, the spray nozzles should be placed on top of the sample as well. The calculated counterbalance weight was then put in the centrifuge basket. The position of the soil surface was recorded and data acquisition system was checked for proper functioning by checking the dielectric and PPTs readings.

6.7   Cone Penetration Testing

The test was started by spinning up the centrifuge up to a target gravitational acceleration of 40, defined at the cone tip at the end of full penetration of 3 in. For this, the centrifuge was spun

up to 45g from control system (which shows the g-level at 1 m radius). The required correction should be made to the depth measurements considering the effect of different g-level at different distances from centrifuge center during penetration which is explained in Section 6.2. In saturated and unsaturated tests, after reaching the desired g-level and before penetration, the dielectric and PPT readings were recorded to check if there is any leakage from the container.

In unsaturated tests, the next step was opening the inflow and outflow solenoid valves to generate a steady state infiltration. Here, the valves were opened 2 turns at 20 psi pressure which gives an infiltration rate of 10^{-3} liters/min and reaches to the degree of saturation of 0.36 (corresponding to matric suction of 3 kPa). The steady state condition was assessed when the dielectric sensors and PPTs at different depths measure the same volumetric water content and pore pressure which proves a uniform suction profile in depth. After reaching the steady state condition, the sample was ready for the cone penetration.

The operation of the piezeocone driving apparatus was controlled through a motion control system remotely. The system was operating through the Lab view in which the input value had a linear relation with the penetration depth. The minimum given value could be zero and the maximum value could be 4 which impose penetration of 0 and 3 in to the cone respectively. Some tests were performed with a continuous drive while some others involved penetration in three or more intervals. The whole penetration length (3 in) took about 18 seconds to be completed which means the penetrations rate was about 4.25 mm/s. The cone tip resistance, total cone resistance, and pore water pressure were measured continuously. In addition, the dielectric and PPT readings were recorded before and after the test as well.

Before any analysis, it is required to have some corrections on the results. Details of these corrections, analysis and discussion of the test results are presented in chapter VII.

Chapter VII

Centrifuge Test Results and Discussion

7.1 Introduction

This chapter includes the results of CPT tests in different saturation conditions (including dry, saturated and unsaturated). It should be mentioned that these are proof of concept work testing the applicability and suitability of the developed cone. Further modifications are underway based on these results.

The cone penetration tests were performed on Ottawa sand from two different batches. As mentioned in section 5.5, the properties of the two are almost the same but there is a difference in their fine content. First set of tests was performed on Ottawa sand I, including two dry test, one saturated test and one unsaturated test while the second set of tests was performed on Ottawa sand II including one saturated test and one unsaturated test. It should be mentioned that for unsaturated tests, the same infiltration discharge was used to have the same degree of saturation (36%) in the samples and thus the same matric suction (3 kPa).

For easier presentation of the result, these tests are named as it is summarized in Table 7.1. In the following sections, the analysis steps and test results are presented.

Table 77-1 Cone penetration tests on different samples

Test name	Soil type	Saturation	Degree of saturation
S1-D1	Soil I	Dry	0
S1-D2	Soil I	Dry	0
S1-S	Soil I	Saturated	100 %
S1-U36	Soil I	Unsaturated	36%
S2-S	Soil II	Saturated	100%
S2-U36	Soil II	Unsaturated	36%

7.2   Analysis Steps

In this section, the corrections that should be applied on results before any further discussion is explained.

7.2.1   Penetration depth correction

The position of the piezocone from the soil surface during penetration was determined considering a constant penetration rate of 4.25 mm/s. Having the total penetration depth of 3 in, the penetration took 18 seconds to be completed. For tests with several intervals, it was required to pick the data corresponding to each interval duration among the recorded data to have the full penetration profile. Then, the penetration depth in prototype scale can be calculated having the gravitational acceleration at each depth (Equation 7.1) and using Equation 7.2.

$$g_z = \frac{r_z}{r_0} g_0 \qquad\qquad \text{Eq. 7.1}$$

where g_0 is the gravitational acceleration which is recorded by data acquisition system and r_0 is radius from centrifuge center. r_z is the distance from centrifuge center at depth of z from soil

surface and g_z is the corresponding gravitational acceleration. In this study, g_0 and r_0 are 45 and 1 m respectively.

$$z_p = z \cdot g_z \qquad\qquad \text{Eq. 7.2}$$

where z_p is the depth from soil surface in prototype scale, z is the depth from the soil surface at g=1 (no spinning) and g_z is the g-level at depth z calculated from Eq. 5.1.

7.2.2 Penetration resistance correction based on penetration test in water

During penetration tests in saturated tests, the cone was subjected to different g-levels. This means that the cone's own weight increases during the penetration and the buoyancy force acting on cone causes a compression force measured by the piezocone load cell. Thus, the measured force should be corrected by adding the weight correction (Δw). Result of the penetration test in water was used for this correction. Figure 7.1 shows the profile of measured cone tip force, total force and calculated sleeve force (subtraction of total force and tip force) during penetration test in water. Based on this graph, the cone tip force and sleeve force should be corrected using equation 7.3 and 7.4 respectively. In these equations, the reverse slopes of the equations shown in Figure 7.1 were used to develop the correction relation.

$$\Delta w_{tip\,force}(KN) = \left(\frac{1}{223.12}\right) d\ (m) = 4.5e^{-3}.d\ (m) \qquad\qquad \text{Eq. 7.3}$$

$$\Delta w_{sleeve\,force}(KN) = \left(-\frac{1}{285.47}\right) d\ (m) = -3.5e^{-3}.d\ (m) \qquad\qquad \text{Eq. 7.4}$$

Force (KN)
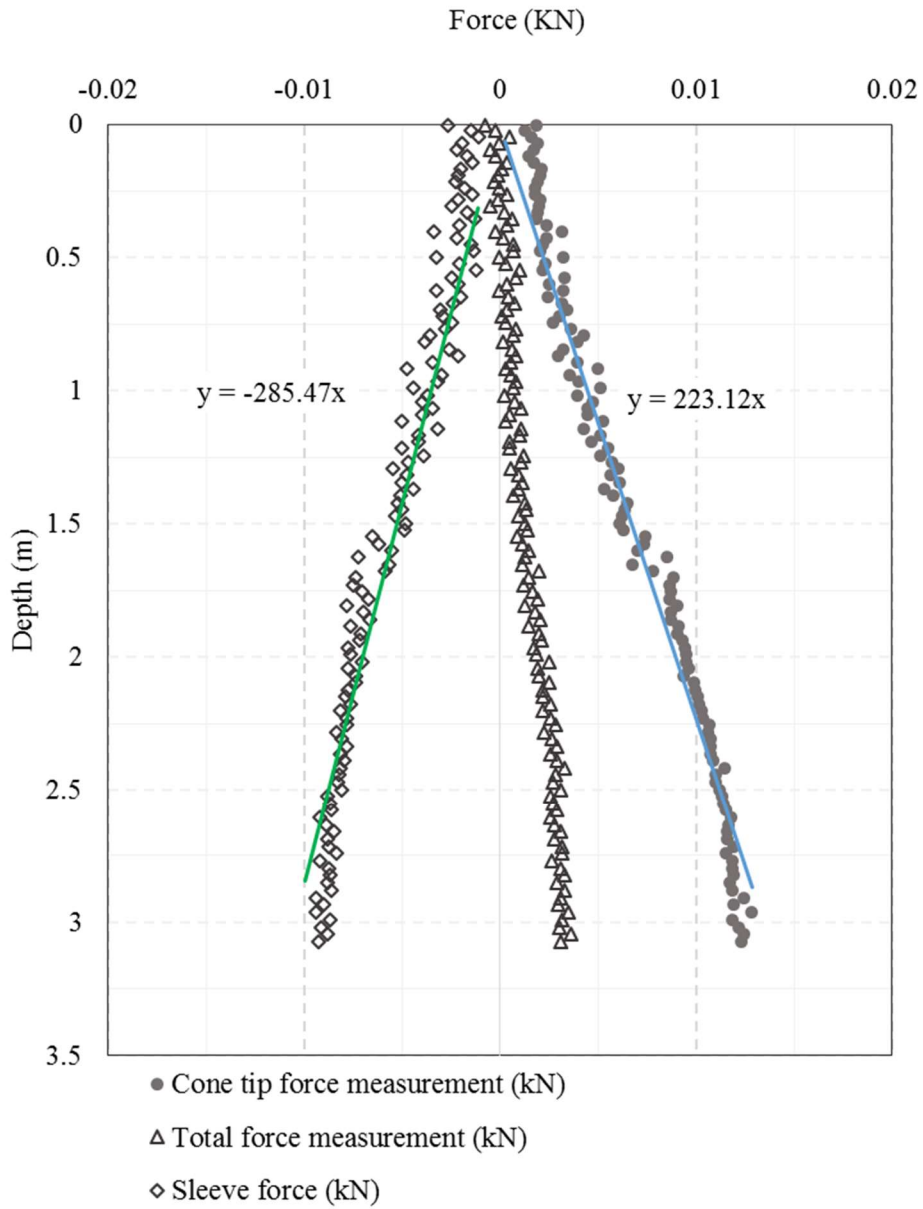
Figure 7-1 Measured tip force and total force and calculated sleeve force from penetration test in water

7.2.3 Hydrostatic water pressure profile

The water unit weight varies with the distance from the center of the centrifuge and can be calculated using Equation 7.5.

$$\gamma_{w\,(r)} = \rho_w \cdot g_{(r)} = \rho_w \frac{g_{(0)}}{r_0} r \qquad \text{Eq. 7.5}$$

In which r is the distance from the center of centrifuge arm, $g_{(0)}$ is the nominal g-level and r_0 is radius of the nominal g-level as shown in Figure 7.2. Then, the hydrostatic water pressure profile can be determined by integrating the water unit weight γ_w along the height.

$$u_{(r)} = \int_{r_w}^{r} \gamma_w dr = \int_{r_w}^{r} \rho_w \frac{g_{(0)}}{r_0} r dr = \frac{\rho_w g_{(0)}}{2r_0} (r^2 - r_w^2) \qquad \text{Eq. 7.6}$$

In which r_w is the distance between free water surface and center of centrifuge arm (Figure 7.2). The position of free water surface can also be determined from PPT readings before starting the penetration tests, given the position of sensor and the water pressure, u. Thus, using Eq. 7.7 gives the value of r_w as following:

$$r_w = \sqrt{r^2 - \frac{2r_0 u}{\rho_w g_{(0)}}} \qquad \text{Eq. 7.7}$$
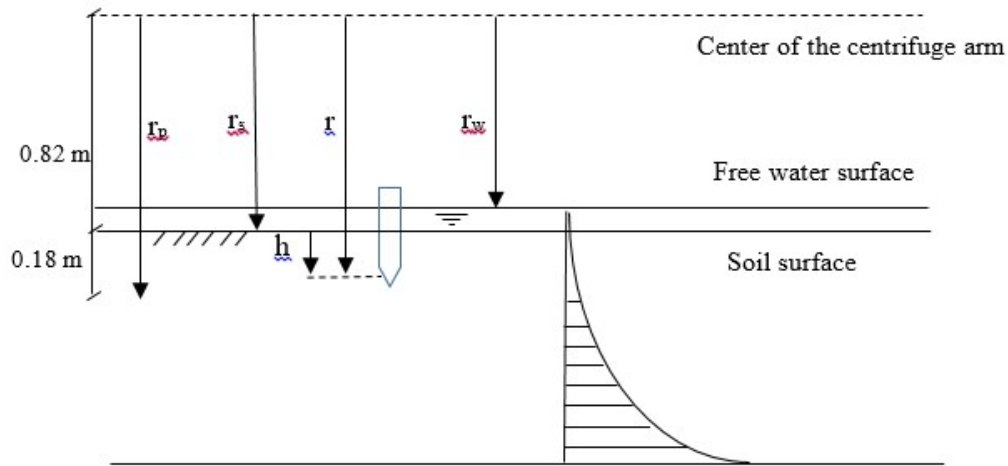
Figure 7-2 Free water surface and piezocone position in respect to the center of centrifuge arm

Having $g_{(0)}$ of 45 and r_0 of 1m in this study, Eq. 7.8 could be summarizes into:

$$u_{(r)} = \frac{1000*45*9.81}{2*1} (r^2 - 0.82^2) = 220.725r^2 - 148.415 \ (kPa) \qquad \text{Eq. 7.8}$$

7.3   Penetration Test Results

The results corresponding to penetration tests are presented in this section. Results consists of cone tip force and sleeve force, cone resistance (q_c) and sleeve friction (f_s) profiles for all tests and pore water pressure (u) profile for saturated and unsaturated tests.

7.3.1   Penetration results of Ottawa sand I (S1)

7.3.1.1   Dry test 1 (S1D1)

Figure 7.3 show the force measurements (tip force and total force) versus time profile of the dry test. Data were recorded for a while before and after the test. The actual penetration took place in 18 seconds during the time period of 35 second and 53 seconds. As it can be seen, there is an increase in force measurements as the test was started and then a decrease after the penetration was completed and during spinning down the centrifuge. The data corresponding to the duration of penetration test (between the time 35 and 53s) were picked and analyzed to find the cone tip resistance and sleeve friction. Figure 7.4 and 7.5 show the tip resistance and sleeve friction profiles respectively. The profiles were presented for prototype depth. The prototype depth was calculated considering the penetration rate and the g-level at each depth as explained in section 6.2.1.

The tip resistance increases linearly in depth as it was expected and reach 1 MPa at maximum penetration depth of 3 m. Having the relative density of the soil, the void ratio can be calculated using equation 7.9. The corresponding soil density for this void ratio would be 1460 kg/m^3. The vertical effective stress of such a soil at depth of 3m is about 0.05 MPa. Using the chart developed after Jamiolkowski et al. (1985) presented in figure 7.6, the cone resistance can be estimated between 0.9 Mpa and 2.9 Mpa for high compressibility and low compressibility quartz sand respectively. It proves that the measured cone resistance is in an acceptable range.

$$Dr = \frac{e_{max} - e}{e_{max} - e_{min}} \rightarrow 0.27 = \frac{0.805 - e}{0.805 - 0.486} \rightarrow e = 0.72 \qquad Eq.\,7.9$$

As it can be seen in Figure 7.5, the sleeve friction is about 0.5% of the tip resistance which is usual

for coarse grain soils.
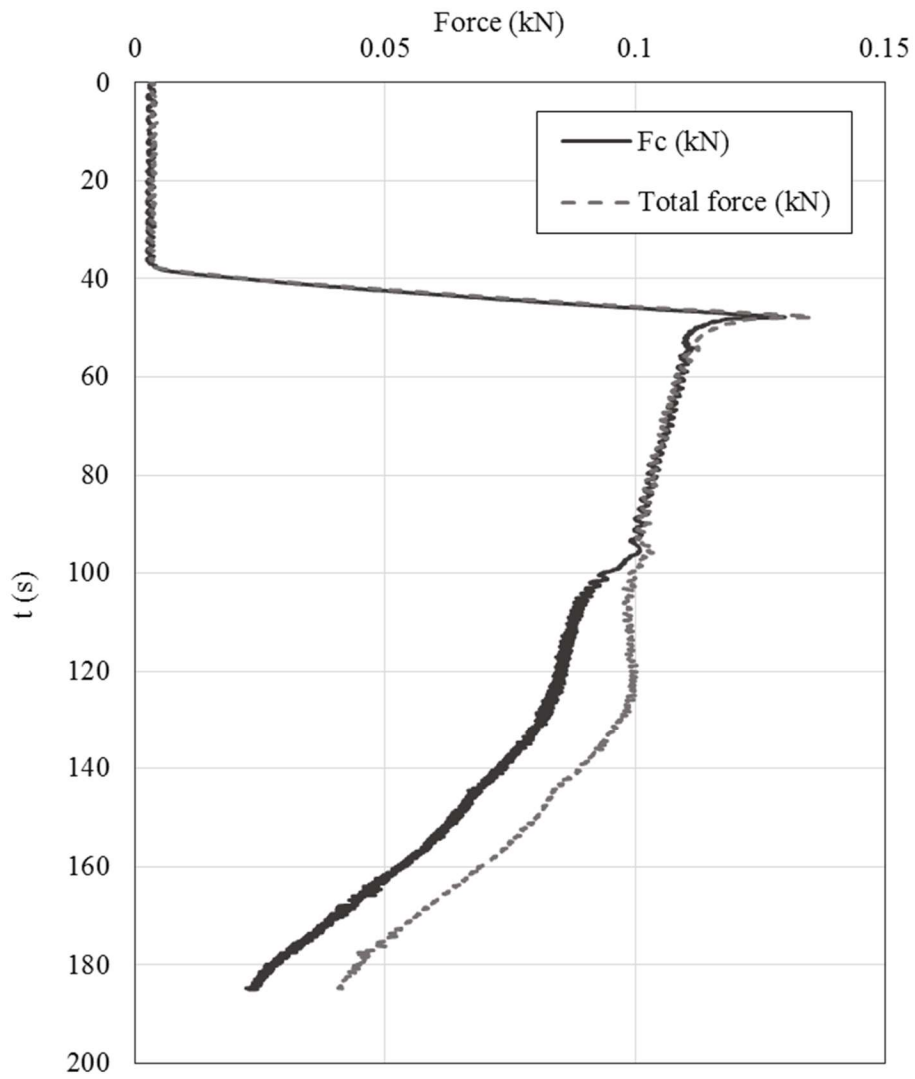
Figure 7-3 Tip force and total force measurements of penetration test on sample S1D1

Figure 7-4Tip resistance (qc) profile of penetration test on sample S1D1
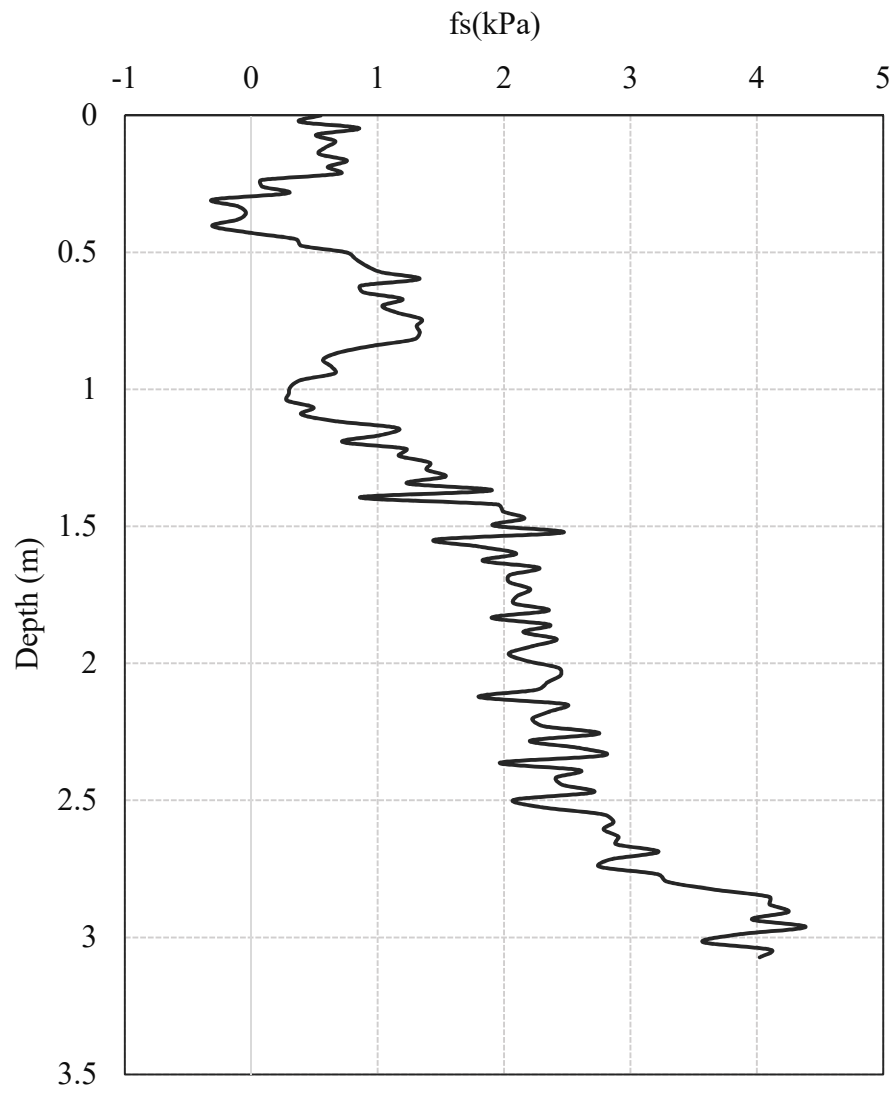
Figure 7-5 Sleeve friction (fs) profile of penetration test on sample S1D1
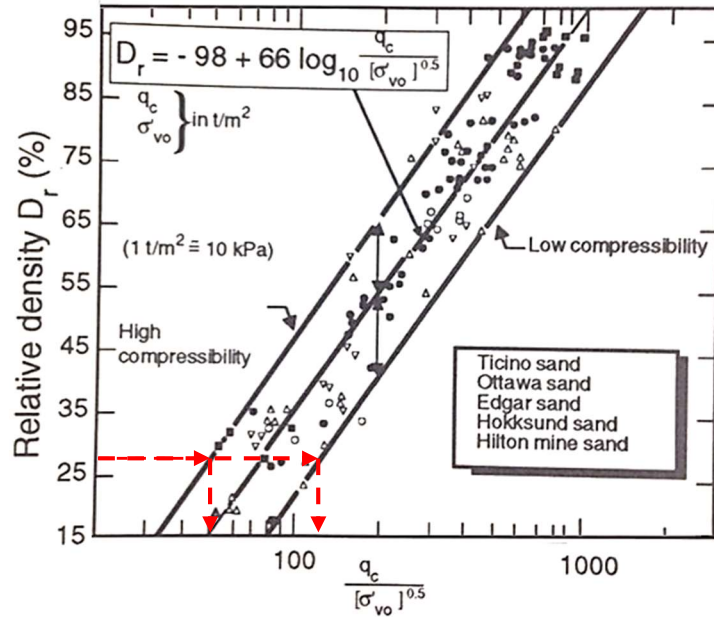
Figure 77-6 Cone resistance estimation based on relative density and vertical effective stress
(after Jamiolkowski et al., 1985)

7.3.1.2 Dry test 2 (S1D2)

Figure 7.7 to 7.9 show the results of second dry test. As it is shown in Figure 7.7, the recorded force measurements are similar to the first test ones.

The tip resistance and sleeve friction profiles are shown in Figure 7.8 and 7.9. The measured tip resistance and sleeve friction profiles are similar to test 1. For better comparison, the results of two tests were shown in one plot. Figure 7.10 presents tip resistance profiles. Considering a relative density of 27%, the empirical equation by Jamiolkowski et. al.(1985), explained in the previous section, was added to the graph as well. As it can be seen, the measured tip resistances are about 10 percent different and results of both tests are in the range of predicted cone resistance by the empirical equation (closer to the high compressibility side) for depths more than 1 m. This

difference could be because of sample preparation procedure which can results in samples with

not exactly the same relative densities.

Figure 7.11 presents sleeve friction profiles. As it is shown, the friction sleeve values of

both tests are pretty close and the difference observed in tip resistance profiles does not exist here.

Based on the results of dry tests, it could be concluded that the samples demonstrate a good

repeatability which confirm the suitability of the specimen formation and adapted testing

procedure.
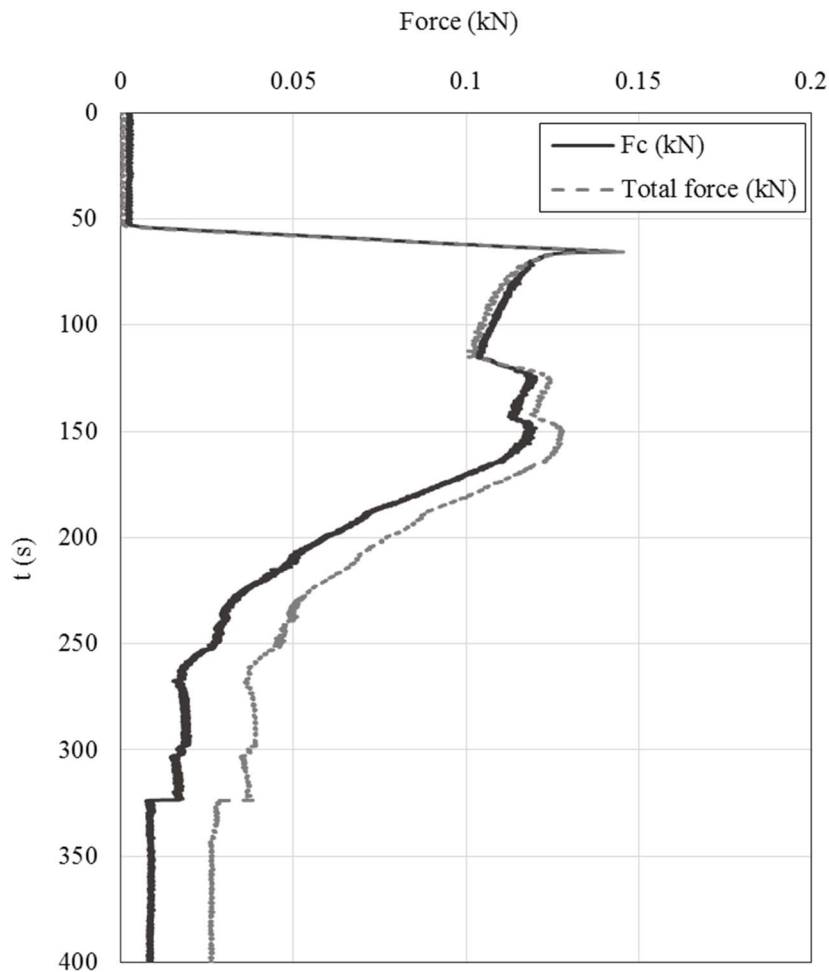
Figure 7-7 Tip force and total force measurements of penetration test on sample S1D2
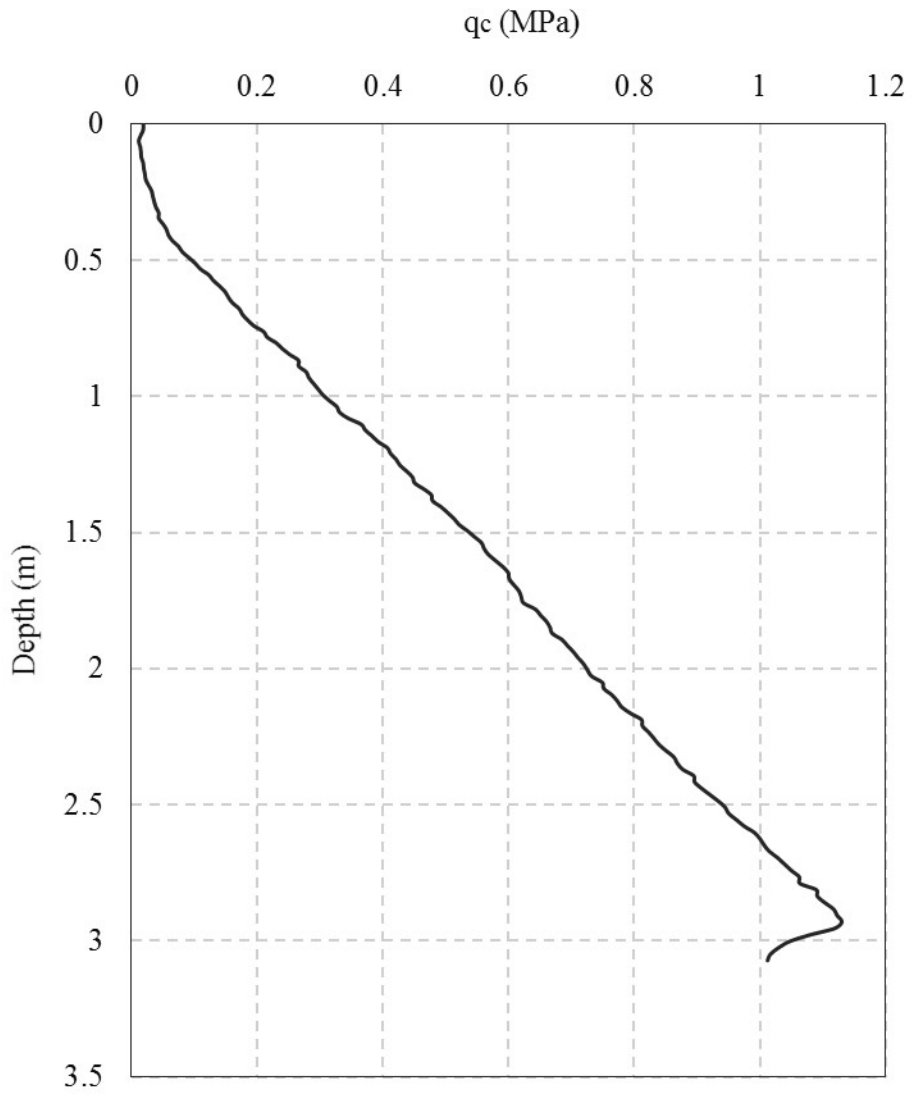
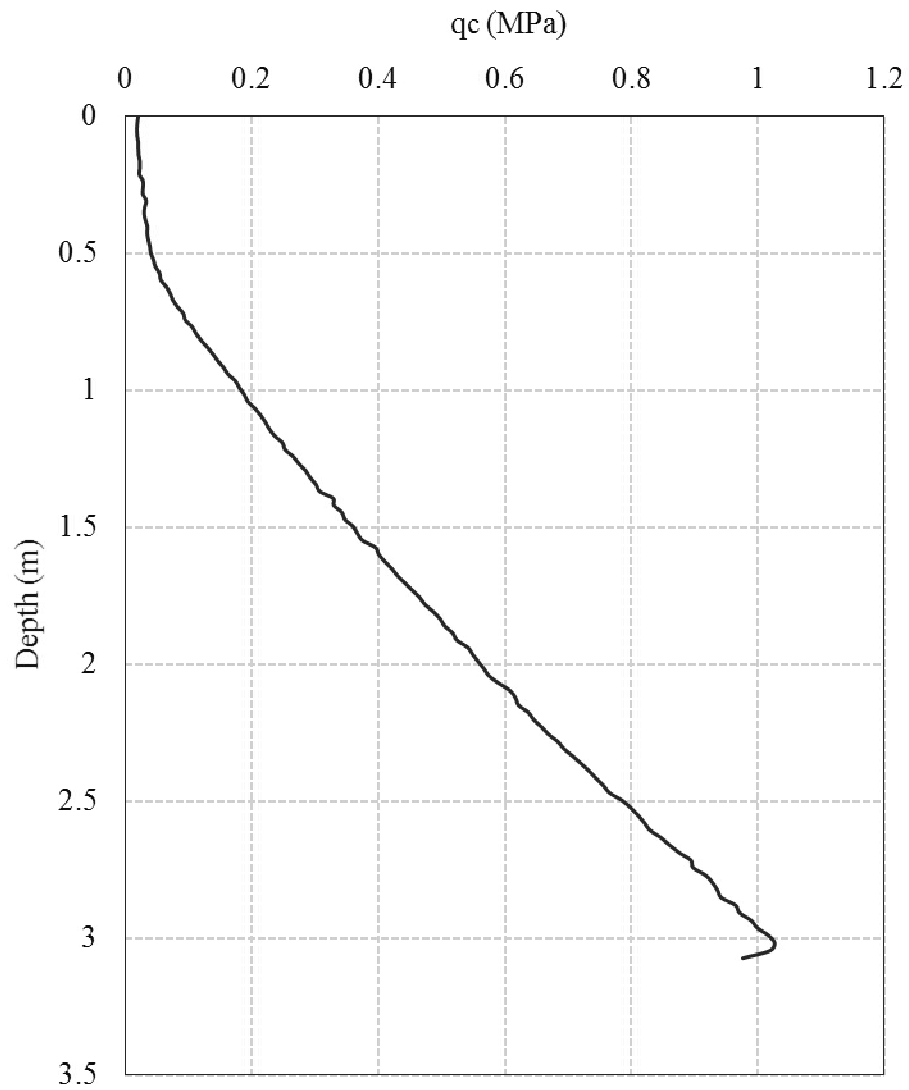Figure 7-8 Tip resistance (qc) profile of penetration test on sample S1D2
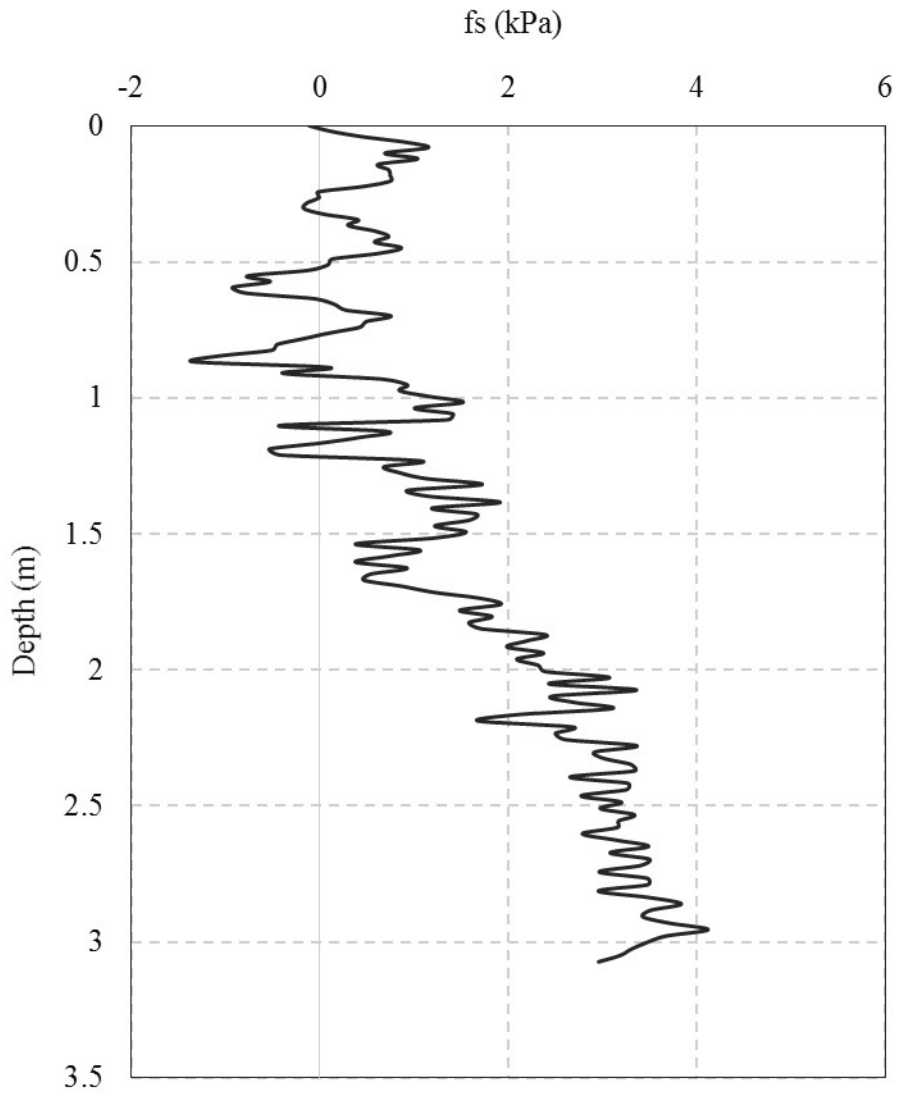
Figure 7-9 Sleeve friction (fs) profile of penetration test on sample S1D2
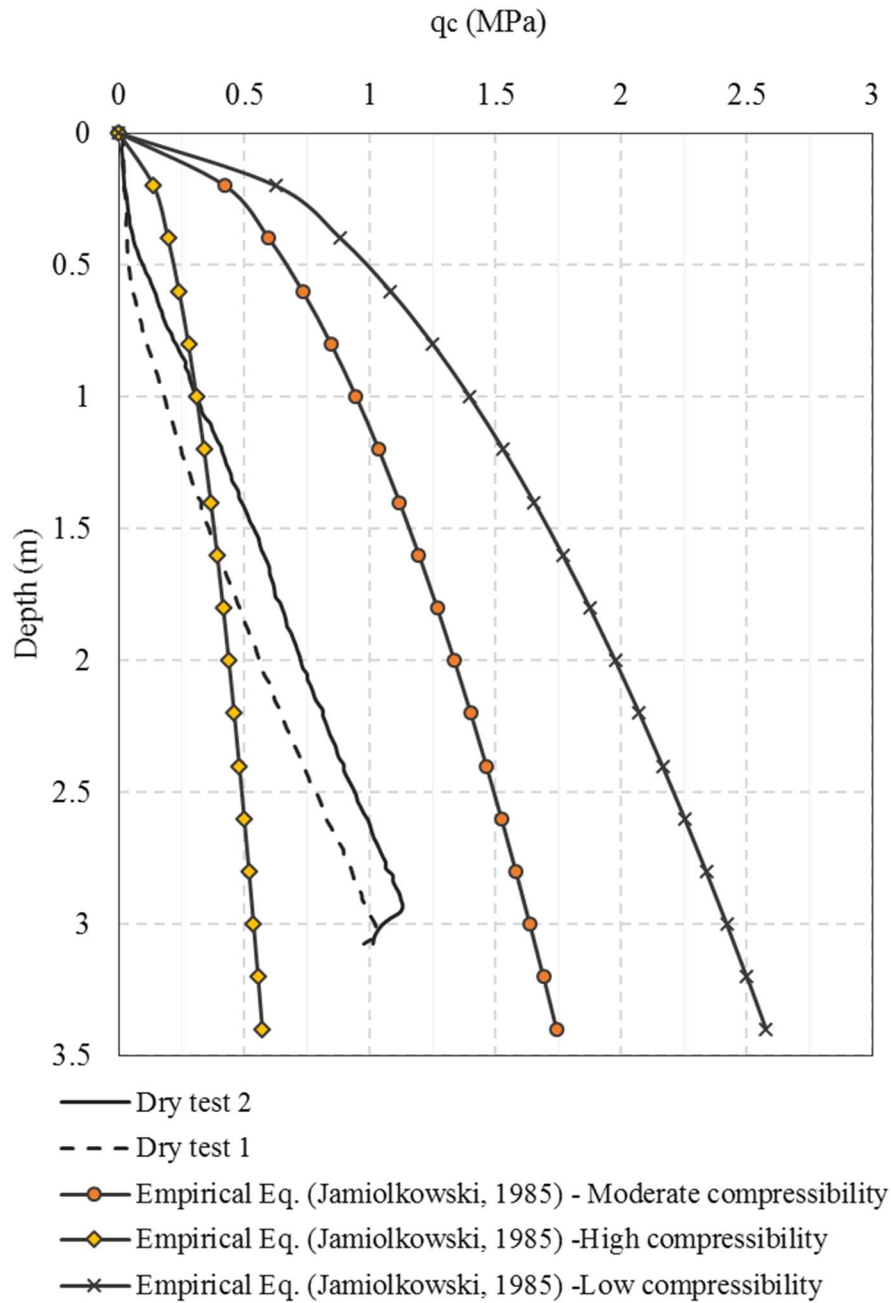
Figure 7-10 Comparison of tip resistance (qc) profile of penetration test on dry samples (S1D1 and S1D2)
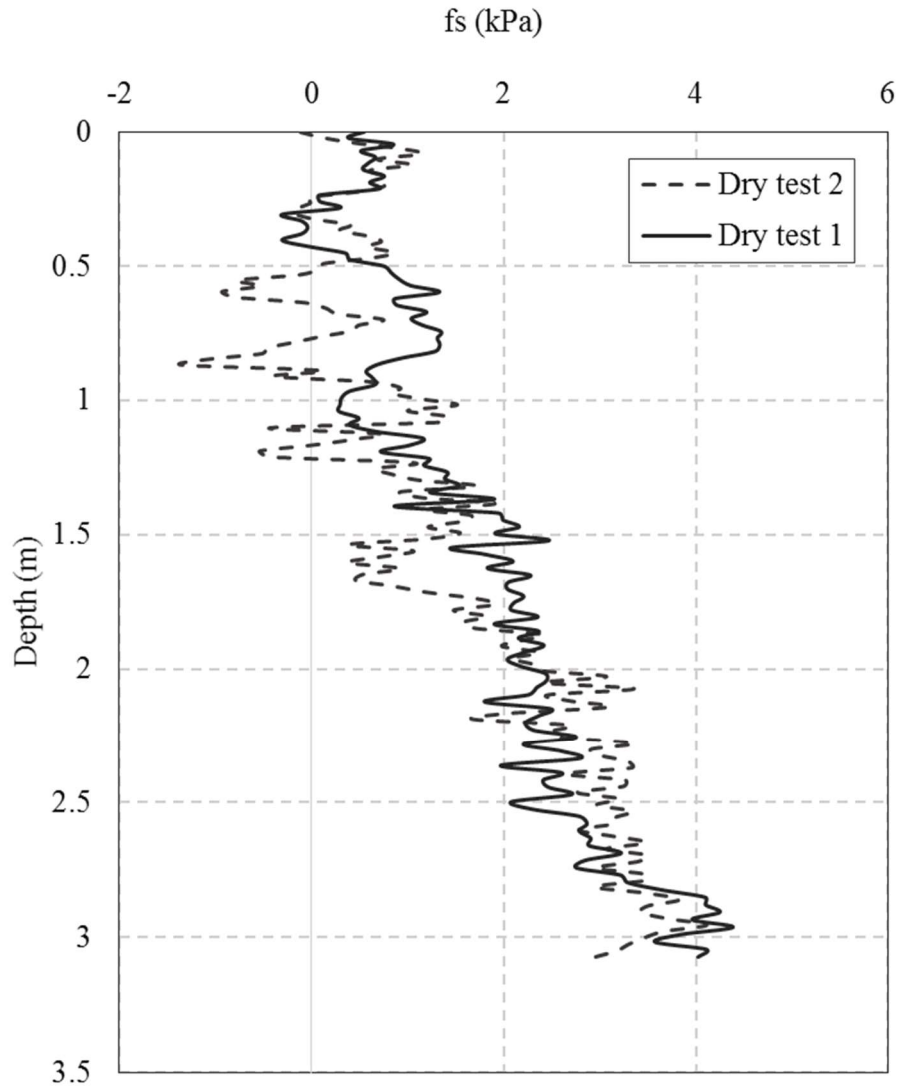
Figure 7-11 Comparison of sleeve friction (fs) profile of penetration test on dry samples (S1D1 and S1D2)

7.3.1.3 Saturated test (S1S1)

In the following, results of saturated test are presented through Figures 7.12 to 7.19. This test was performed in three intervals. The drops in the q_c profiles are related to the end of each interval. The cone was kept saturated by putting a small plastic cylinder with a plastic sheet at the bottom on the soil surface and filling it with water. Thus, cone was in the water during the centrifuge spinning. As the test starts, it hits the plastic sheet and tears I, so, it doesn't make any obstacle for penetration.

Figure 7.12 shows the correction of cone tip force explained in section 6.1.2. As it is shown, the correction is about 13% of the measured cone tip force.

The tip resistance profile is presented in figure 7.13 while a comparison of this profile with dry ones is presented in Figure 7.14. Here, the tip resistance increases linearly similar to the dry test. Up to the depth of 1.5 m, the q_c values of saturated and dry test 1 are close to each other and lower than dry test 2 and in depths more than 1.5 m, the q_c values of saturated test is lower than both dry tests. This reduction was expected as the effective stress and thus the soil strength is lower in saturated condition. In addition, it is mentioned in literature that it can be attributed to the development of pore pressure during testing which reduces the effective stress of the soil and thus the soil strength (Shaqour F.M., 2007).

The sleeve friction profile is presented in Figure 7.15 and comparison of this profile with dry ones is presented in Figure 7.16. There is a linear increase in sleeve friction values with depth similar to dry tests. However, unlike the tip resistance, the sleeve friction values in saturated test are about 50% higher than dry ones. This result is unexpected and seems to be too much change and more data is needed for better conclusion.

Figure 7.17 shows the pore pressure measurements for the three penetration intervals. They were shown for a while before and after each interval for better explanation. The negative values are generated because of the pressure due to the distance between cone and transducer as explained in section 4.5.1. The pressure is constant before each penetration interval and then it decreases linearly during the penetration and again it becomes constant as the penetration is completed and no excess pore pressure is observed. However, the results should be corrected, as explained in section 4.5.1, for better discussion. Figure 7.18 shows the correction procedure while Figure 7.19 presents the corrected pore pressure in comparison with hydrostatic pressure. Up to the depth of 1 m, the measured pore pressure doesn't follow the same trend as hydrostatic pressure and predicted values are less than the hydrostatic pressure but in depths more than 1 m, the measurements have the same slope as hydrostatic pressure which gives a predicted pressure 70% of hydrostatic pressure at depth 3 m. There is a possibility that cone became de-saturated during the centrifuge spinning and then under hydrostatic pressure, it gets saturated again.

Figure 7-12 Cone weight correction of cone tip resistance profile of S1S
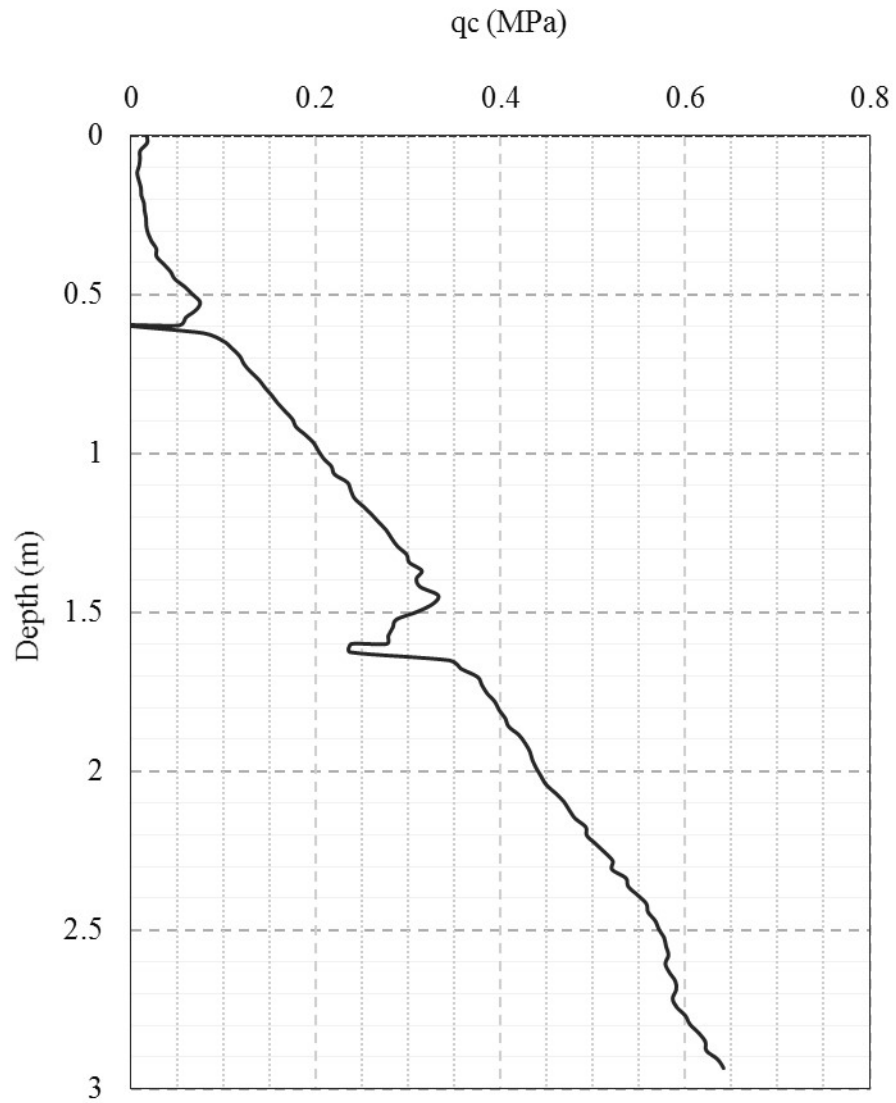
Figure 7-13 Tip resistance (qc) profile of penetration test of S1S

Figure 77-14 Comparison of tip resistance (qc) profile of penetration test of S1D1, S1D2 and S1S
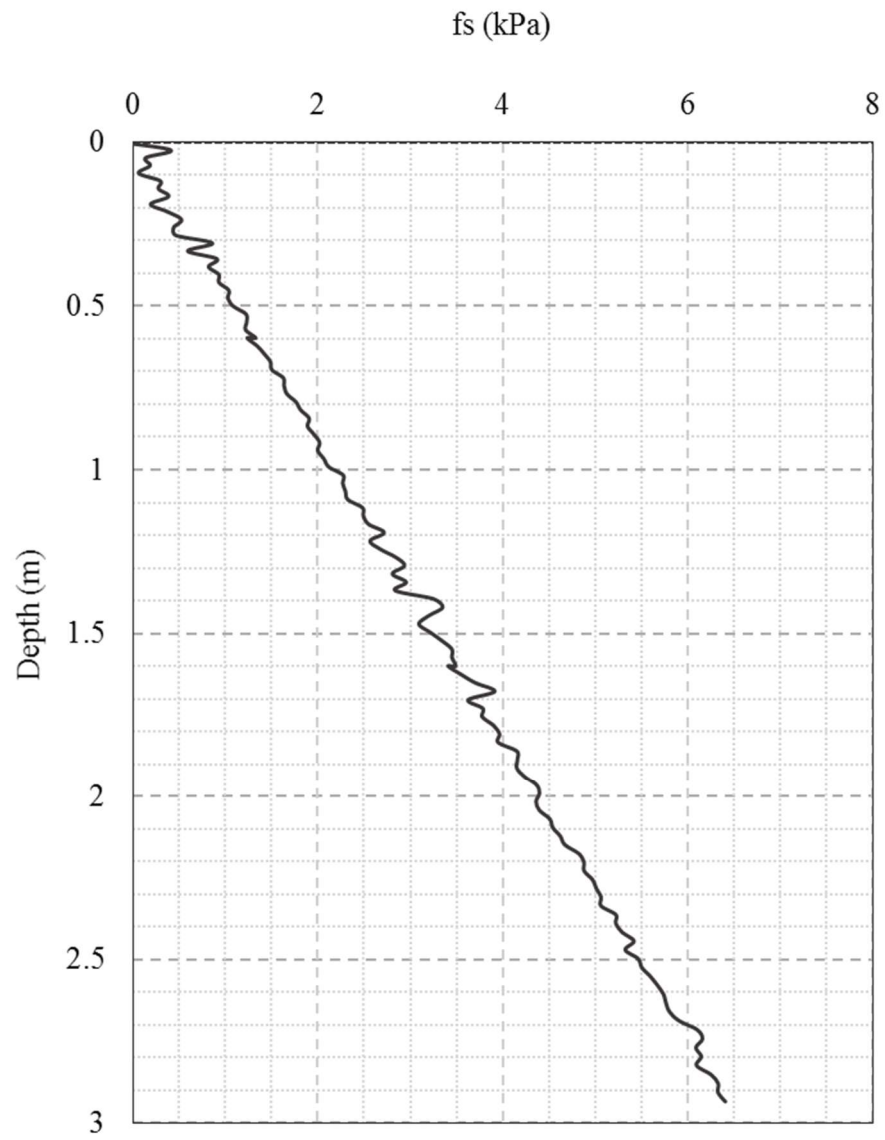
Figure 7-15 Sleeve friction (fs) profile of penetration test of S1S

Figure 7-16 Comparison of sleeve friction (fs) profile of penetration test of S1D1, S1D2 and S1S
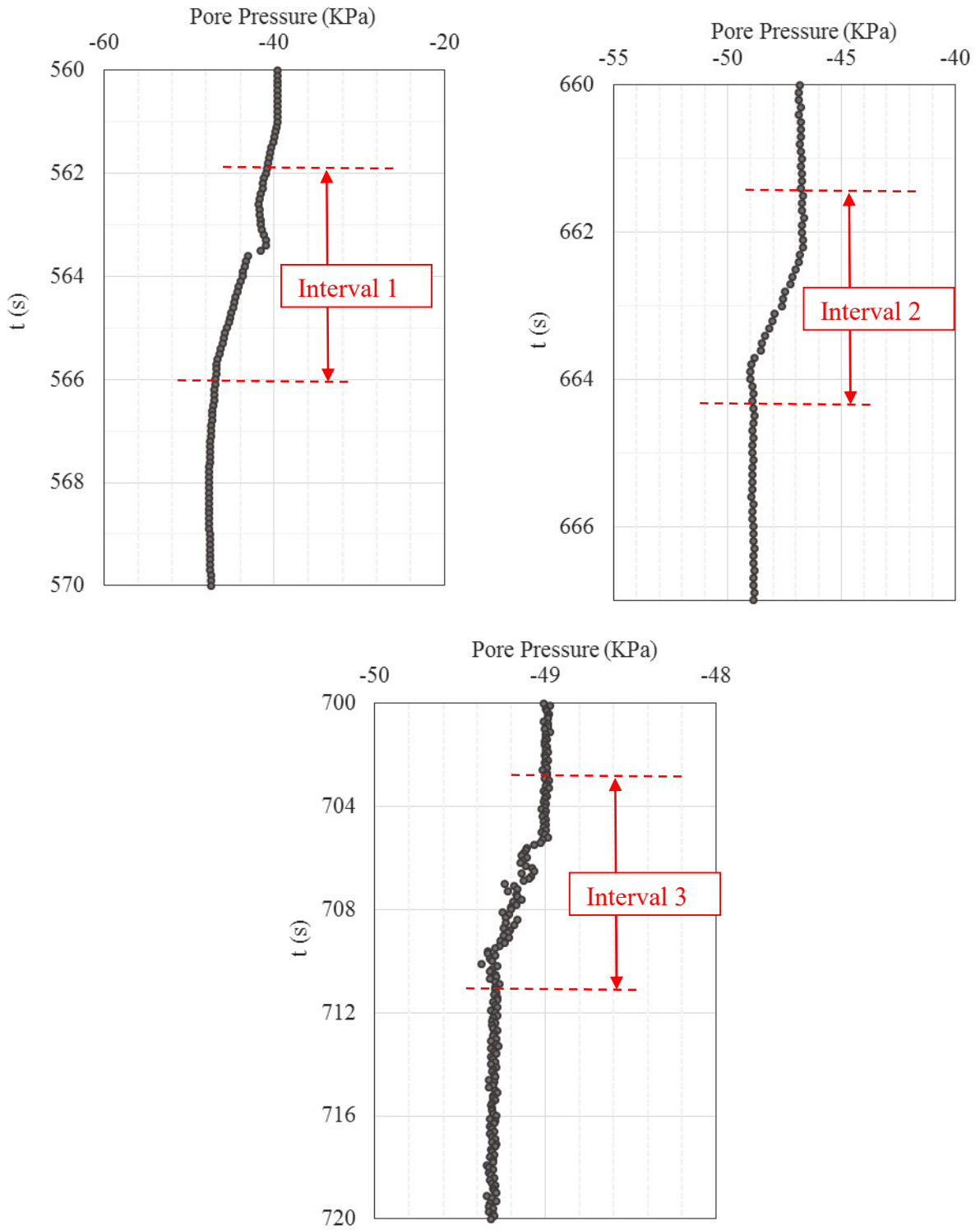
Figure 7-17 Pore pressure measurements for three penetration intervals of S1S
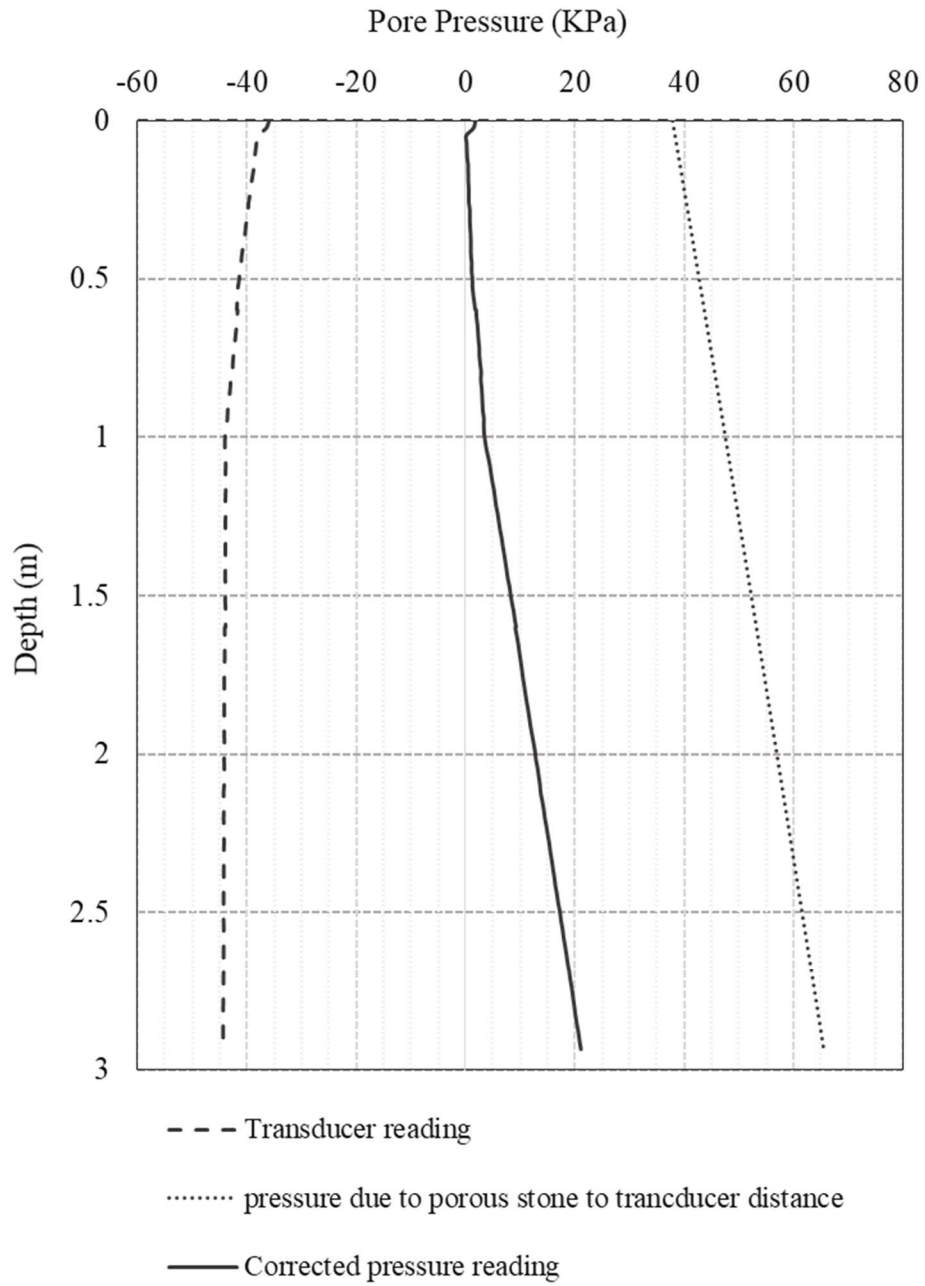
Figure 7-18 Pore pressure correction of S1S

Figure 7-19 Corrected pore pressure of S1S in comparison with hydrostatic pressure

7.3.1.4 Penetration results in unsaturated soil 1 (S1U)

In the following, the results of penetration test in unsaturated soil are presented through Figures 7.20 to 7.23. This test was done in three steps but unfortunately, the pore pressure measurements were not recorded due to hardware problems.

Figure 7.20 shows the cone tip resistance (q_c) profile while Figure 7.21 shows this profile in comparison with dry and saturated tests. Averaging the results of dry test 1 and 2, as it can be

seen, the q_c values of unsaturated condition are higher than dry and saturated condition. This is consistent with the literature in which higher strength is reported for soil in unsaturated condition (Pournaghiazar 2013).

Figure 7.22 shows the sleeve friction (f_s) profile while Figure 7.23 shows this profile in comparison with dry and saturated tests. As it is shown, the sleeve friction in unsaturated condition is much higher than dry and saturated condition (about 10 times). As explained for saturated test, this much of increase seems to be too much and there is a possibility that the load cell calibration is changed.
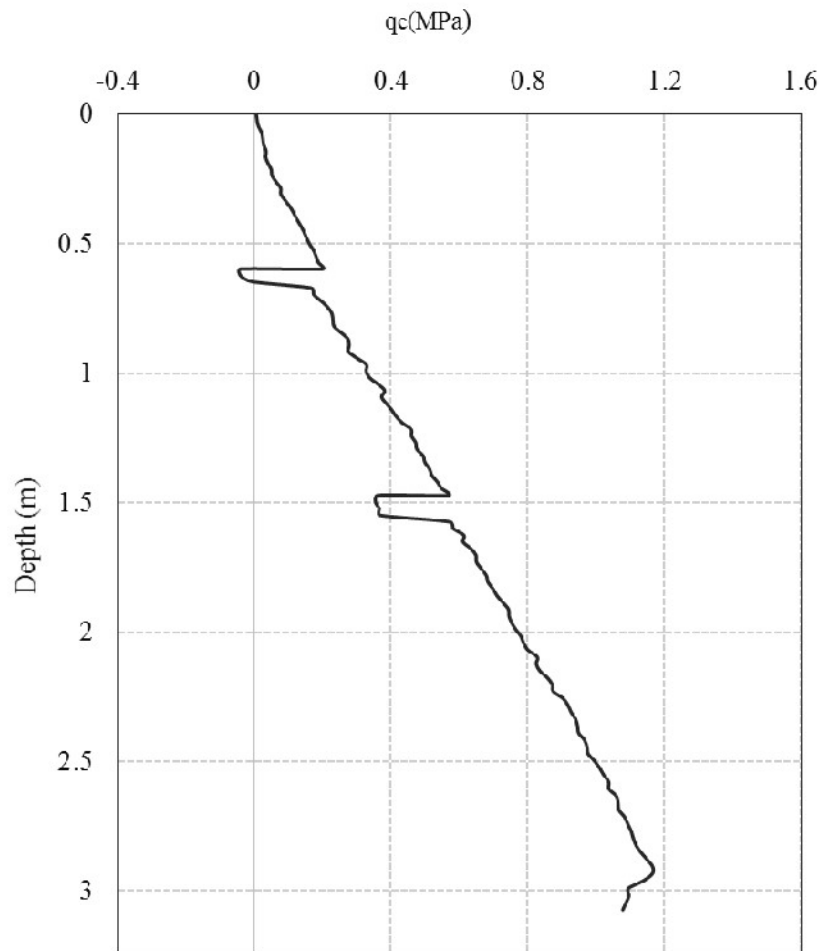
Figure 7-20 Tip resistance (qc) profile of penetration test of S1U
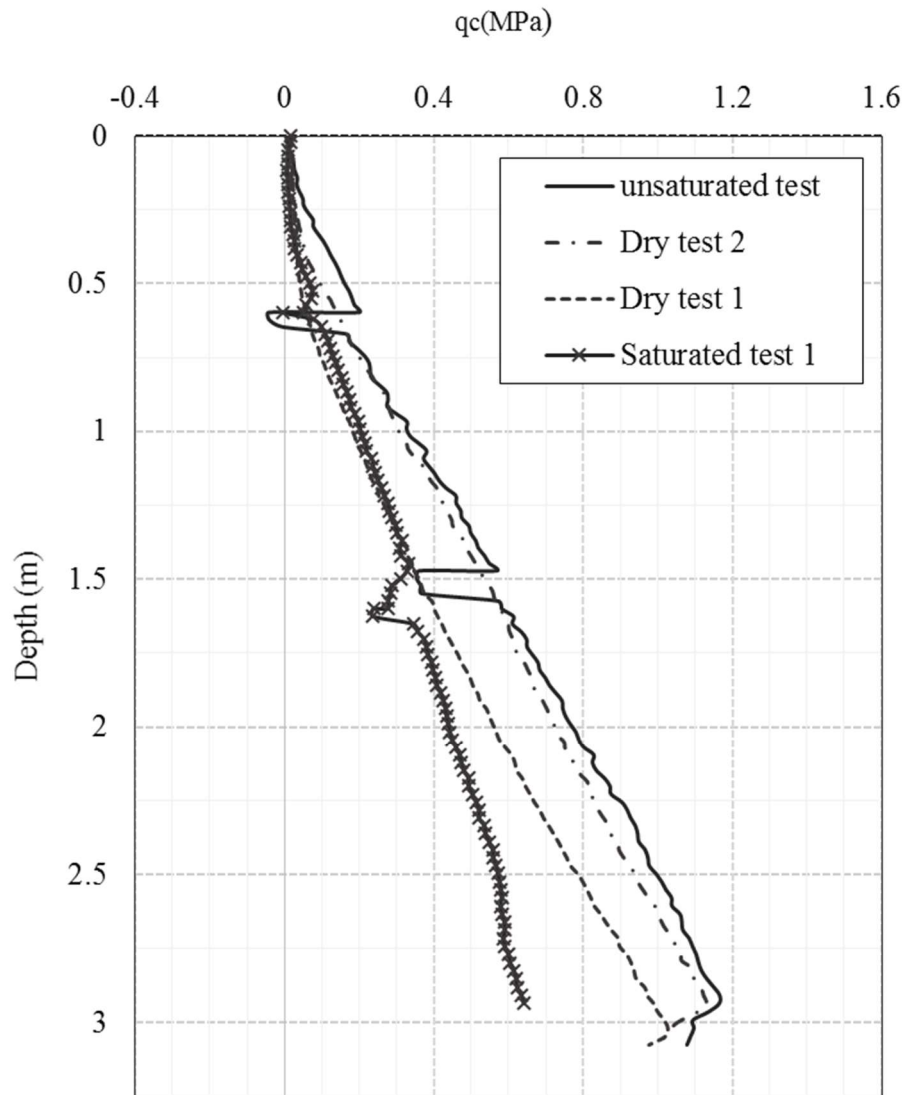
Figure 7-21 Comparison of tip resistance (qc) profile of penetration test on dry, saturated and unsaturated samples (S1D1, S1D2, S1S, S1U)
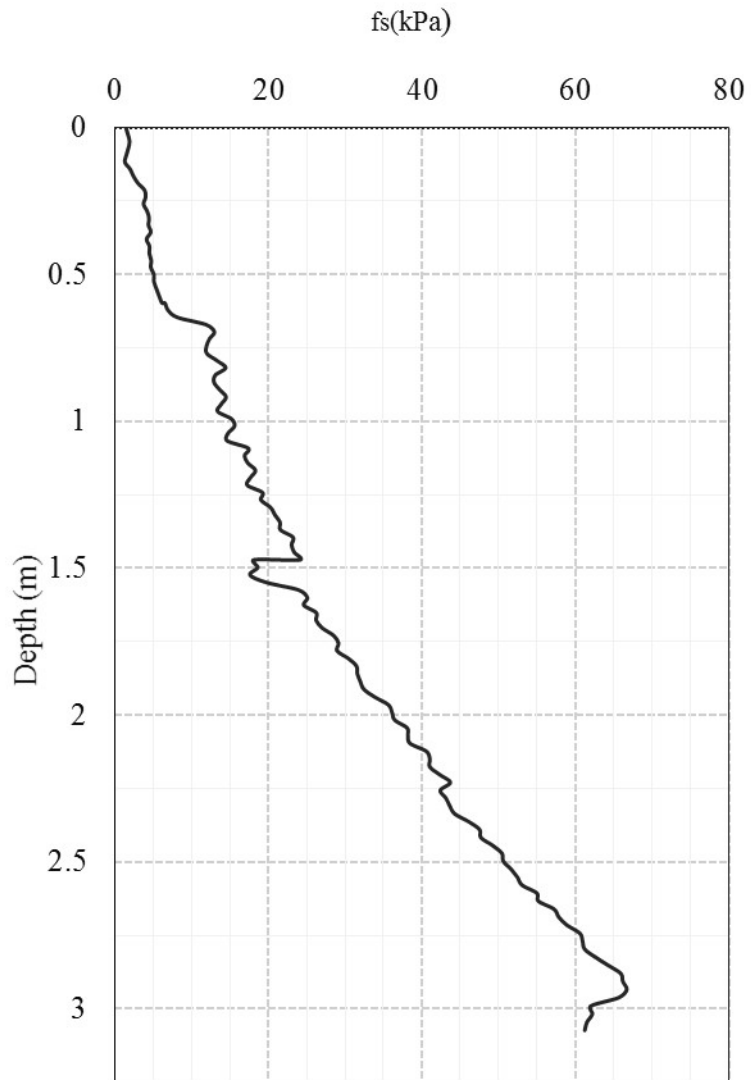
Figure 7-22 Sleeve friction (fs) profile of penetration test of S1U
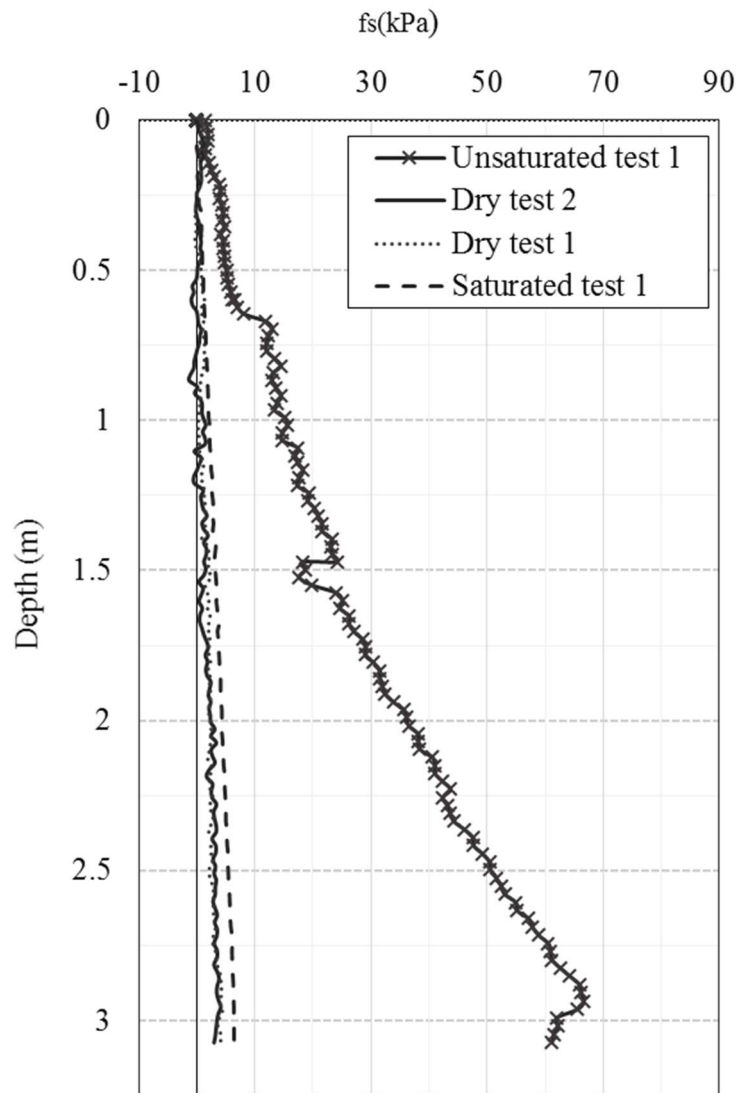
Figure 7-23 Comparison of sleeve friction (fs) profile of penetration test on dry, saturated and unsaturated samples (S1D1, S1D2, S1S, S1U)

7.3.2   Penetration results of Ottawa sand II (S2)

7.3.2.1   Saturated test (S2S)

In the following, the results of penetration test in saturated sample 2 are presented through Figure 7.24 to 7.29. This test was done in three intervals. Three dielectric sensors and three PPTs

were used in different layer based on instrument layout shown in Figure 6.5. The cone porous stone was sealed using vacuum grease as explained in section 5.5.1.

Figure 7.24 shows the correction of cone tip force explained in section 7.1.2. Similar to saturated test 1, the correction is about 10% to 15% of the measured force.

Figure 7.25 shows the cone tip resistance (q_c) profile while Figure 7.26 shows the friction sleeve (f_s) profile. As it can be seen, the soil has much more sleeve friction (about 4 times more than soil 1). Although soil 2 has more fine content which provides cohesion between the cone and soil; however, this difference is seems too much and as mentioned before, there is a possibility of changing the load cell calibration.

Figure 7.27 shows the pore pressure measurements for the three penetration intervals. Similar to saturated test 1, they were shown for a while before and after each interval for better explanation. As explained before, the negative values are generated because of the pressure due to cone to transducer distance. In the first interval, the pressure is constant before the penetration and then it decreases linearly during the penetration and again it becomes constant as the penetration is completed and no extra pore pressure is observed. However, in the next two intervals, there is pore pressure. In the second one, the extra pore pressure is about 2 kPa and for the third one, it is about 6 kPa. This extra pore pressure takes a while to be dissipated. It is about 15 seconds for second interval and 80 seconds for third interval. The results are corrected for better discussion. Figure 7.28 shows the correction procedure while Figure 7.29 magnifies the corrected pore pressure for each interval and compares it with hydrostatic pressure. It should be mentioned that these graphs are shown versus time instead of depth to include the dissipation time while the penetration duration in these graphs is marked.
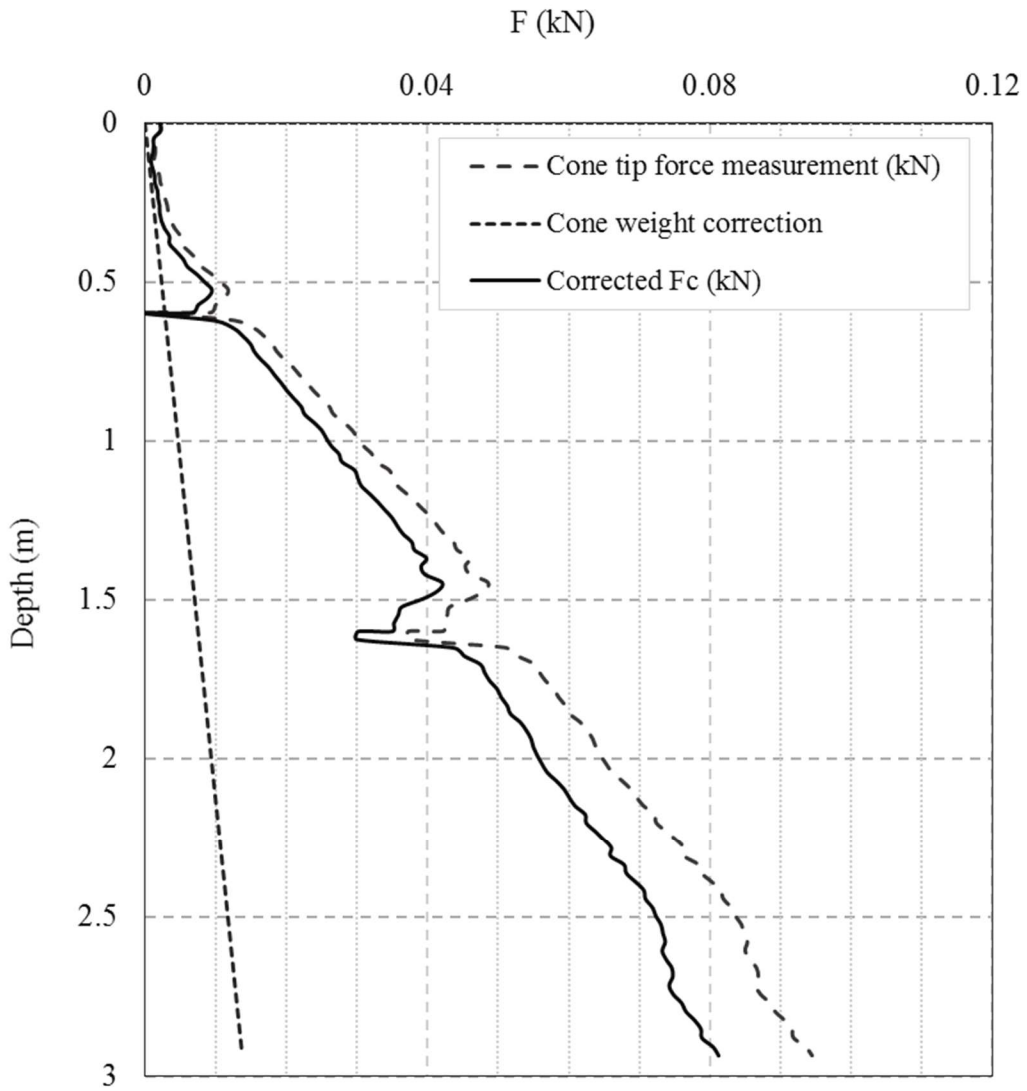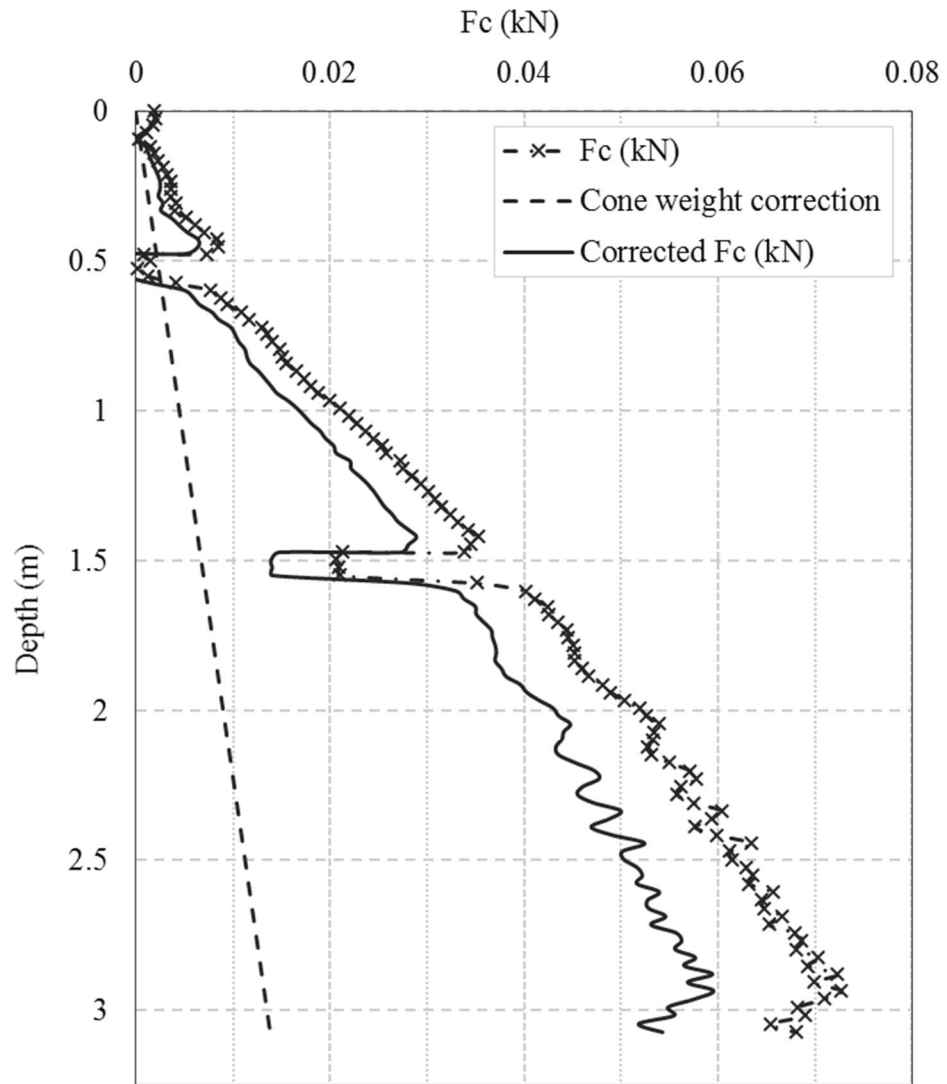
Figure 7-24 Cone weight correction of cone tip resistance profile of S2S
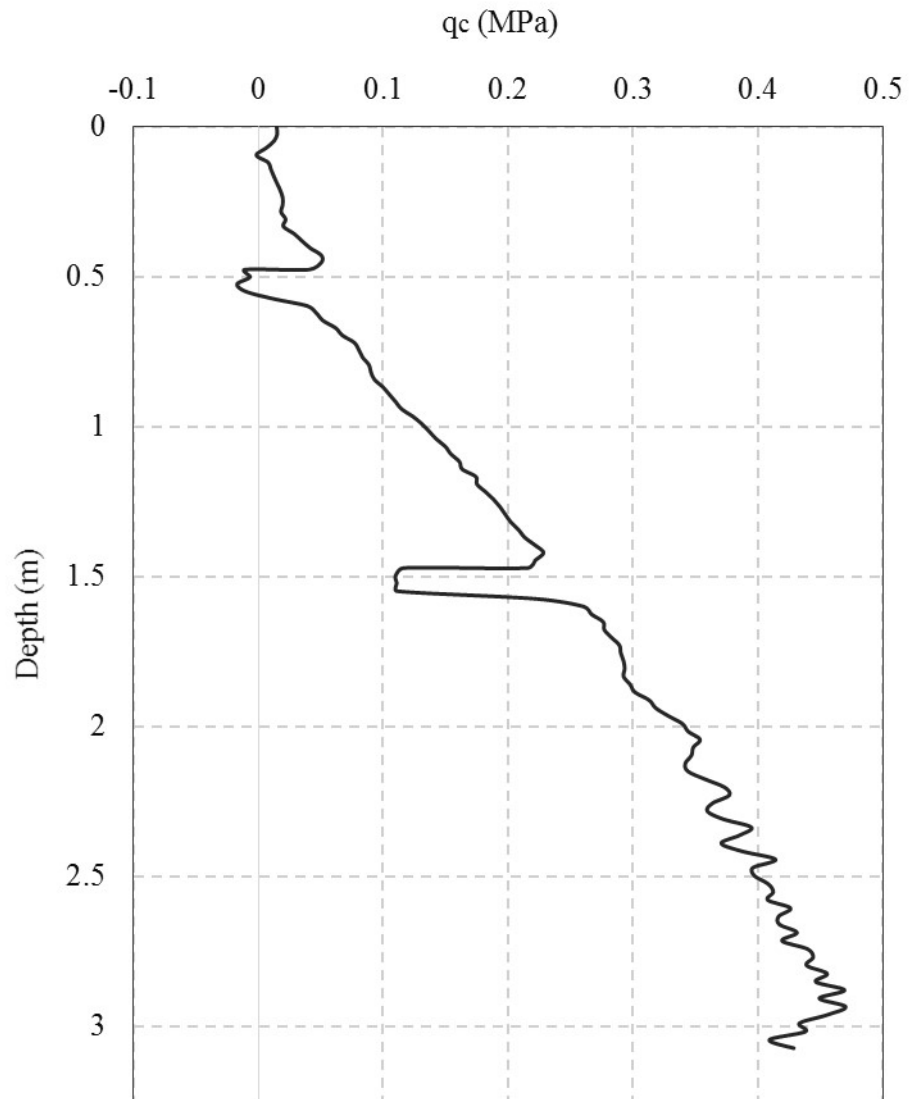
Figure 7-25 Tip resistance (qc) profile of penetration test of S2S
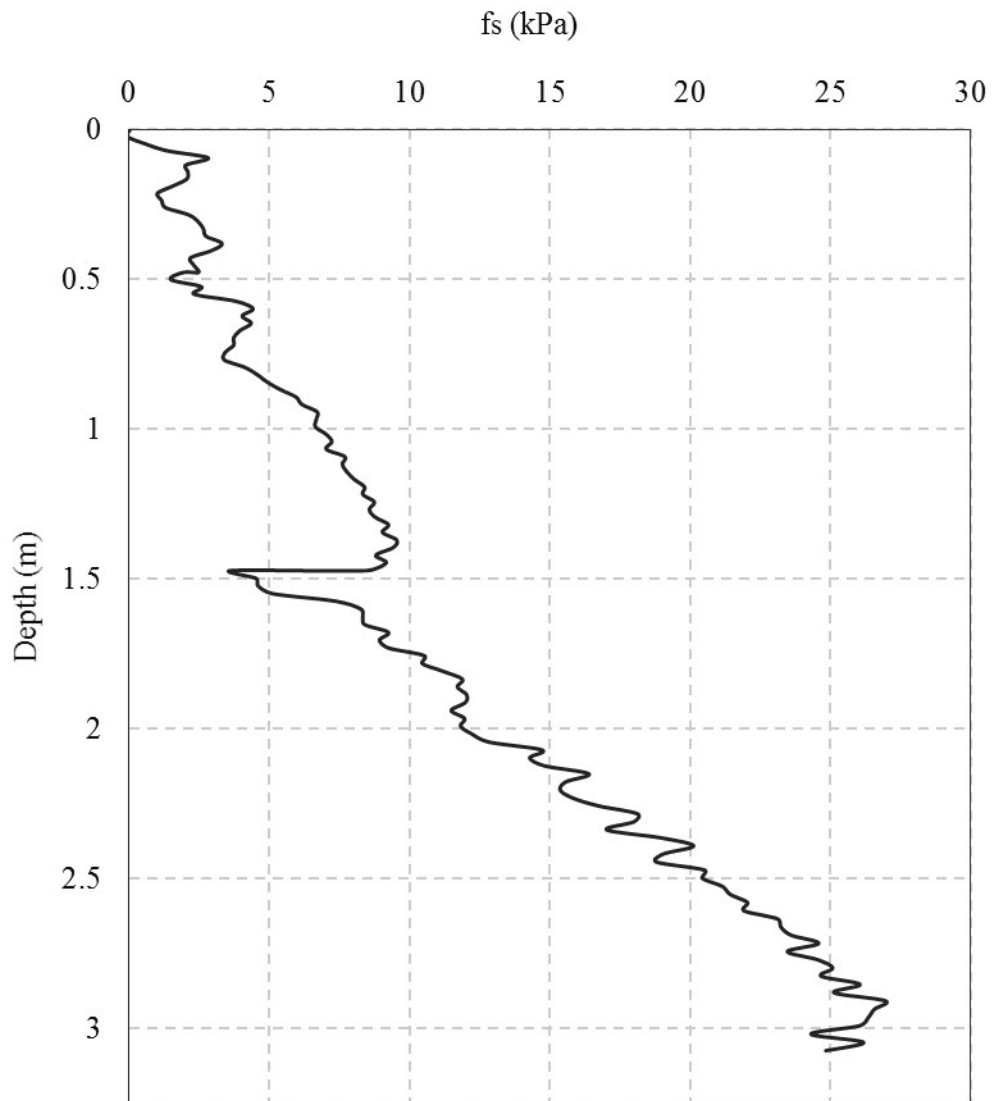
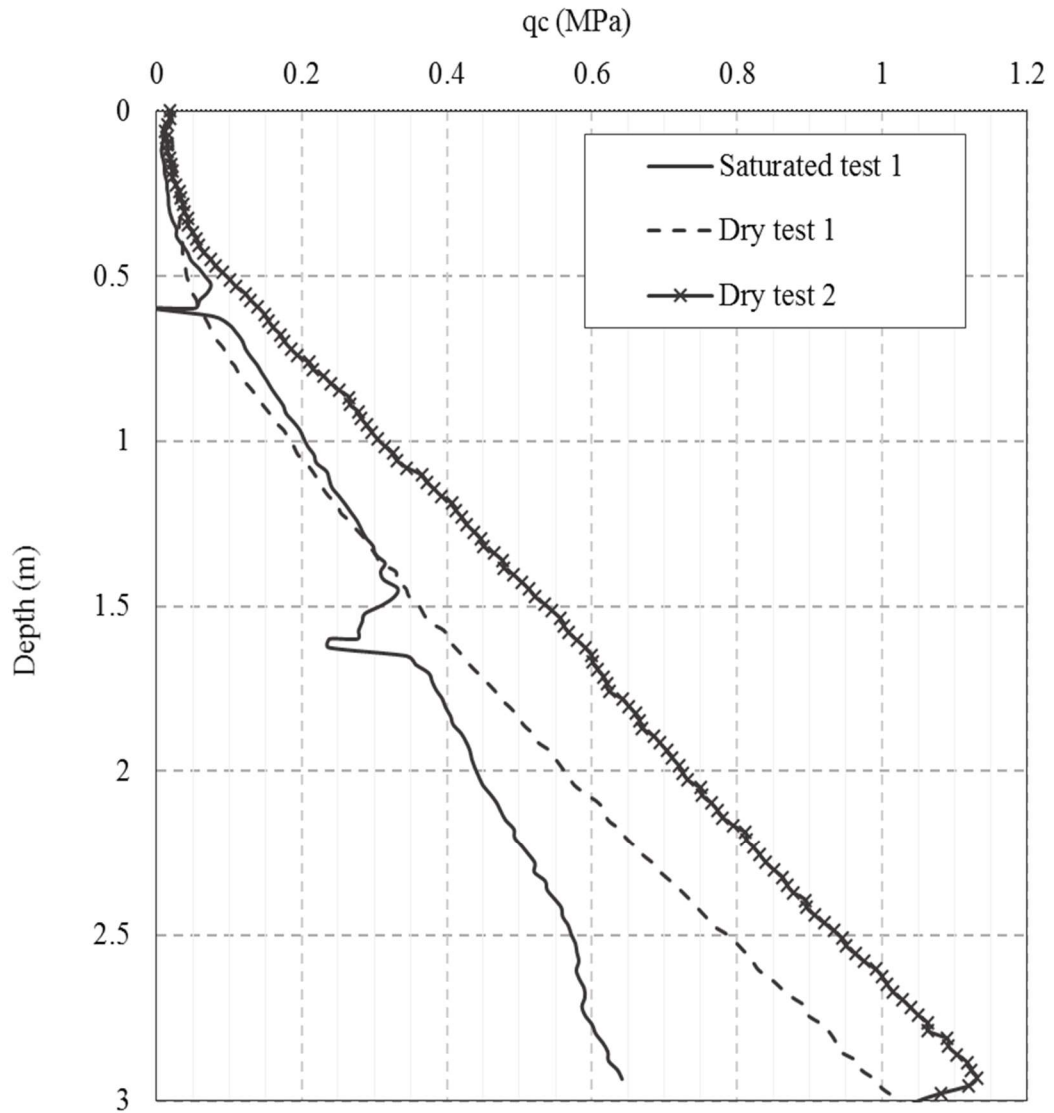Figure 7-26 Sleeve friction (fs) profile of penetration test of S2S
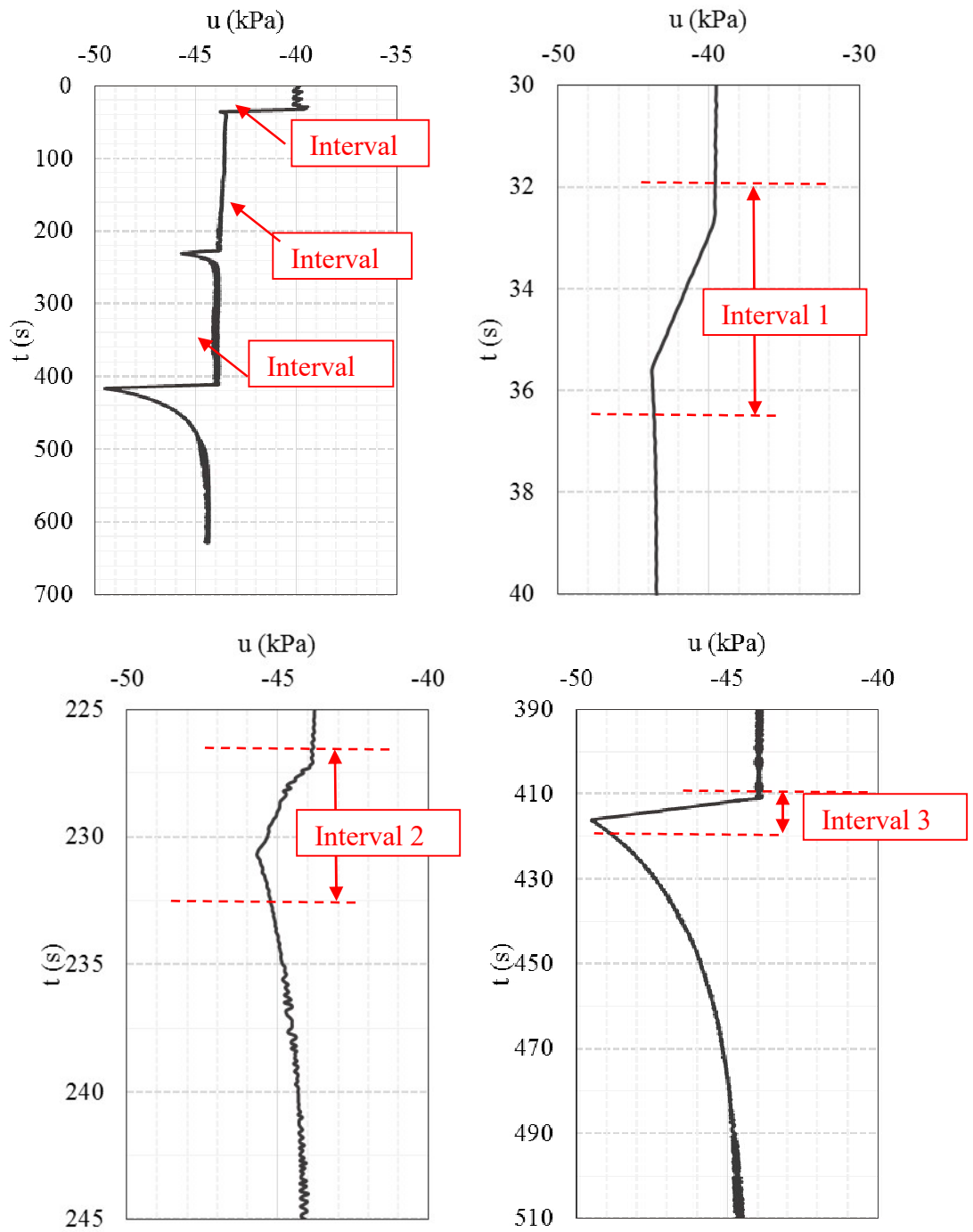
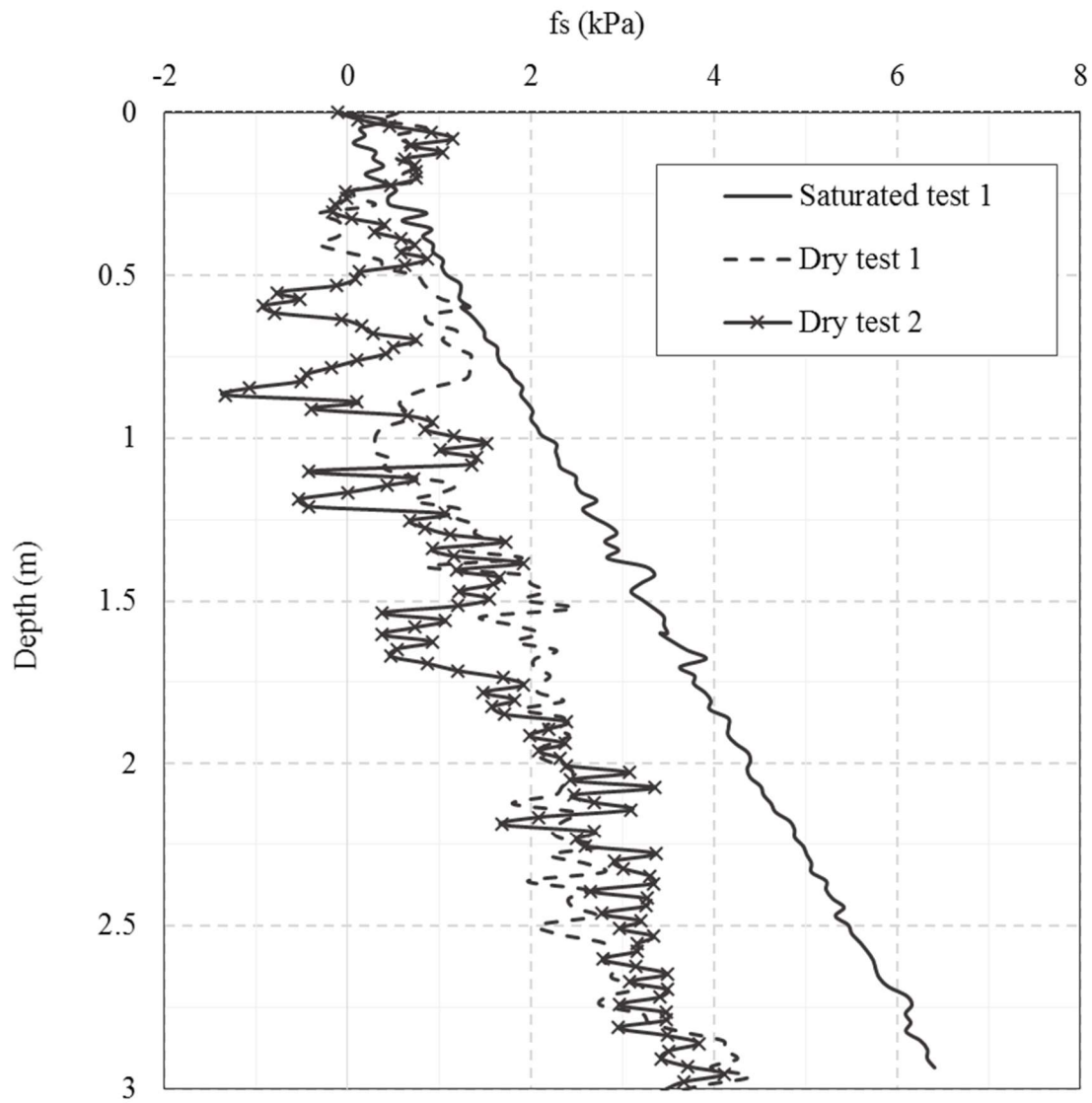Figure 7-27 Pore pressure measurements for the whole test and three penetration intervals of S2S
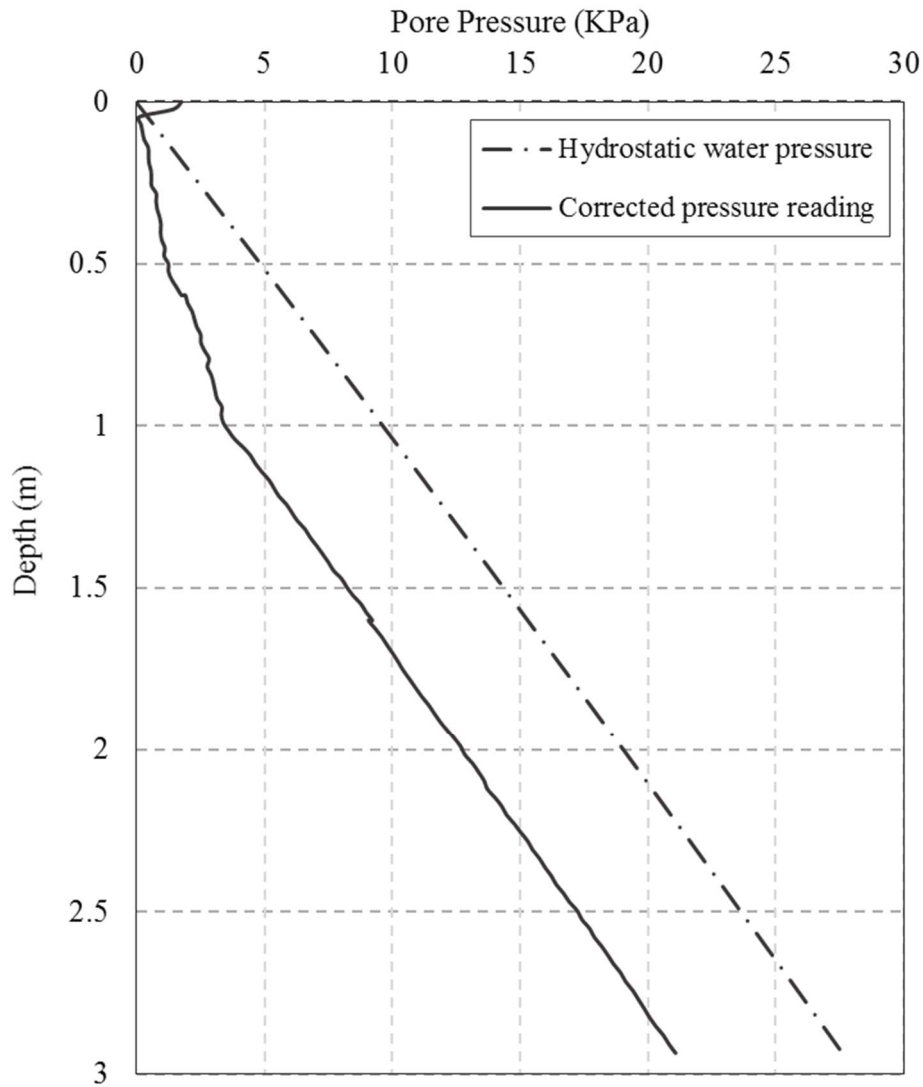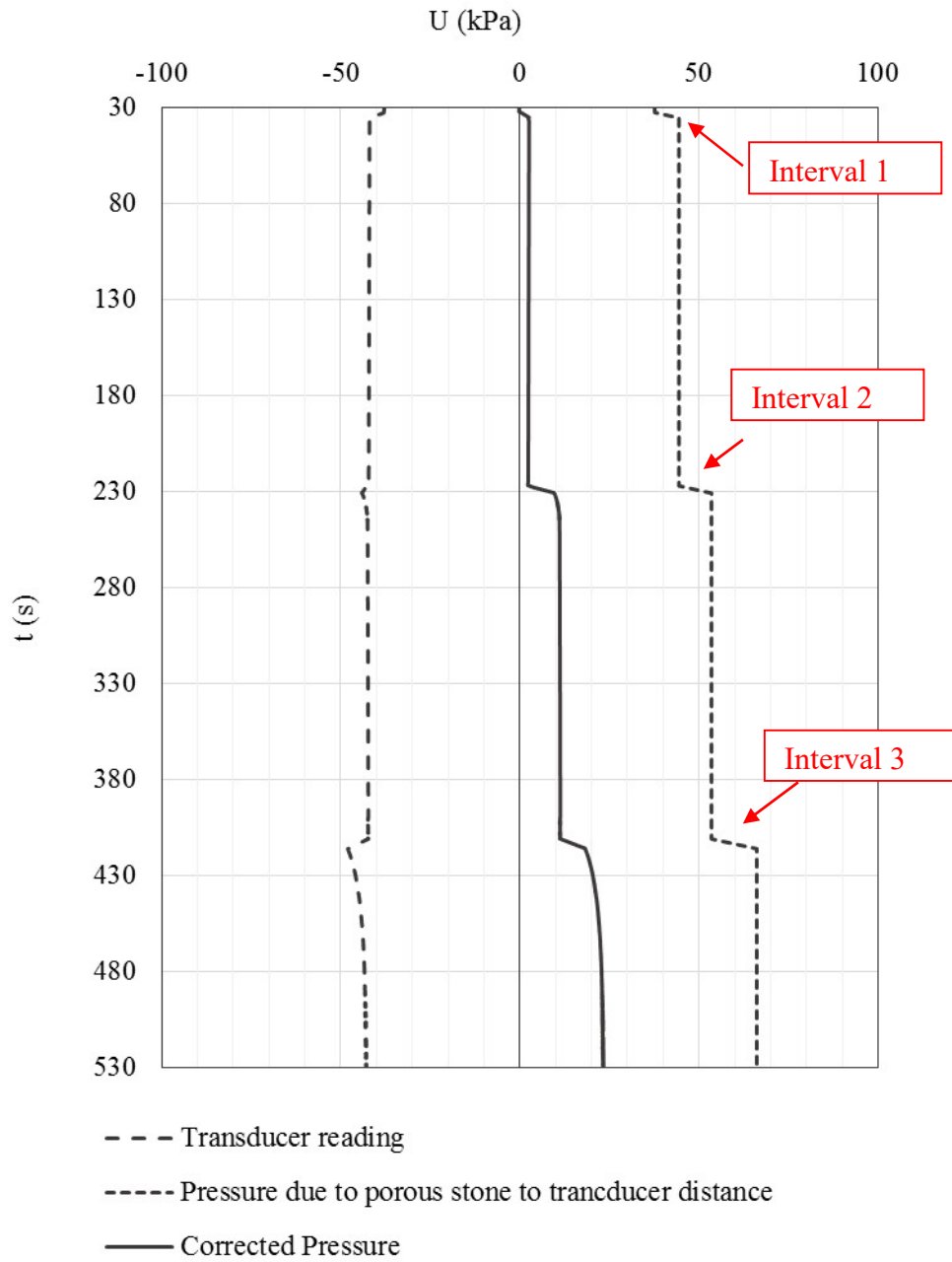
Figure 7-28 Pore pressure correction of S2S
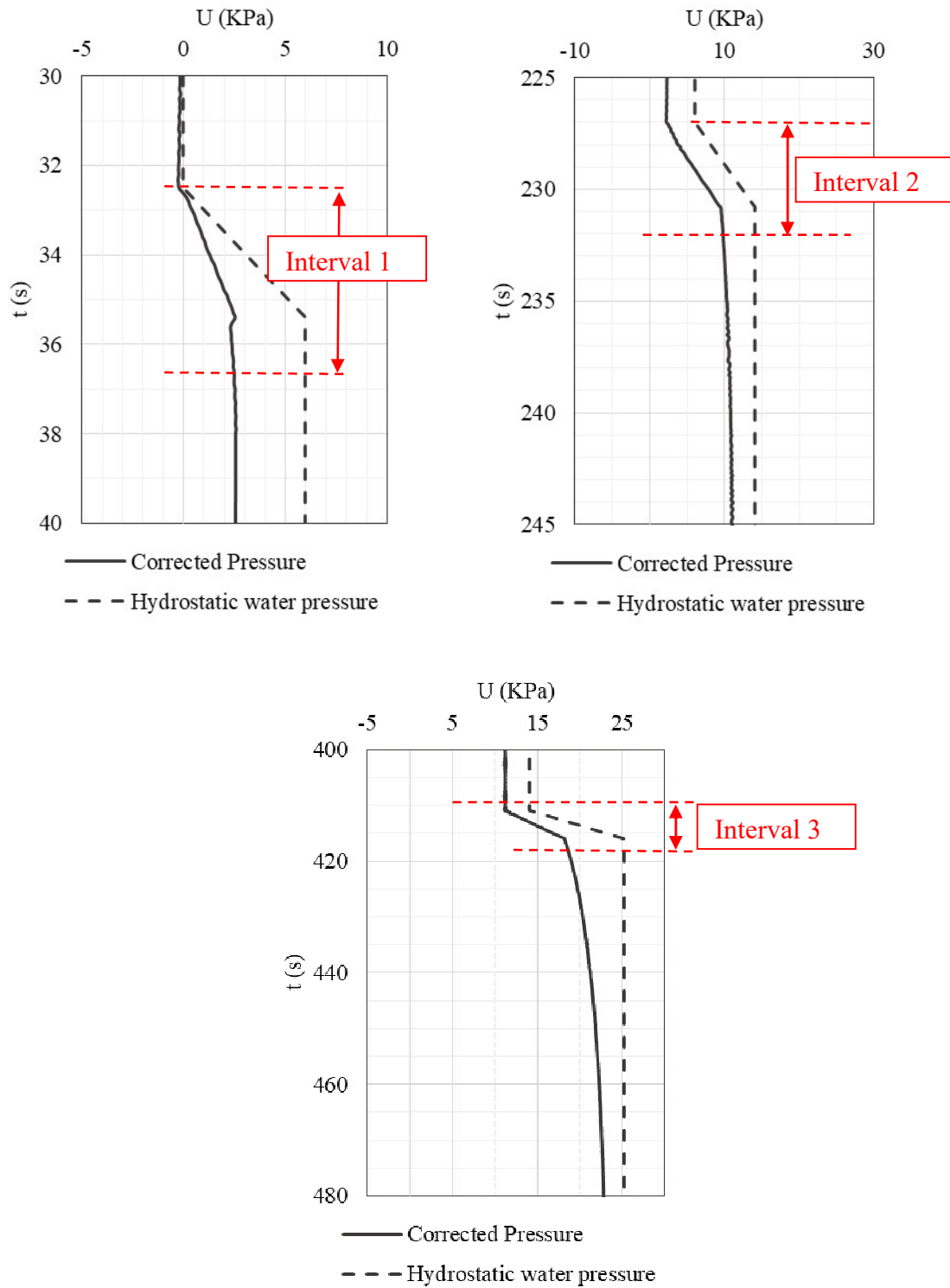
Figure 77-29 Corrected pore pressure in comparison with hydrostatic pressure

7.3.2.2 Unsaturated test (S2U)

In the following, the results of penetration test in unsaturated soil 2 are presented through Figures 7.30 to 7.36. This test was done in three intervals. Three dielectric sensors and three PPTs were used in different layers based on instrument layout shown in Figure 6.5. The cone porous stone was sealed using vacuum grease as explained in section 4.5.1.

Figure 7.30 shows the cone tip resistance (q_c) profile while Figure 7.31 shows this profile in comparison with saturated test. As it can be seen, the q_c values of unsaturated condition are higher than saturated condition which is consistent with the literature and results of soil 1. It can be said that in unsaturated condition, the q_c value is about 50% higher than saturated ones.

Figure 7.32 shows the sleeve friction (f_s) profile while Figure 7.33 shows this profile in comparison with saturated tests. As it is shown, the sleeve friction in unsaturated condition is 2 times higher than saturated condition. This ratio is much less than the ratio of soil 1 where, the sleeve friction in unsaturated condition was 10 times higher than dry and saturated condition

Figure 7.34 shows PPT readings before and after the penetration test. As it is shown, before the test and during the centrifuge spinning up, PPTs measured the hydrostatic water pressure (the sample was saturated) and after the test, all three PPTs, measure the same matric suction of about 3.5 kPa which confirms constant suction profile in depth. Figure 7.35 shows the pressure measurements for the three penetration intervals. Similar to previous tests, they were shown for a while before and after each interval for better explanation. As explained before, the negative values are generated because of the pressure due to distance between cone and transducer. Figure 7.34 shows the correction procedure while Figure 7.35 magnifies the corrected pore pressure for each interval. As it is shown, the matric in the first interval is about 7 kPa and 9 kPa before and after the interval respectively. This value is higher than the matric suction measured by PPTs. However,

in the second and third interval, before penetration, the predicted matric suction by transducer is about 3.5 kPa which is close to the PPT measurements. Then during the penetration, there is excess pore pressure which causes the pore pressure to increase about 6 kPa and after penetration, the pressure decreases and becomes stable at matric suction of 2 kPa.
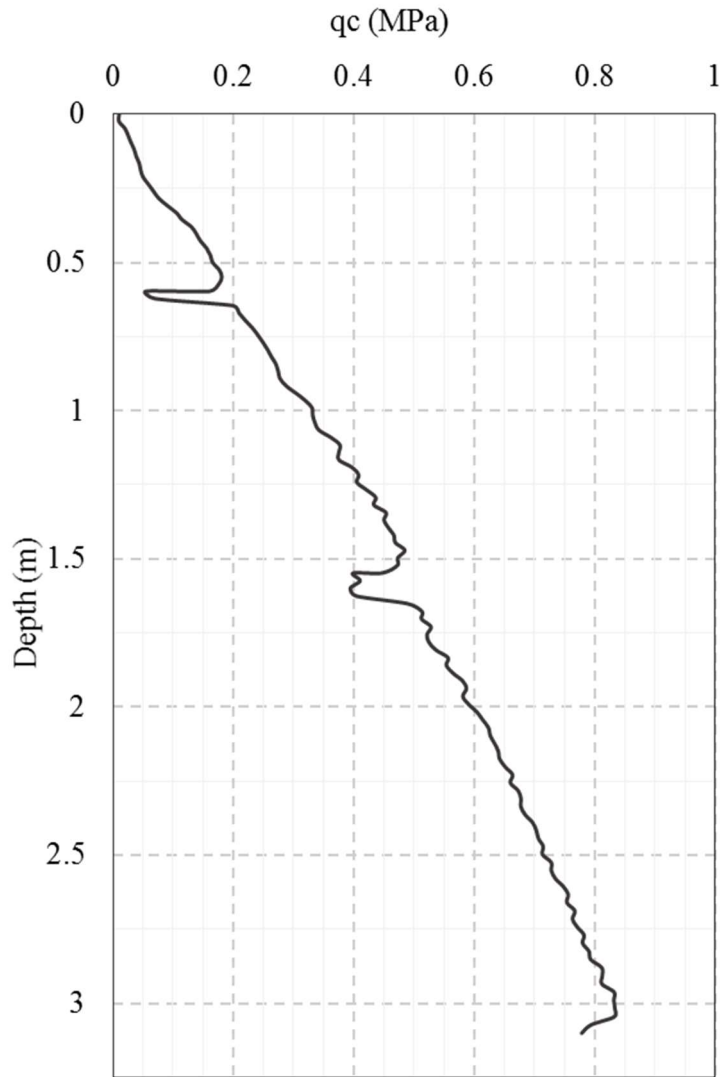
Figure 7-30 Tip resistance (qc) profile of penetration test of S2U
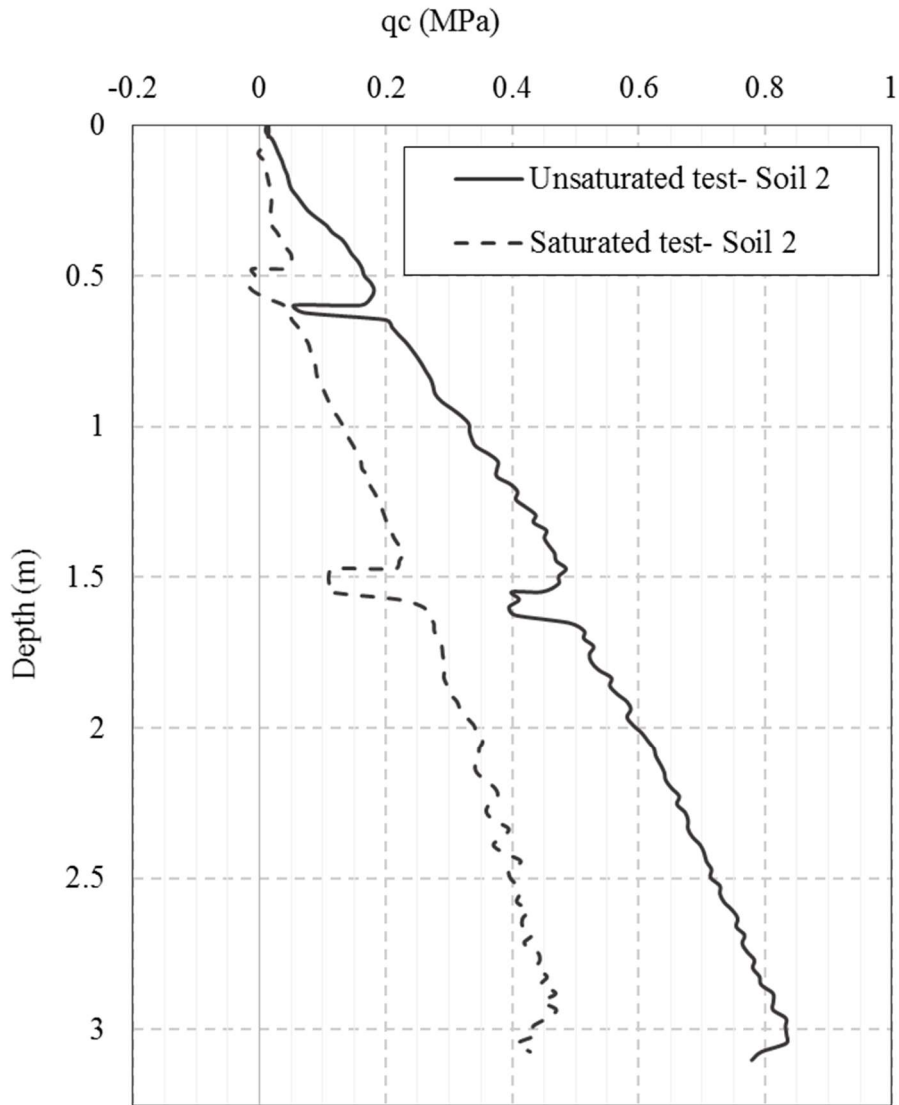
Figure 7-31 Comparison of tip resistance (qc) profile of penetration test of S2S and S2U
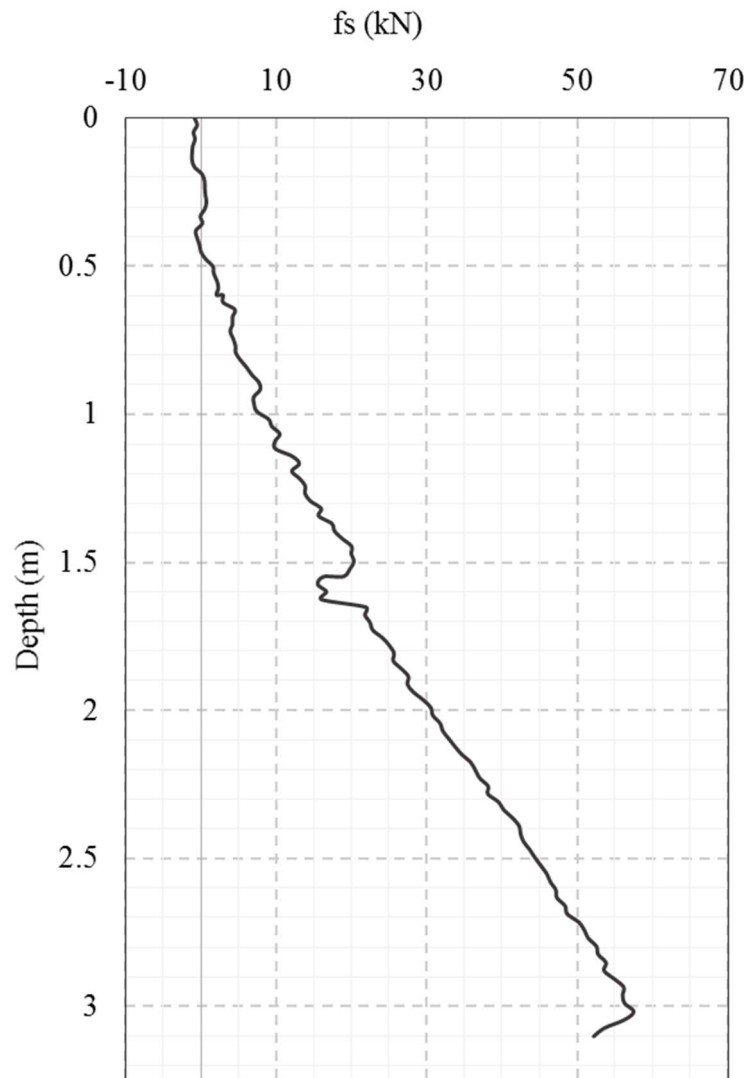
Figure 7-32 Sleeve friction (fs) profile of penetration test of S2U
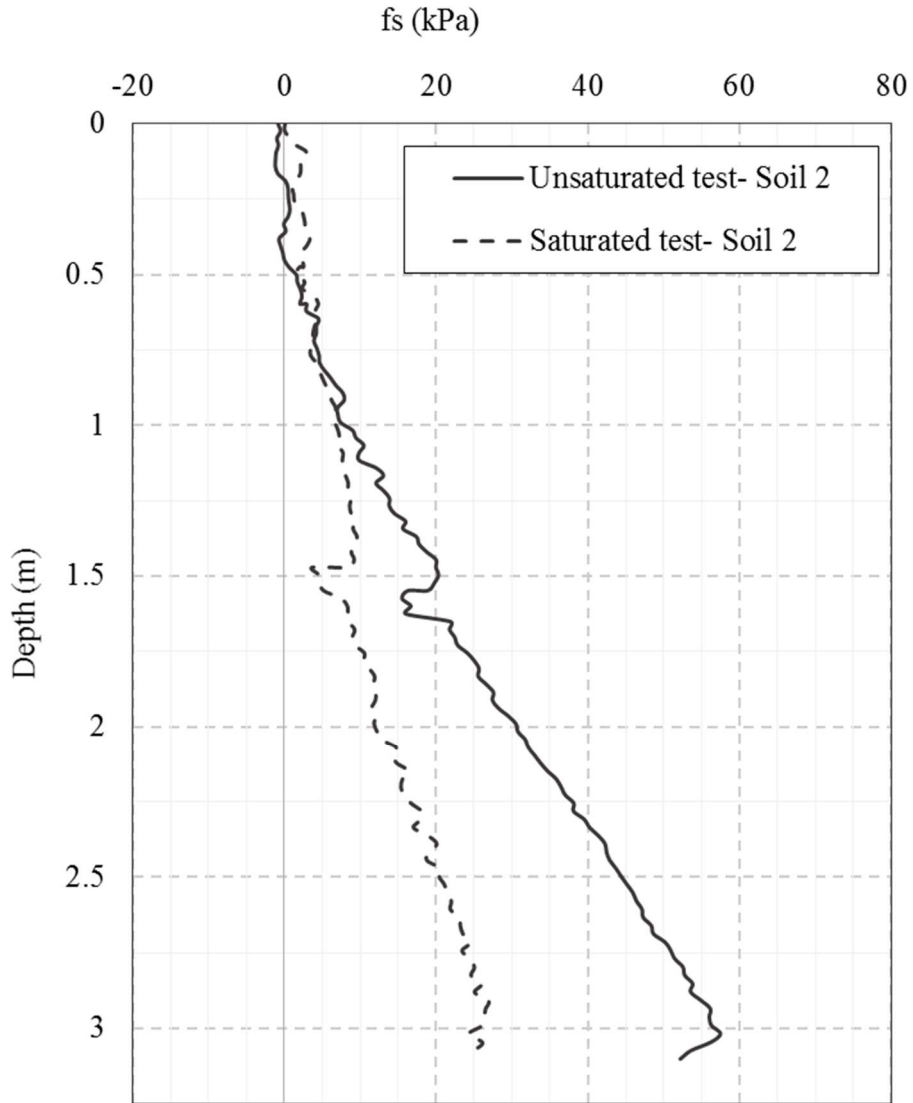
Figure 7-33 Comparison of sleeve friction (fs) profile of penetration test on saturated and unsaturated sample 2 (S2S, S2U)
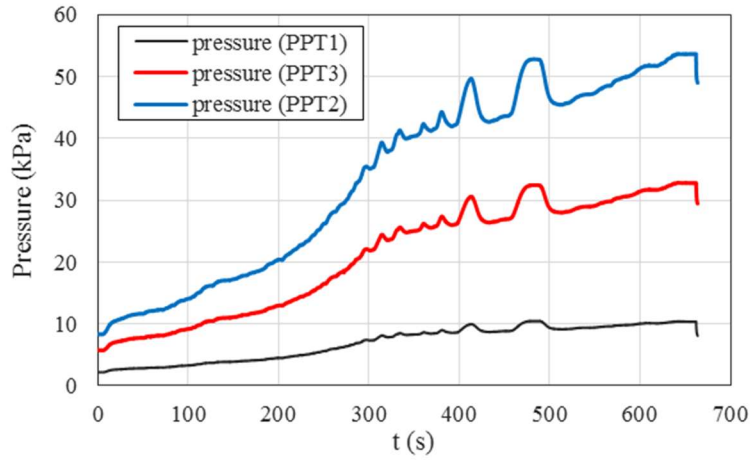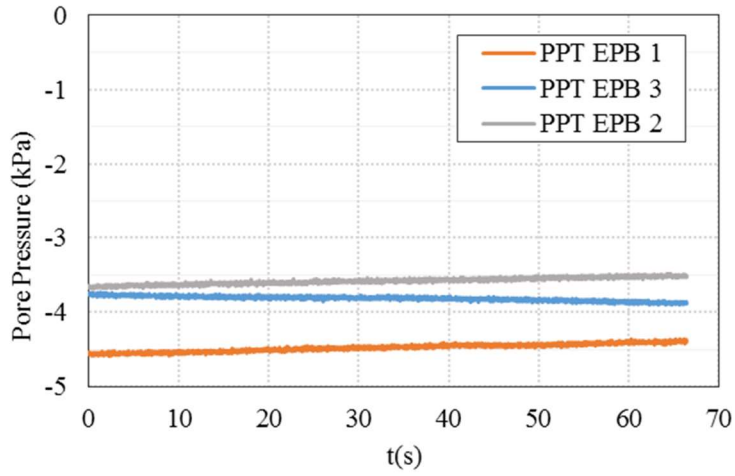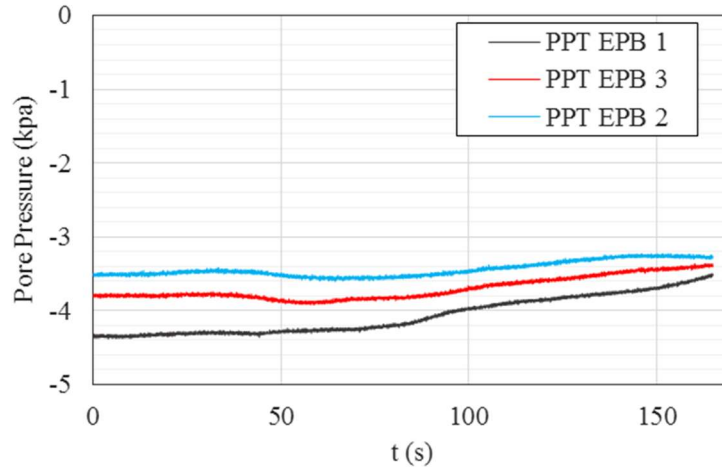
Figure 7-34 PPTs readings (a) before test and during spinning (b) After opening valves for infiltration (c) after penetration test
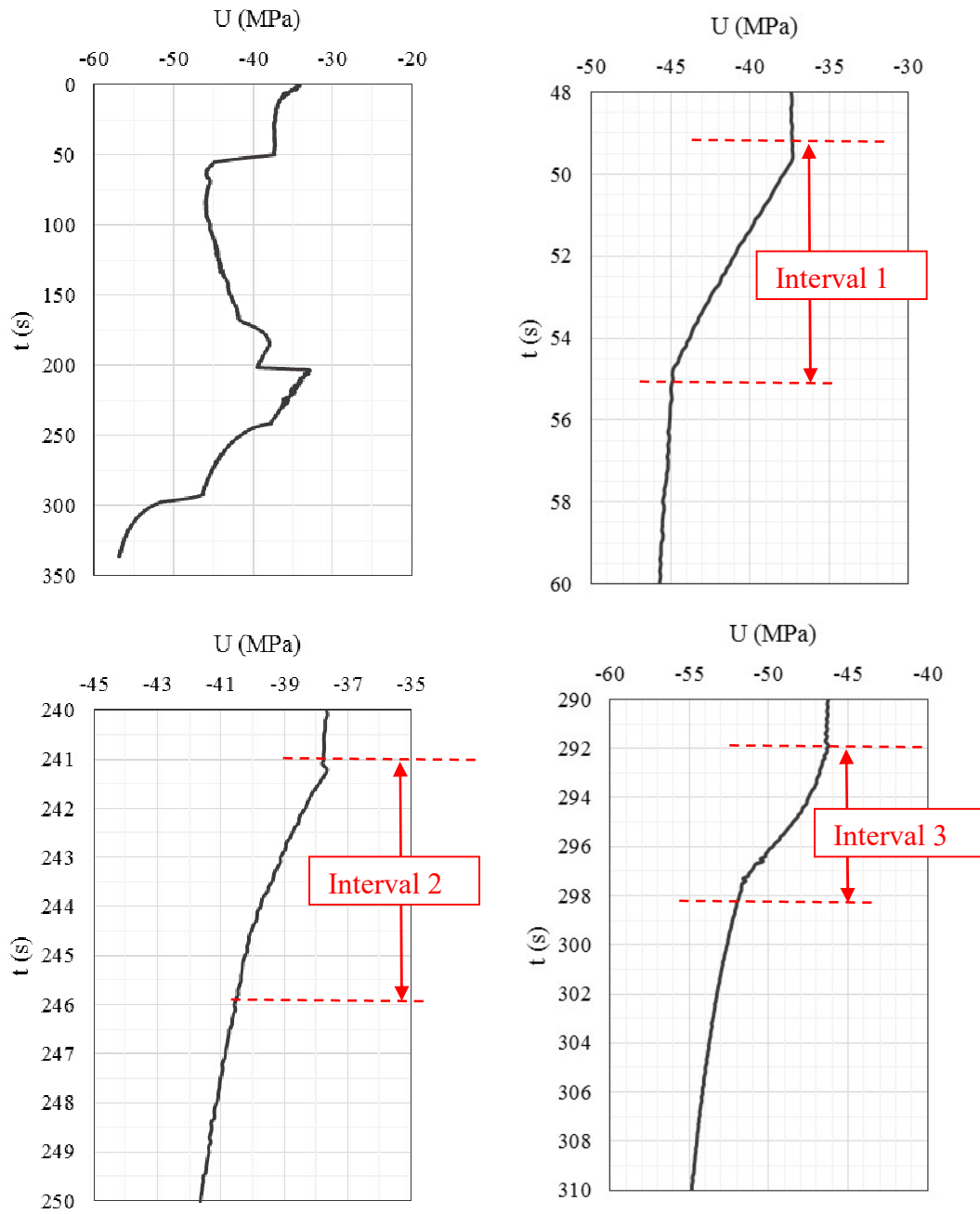
Figure 7.34. Pore pressure measurements for the whole test and three penetration intervals of

unsaturated test 2
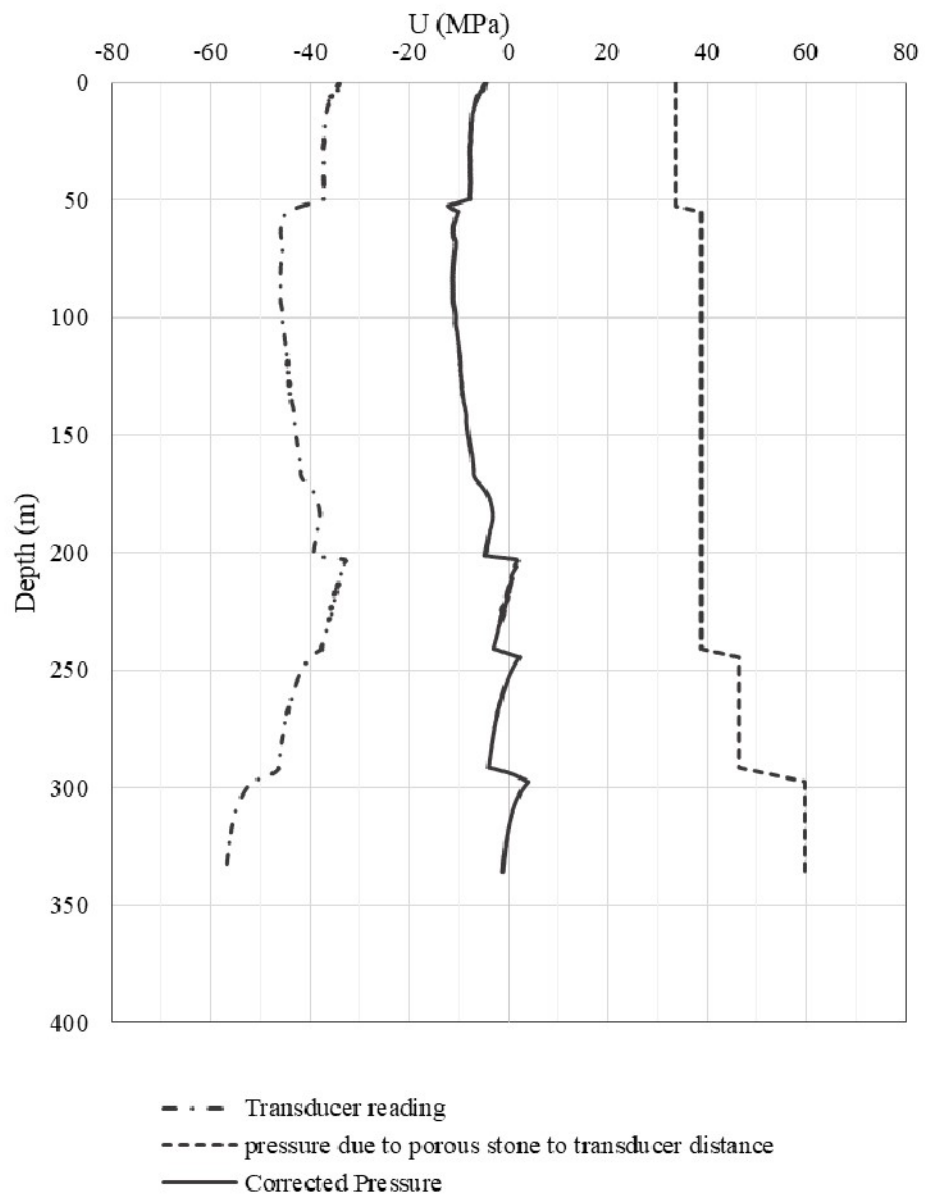
Figure 7-35 Pore pressure correction of S2U
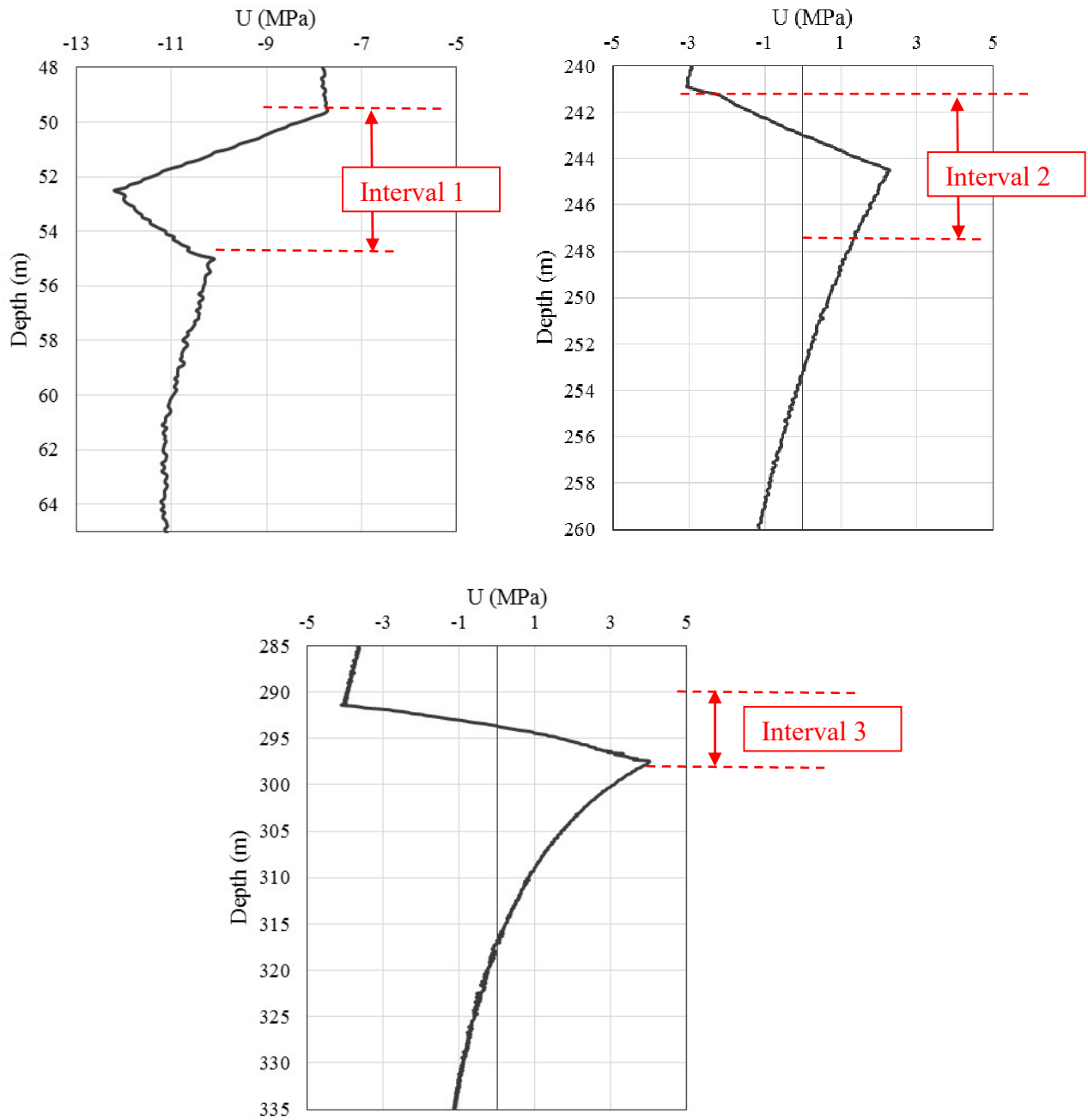
Figure 7-36 Pore pressure correction of S2U

7.4 Discussion on the CPT Results

The results of cone penetration tests, presented in section 6.3, are summarized in Table 7.2. The values presented in this table is corresponding to the maximum penetration depth (end of the test).

Table 7-2 Cone penetration results in different saturation condition at maximum penetration depth

Test	Cone tip resistance q_c (MPa)	Sleeve friction f_s (kPa)	Pore water pressure u (kPa)	Hydrostatic pressure (kPa)	Matric suction (kPa)
S1-D1	1.1	4	-	-	-
S1-D2	1	4	-	-	-
S1-S	0.7	6.5	21	27	-
S1-U	1.2	65	-	-	-
S2-S	0.48	27	23	26	-
S2-U	0.85	67	- 3	-	-4

As it is shown, the cone tip resistance in unsaturated condition is higher than dry or saturated conditions for both tests (about 50 % higher than saturated condition). However, the measured sleeve friction data are a little doubtful. It was expected to have higher sleeve friction values in unsaturated condition but 10 times and 2.5 times increase (for soil 1 and 1 respectively) seems to be too much. There is a possibility that after performing dry and saturated tests on soil 1, the cone calibration was changed and the recorded data are not reliable anymore. However, performing a calibration test for this load cell can clarify it and it is recommended before doing any more CPT tests.

Based on the pore pressure measurements, it can be concluded that the transducer prediction of pore pressure in saturated condition is close to hydrostatic pressure. Although, the results of two saturated tests are a little different in case of existence of extra pore pressure. In soil 1, no extra pore pressure is observed while in another one there is an extra pore pressure of about 2 kPa. In unsaturated test, the transducer measurements show that it is capable of measuring suction and the saturation method used was efficient. However there is a kind of excess pore pressure in the measurements and more data is needed before any further conclusion.

Chapter VIII

Cone Penetration in Unsaturated Soils: Summary, Conclusions and Recommendations

8.1   Summary and conclusion

The objective of this research was to investigate the effect of unsaturated condition on CPT results. It consists of two parts. Numerical modeling and experimental testing.

In numerical modeling part, a finite element model was developed using Abaqus/ Explicit and two unsaturated condition were considered using two different approaches: modifying an apparent cohesion in standard constitutive relations and implementing an elastoplastic constitutive model for unsaturated soils. Two models were developed, simulating the penetration test inside a calibration chamber with different constant suction values and penetration in free field soil layer inside a centrifuge with various ground water levels. Results showed that, the cone tip resistance in unsaturated soil is higher than dry or saturated condition and ignoring this effect can cause misestimating the soil strength properties. In addition, based on the results, it can be concluded that both approaches for considering the unsaturated condition are appropriate methods. However, using more complicated material models such as strain dependent constitutive models may improve the results.

In the experimental part of this study, a new miniature piezocone was designed, built and calibrated to be used for penetration tests on partially saturated soils. The piezocone and penetration set up were designed to fulfill the space limitations in UNH centrifuge. The piezocone is capable of measuring the cone tip resistance, sleeve friction and pore water pressure. It was first calibrated and the performance of load cells and pore pressure transducer was examined. Different methods for keeping the cone porous stone saturated were examined. Also, several tests including penetration tests in dry, saturated and unsaturated conditions were performed. Based on the results, it can be concluded that the cone tip resistance and sleeve friction in unsaturated condition is higher than dry and saturated condition. However, some uncertainly was observed in sleeve friction results where it was increased in unsaturated condition about 2 time comparing to dry and saturated tests for one soil and 10 time for another soil. Thus, recalibration of this load cell, is recommended before any further tests. In addition, the pore pressure measurements show that the transducer is capable of estimating the hydrostatic pressure with about 10% error (results of penetration tests in water and saturated soil). It proves the efficiency of the method used to keep the cone porous stone saturated (using vacuum grease). In unsaturated condition, the matric suction was measured by transducer but results were not consistent. As an example the pressure change in different intervals of one test can be observed. Performing more unsaturated tests, can help to check the repeatability of the results and more reliable conclusion can be taken.

8.2 Recommendations

A recommendation for future research would be to perform more experimental test on different soil samples and saturation conditions to extend the database needed for an accurate conclusion on the effect of unsaturated condition on CPT results.

Using a transducer with lower capacity (the capacity of the one used in this study is 1 MPa), may help to improve the accuracy of suction measurements. It is important as the range of matric suction that could be produced in Ottawa sand is less than 10 kPa and it is required to have enough accurate measurements by transducer.

Using more complicated material model to consider the compressibility of soil during penetration can help to improve the numerical results as well.

Having enough data from experimental tests, the soil strength properties can be estimated for different saturation condition to investigate the effect of partially saturated condition on estimations. In addition, the results can be used in combination with numerical models to develop new correlations for estimating the soil strength properties specifically for unsaturated condition and have a conclusion about the percentage of error in predicting the soil properties in case of ignoring the saturation condition.

Numerical Simulation of Fracture Propagation in Shale Rock

during Brazilian test

Chapter IX

Brazilian Test on Shale Rock: Motivation and Approach

9.1 Research Motivation

Acquiring a clear understanding of the rock failure mechanism is a key step in addressing many rock engineering problems such as rock cutting, blasting, oil and gas production, geothermal systems, hydraulic fracturing, safety of nuclear waste repositories and geological carbon storage units. This knowledge will also assist scientists and engineers to predict the long-term structural performance of various geological systems which may have significant environmental impacts. As an example, the safety and long-term effectiveness of a Carbon storage reservoir depends on the macro-fracture behavior, in turn, depends on micro-fracture response. Thus, a robust understanding of basic fracture propagation in small scale is a necessary step before predicting the large scale behavior of rock systems (Rutqvsist at al. 2008; Rinehart et al. 2015).

The understanding of fracture in rock can be better achieved upon accurate numerical modeling and conducting experimental fracture tests such as notched three-point bending test (N3PBT), short-rod test, and/or Brazilian test. Different testing strategies should be compared to determine the preferred testing method depending on the application. However, Brazilian test has

been widely employed in rock mechanics due to the difficulties in performing direct uniaxial tensile stress test.

Many studies have been done to investigate the effect of different factors such as rock anisotropy, boundary condition, geomaterial ratio and inhomogeneity on Brazilian test response and rock fracture during this test. However, in most of the studies, a unique value for elastic modulus of rock is considered for both compression and tension. On the other side, several studies have shown that the tensile and compressive elastic modulus in rock may differ by a factor of 5-20 (Weinberger et al. 1994; Chamis et al.). Thus, this effect should be investigated together with other factors such as anisotropy for a more accurate modeling which is considered in this research.

9.2 Research Objectives/ Research Approach

The objective of this research is to investigate the effect of considering different elastic modulus in tension and compression and also anisotropy on rock response during Brazilian test. For this purpose, a numerical model was developed using FEM commercial software, Abaqus, to simulate the Brazilian test. A cohesive fracture model, Linear Softening Cohesive Fracture Model (LCFM), was used to predict the fracture growth during the test. A set of experimental results conducted on Mancos shale was used to calibrate the properties of the numerical model. Mancos shale is a heterogeneous shale and the effect of heterogeneity was considered in the model by defining different layers of material with different properties or defining it as a transversely isotropic material. In addition, a user material was implemented to consider different elastic modulus for rock in compression and tension. Based on the results, capability of LCFM in simulating the crack propagation and the importance of considering different compression and tensile elastic modulus in predicting the tensile strength and accurately modeling fracture propagation during Brazilian test is discussed.

Chapter X

Brazilian Test on Shale Rock: Background

10.1 Rock Fracture Model

Rock fracture is usually induced by the means of tensile stress, shear stress, or a combination of the two, referred to as mode I (opening mode), mode II (sliding mode), and mix-mode, respectively. The compression stress is less critical than tensile and shear stresses as the compressive strength of rock is much higher than its tensile strength (Perras and Diederichs 2014). In order to simulate the rock fracture in small scale, different approaches mostly focused on mode-I fracture such as linear elastic fracture models, equivalent crack models, (e.g. R-curve models), and cohesive fracture models (Bazant and Planas 1997; Gross and Seelig 2011) have been used. Also, there are fracture models considering tension, compression, and shear behavior of material, which are able to present mix-mode brittle material failure (Galvez at al 2002; Gui et al. 2015). Among these models, cohesive zone fracture models, introduced by Dugdale (1960) and Barenblatt (1962), become popular in modeling of geomaterial due to the proper balance between the conceptual-computational simplicity and predictive capability-accuracy. However, this model can't consider the effect of crushing on the crack evolution path as the crack zone is pre-defined in the model.

In CZM, a very thin interface of cohesive material is considered within the elastic domain representing the brittle material. The fracture happens gradually by the separation of material surfaces, which is in turn resisted by the cohesive traction in the process zone (the unbroken region of the cohesive zone which comprises the material that is partially damaged but still able to transfer load across the fracture) governed by a traction-separation law (Chen 2009). Figure 10.1 shows the general traction-separation response of a cohesive fracture model. An elastic response is illustrated from a traction of zero to a yield traction of σ_{yield}, strain hardening from σ_{yield} to a peak traction σ_{max}, and a strain softening from the displacement w_0 at σ_{max} to a displacement w_1 beyond σ_{max} (Planas et al. 2003).
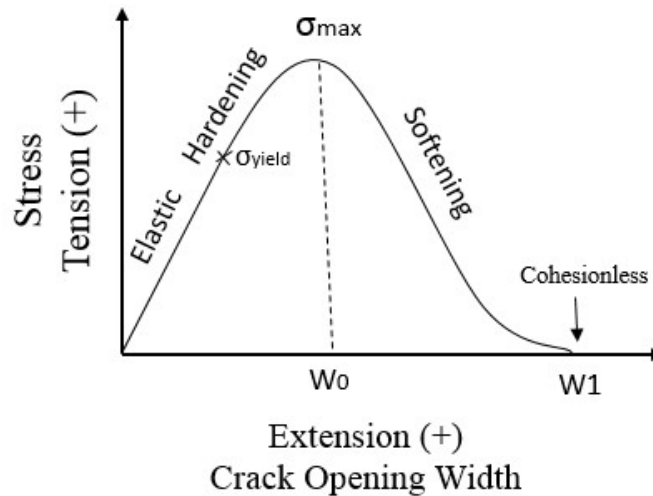
Figure 1010-1 Traction-separation response of a cohesive fracture model

The opening mode (mode I) fracture in rock models can be simplified using a Linear Softening Cohesive Model (LCFM) (Jaeger et al 2007). The LCFM traction-separation law includes a linear elastic behavior from $\sigma = 0$ to σ_{max} and a linear softening response from w_0 at σ_{max} to a displacement w_1 beyond σ_{max}, shown in Figure 10.2. LCFM has been successfully

implemented in geo-mechanical applications such as well bore-scale hydraulic fracturing (Boone et al. 1986; Yao 2012) and disk propagation (Rubin 1993).
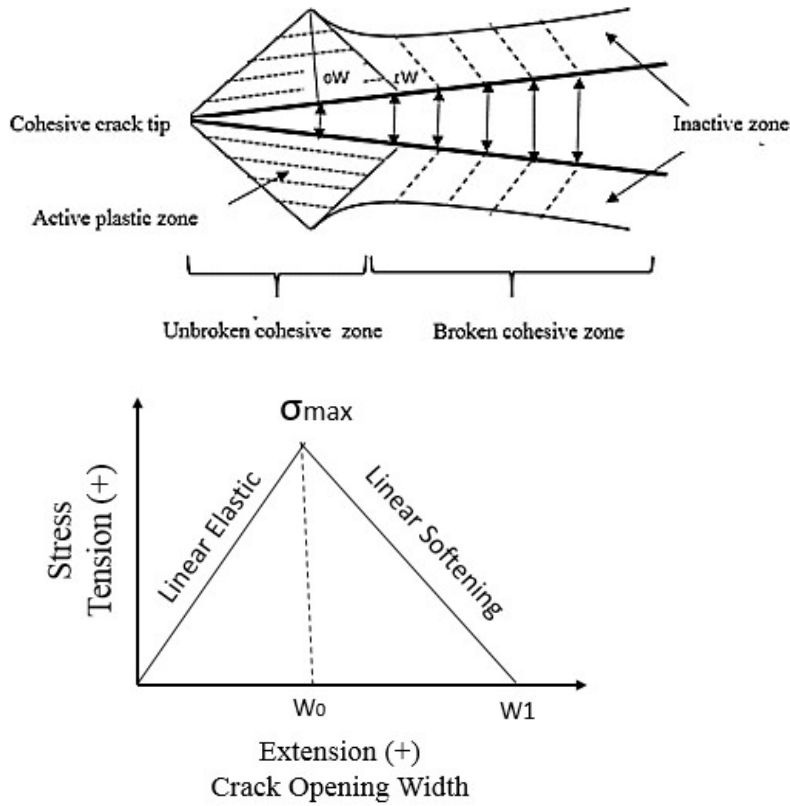
Figure 10-2Traction-separation response of a Linear Softening Cohesive Model (LCFM) (Rinehart et al. (20015))

10.2 Brazilian Test

Brazilian test is an indirect method for determining the tensile strength of brittle materials such as concrete and rock. It is widely used and become popular due to the difficulties in performing direct uniaxial tensile stress test. Although measuring the indirect tensile strength is the main purpose of this test, the fracture propagation during the test provides valuable insights with regards to the rock fracture mechanism. In this test, a diametrical compression load is applied on a thin circular disk of rock. Figure 10.3 shows the sample geometry and testing configuration.

The compression load induces tensile stress normal to the material diameter which is constant over an area around the center. The indirect tensile strength is calculated using the following equation (IRSM 1978) derived from the solution of elastic mechanics in a 2D disk (Timoshenko and Goodier 1990) given the failure occurs at the point of maximum tensile stress, i.e. the center of the disk.

$$\sigma_t = -\frac{2P}{\pi D t}$$
<div align="right">Eq. 10-1</div>

where, P is the maximum applied load, D is the diameter, and t is the thickness of the disk.
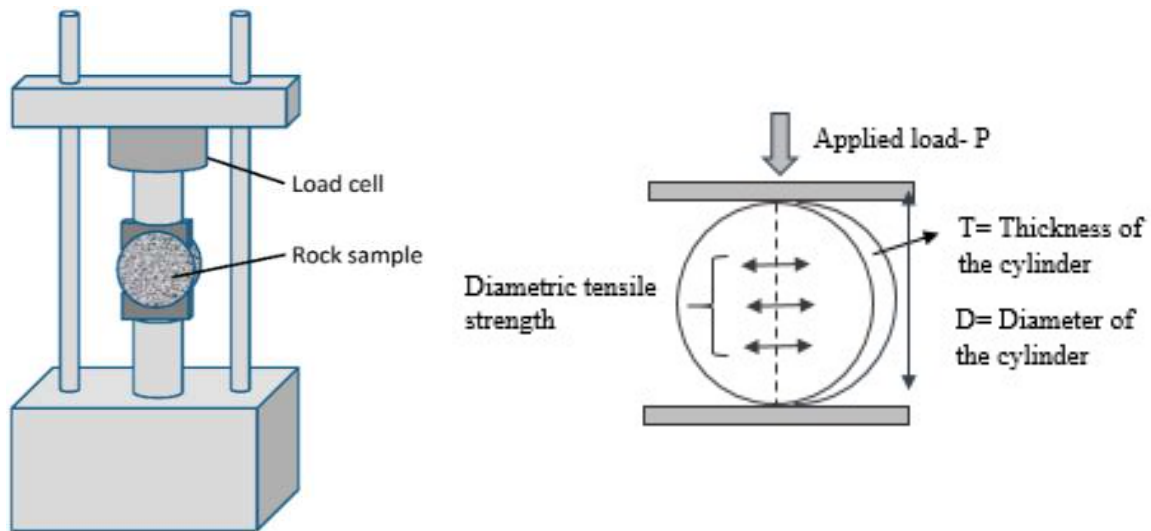
Figure 10-3 Sample geometry and testing configuration in Brazilian test (Abdul Mwanga et al. 2015)

10.3 Numerical Modeling of Brazilian Test

Historically, different factors affecting the results of the Brazilian test including rock anisotropy, boundary condition, geomaterial ratio and inhomogeneity, have been studied analytically, experimentally, and numerically (Fairhurst 1964, Chen et al. 1998a, b; Exadaktylos and Kaklis 2001; Cai and Kaiser 2004; Thuro et al. 2001, Rocco 1999, Chen 2004). In addition,

there are studies which have focused on simulating the fracture mechanism in this test using different methods such as Finite Element Method (FEM), Boundary Element Method (BEM), digital image processing-based finite element method, and Distinct Element Method (DEM) using different fracture models such as smeared rotating crack model, Flat-Joint model, and cohesive fracture model (Lanaro et al. 2009; Steen et al 2005; Yue et al 2003; Cai 2004, Fahimifar and Malekpour 2012; Gui 2015).

Although the fracture models are the key component in predicting the rock fracture, the value considered as an elastic modulus of rock play an important roles in the response as well. In most of the studies on the field of rock fracture, a unique value for elastic modulus of rock is considered for both compression and tension. However, it has been shown that the tensile and compressive elastic modulus in rocks may differ by a factor of 5-20 and assuming an equal elastic modulus in tension and compression can cause the flexural modulus to be underestimated by 35% (Weinberger et al. 1994; Chamis et al.). This could be attributed to the fact that the compressive stresses would close the voids and pre-cracks that makes the material stiffer; while tensile stresses would soften the material by opening the voids and pre-cracks. As a result, $E_{tension}$ becomes much smaller than $E_{compression}$. Reinhart et al. (2015) showed that linear softening cohesive fracture model (LCFM) cannot accurately describe the fracture during the N3PB test when single elastic modulus is assigned across the entire specimen. Thus, assigning different elastic modulus, one for tension and one for compression, improve the result and reduces disparity between computational data and experimental data (Borowski and Newell 2015). Thus, considering different elastic modulus in tension and compression together with an anisotropic material can simulate the rock behavior more accurately.

Chapter XI

Brazilian Test on Shale Rock: Experimental Data collection

11.1 Introduction

This research is a collaboration between University of New Hampshire and Sandia National Laboratories. The experimental data presented in this section are prepared by collaborator at Sandia National laboratories while the numerical modeling of the problem is the focus of this thesis. In the following sections, the details of both data collection and numerical modeling are explained.

11.2 Rock samples

Results of Brazilian test on cores of Mancos shale were used as the benchmark in this study. 25.4±0.24 mm diameter, 13±0.8 mm length samples were prepared and tested according to ASTM D3967 standard called 'Method for Splitting Tensile Strength of Intact Rock Core Specimens. Figure 11.1 shows a photo of the sample after the test. Tests were performed on a 22 kip load frame. Specimens were cushioned between the edge of the specimen and the platen interface with a single thickness of masking tape. This assists to reduce the stress concentration at the point of

loading. Also wrapping the specimen in masking tape and containing the specimen after failure allowed the confirmation of the fracture pattern observed with digital image contrast (DIC).
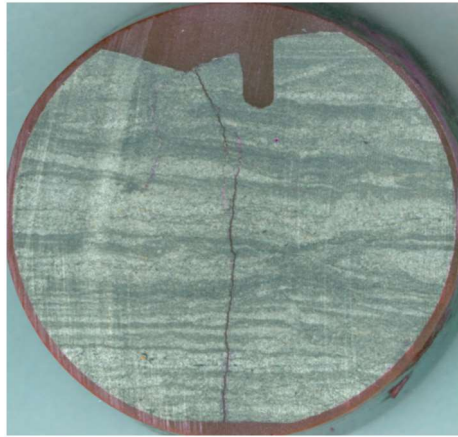
Figure 11-1 Mancos shale sample after Brazilian test

11.3 Brazilian Test Results

Results include stress-displacement graphs and DIC images of the sample during the test. Table 11.1 summarizes experimental condition and key experimental results including the splitting stress at failure, and the displacement from initial contact to achieve failure while Figure 11.2 shows the DIC and stress displacement result for the sample. This result is magnified for each step of test separately in Figures 11.3 to 11.6. The specimen showed axial splitting as the primary failure mechanism.

Table 11-1 Loading orientation, failure stress and displacement to failure of the Mancos shale specimen.

Specimen	Loading Orientation	Failure Stress (MPa)	Displacement to failure (mm)
Mancos Shale		4.548	0.54
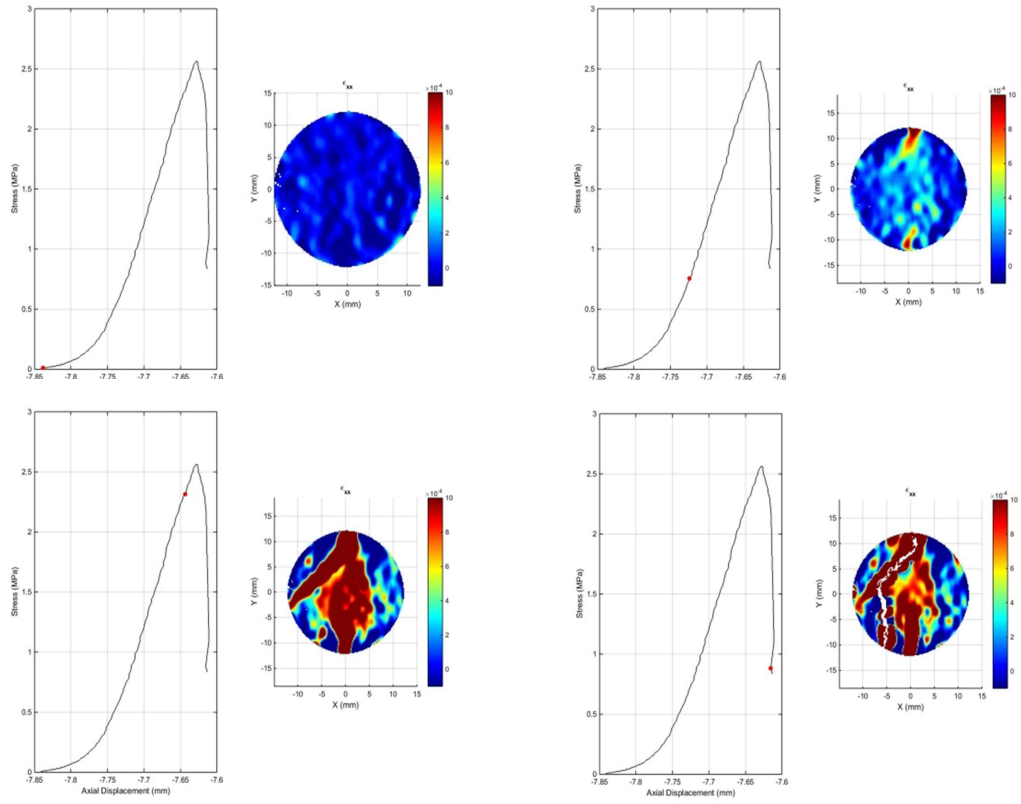
Figure 11-2 DIC and stress-displacement results of Mancos shale specimen
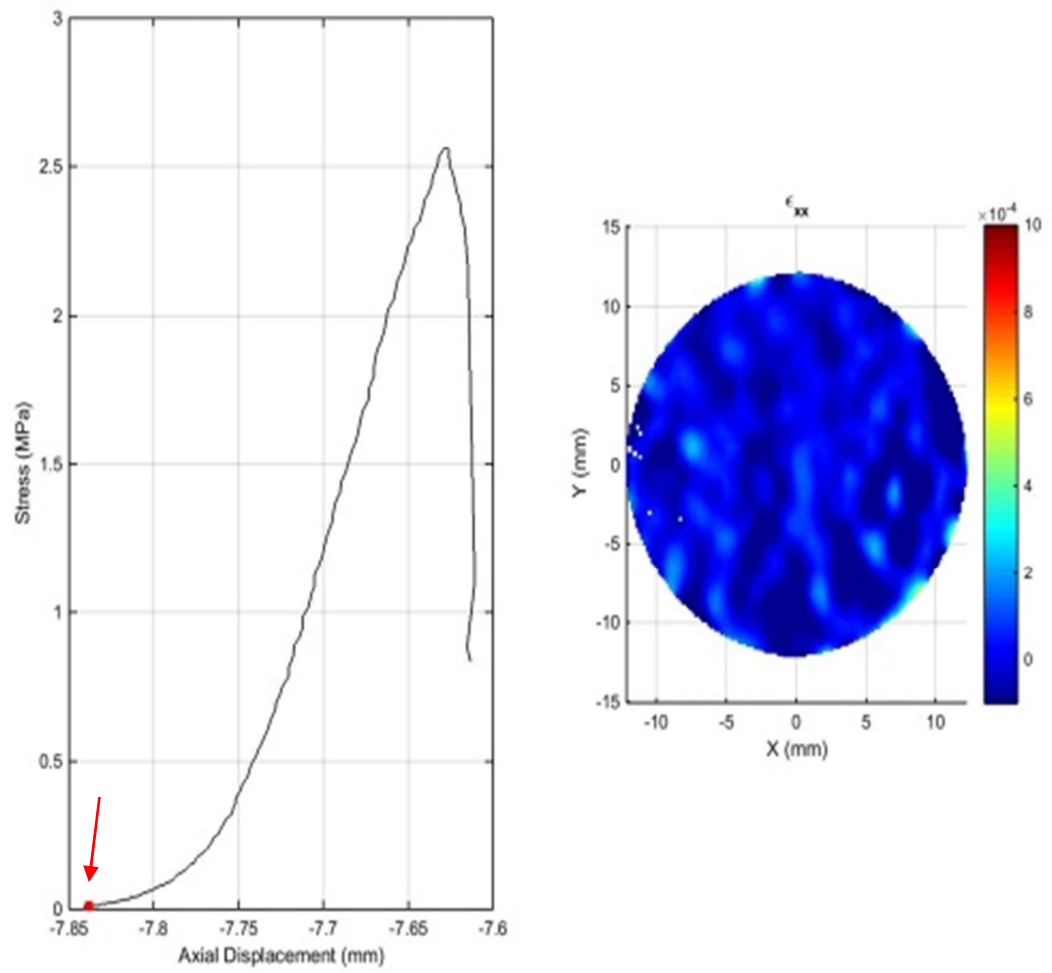
Figure 11-3 DIC and stress-displacement result of the specimen - interval 1
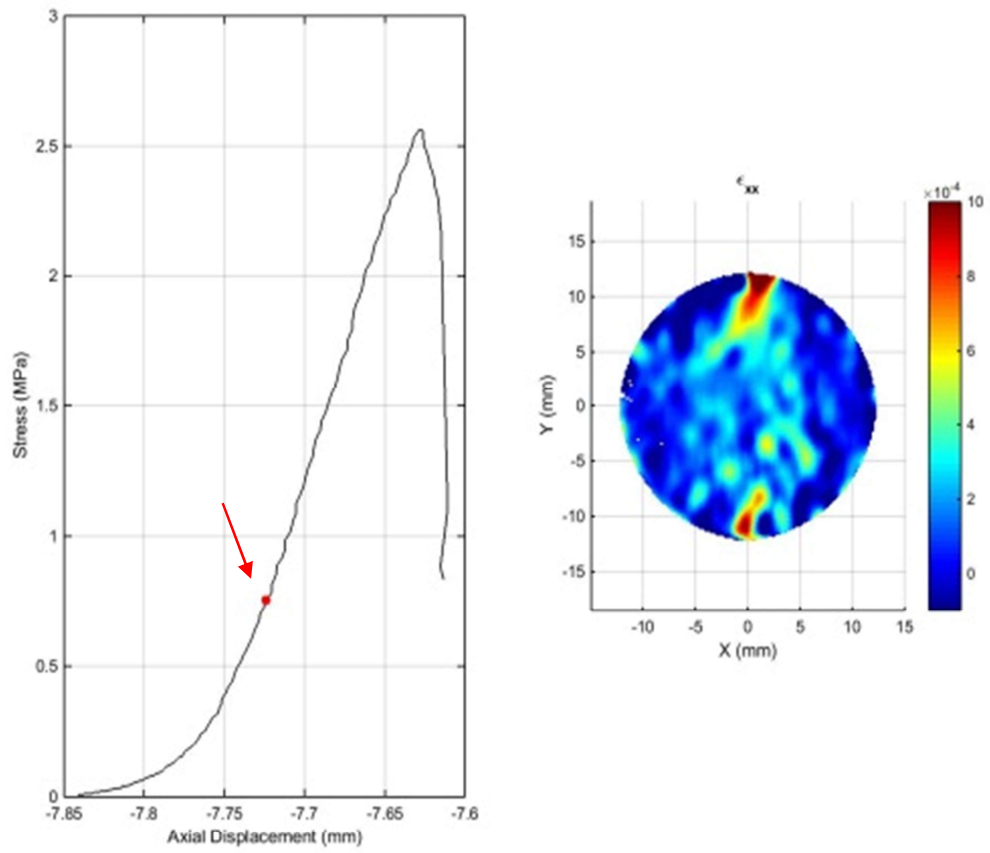
Figure 11-4 DIC and stress-displacement result of the specimen- interval 2
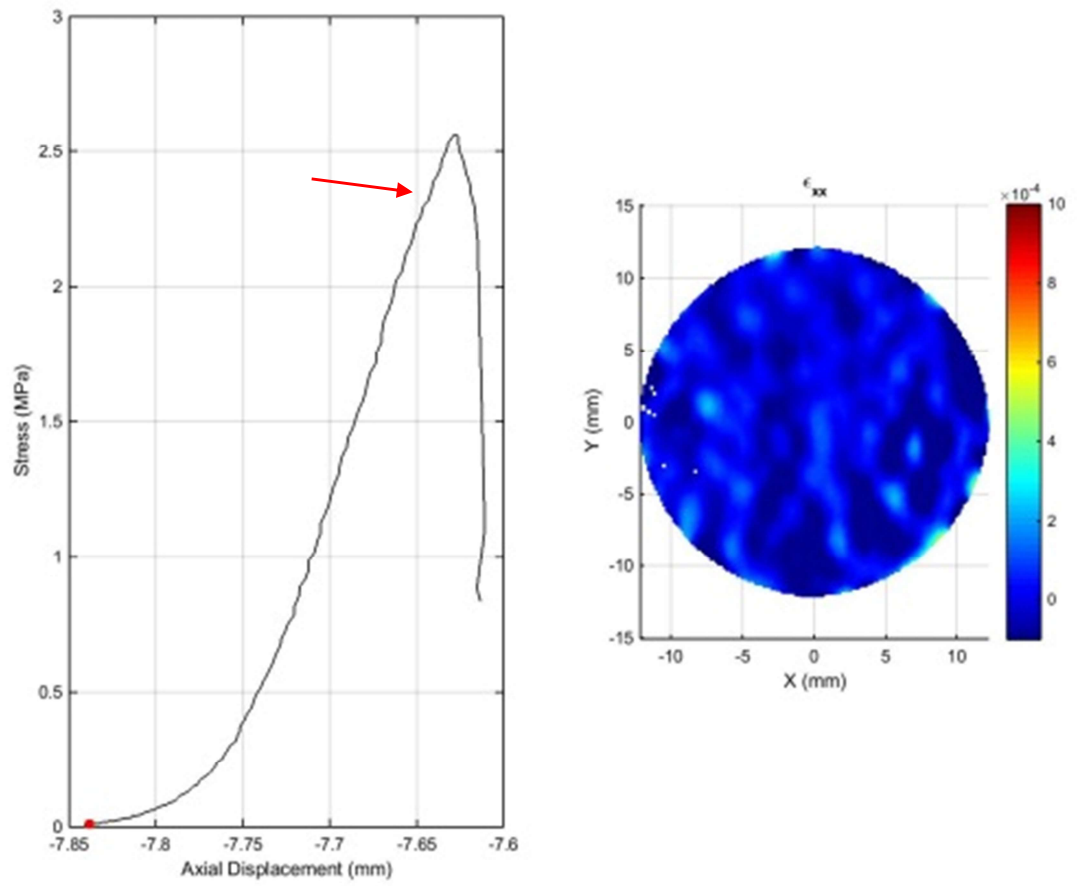
Figure 11-5 DIC and stress-displacement result of specimen - interval 3
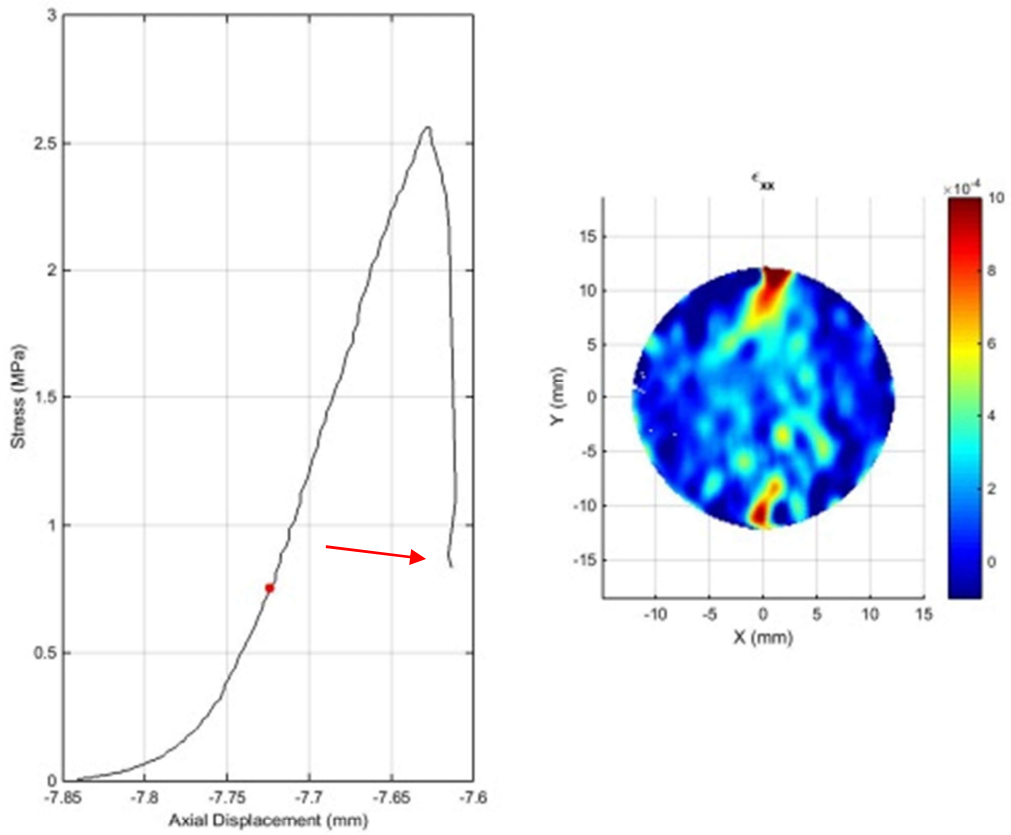
Figure 11-6 DIC and stress-displacement result of the specimen - interval 4

11.4   Layer Identification

As mentioned before, Mancos shale is a very heterogeneous rock. As it is shown in Figure 11.1, which is a real photo of sample B after the Brazilian test, different layers can be observed in the rock sample. The properties of different layers of each sample was identified by approximating the volume of stiff, intermediate and soft materials in each micro-lithofacies of samples and interpreting the elastic modulus and Poisson's ratio based on the study by Sone and Zoback (2013). Figure 11-7 shows the plot suggested in that research. Based on this identification method, four different material were defined which are distributed irregularly throughout the specimen. Figure 11.8 shows the layer configuration of sample B while Table 1.2 presents the corresponding material properties. In order to consider this layering in numerical model, the layers configuration was simplified as it is shown in Figure 11.9.
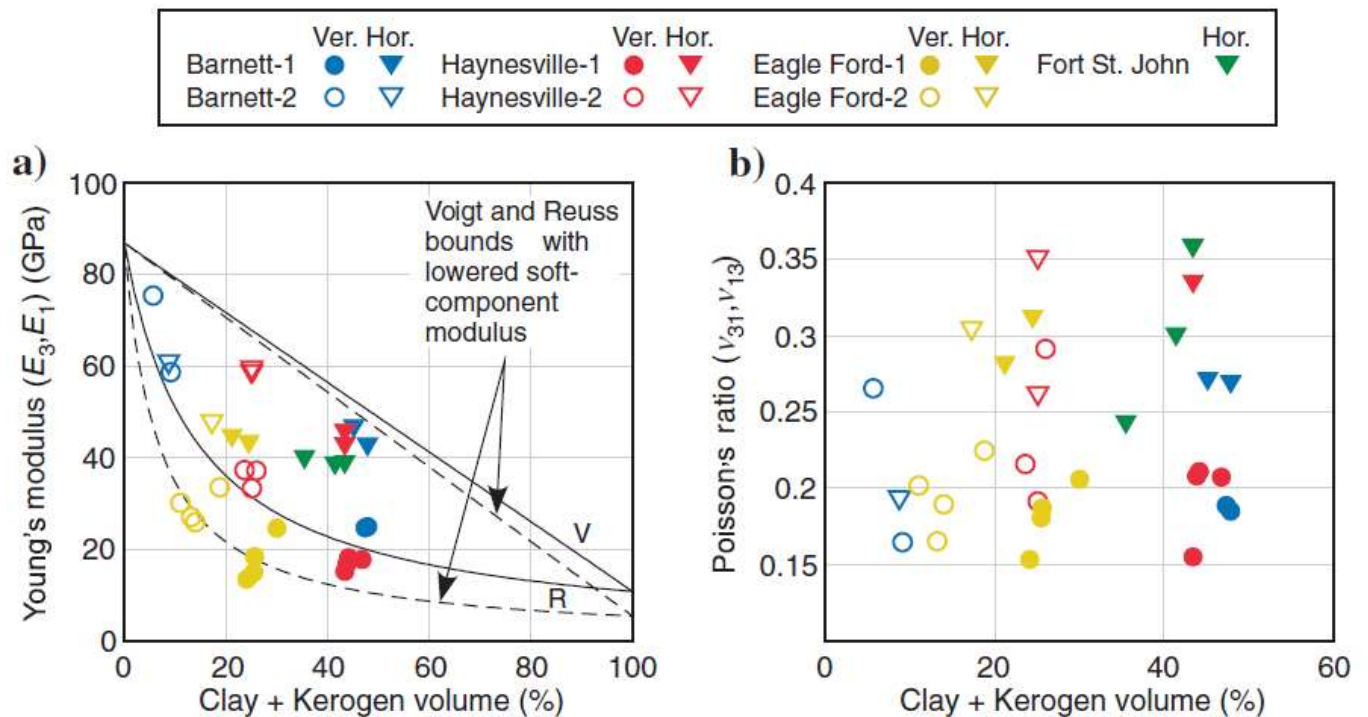
Figure 11-7 Static moduli data plotted against the sum of clay and Kerogen volume compared with Voigt/Reuss bounds (a) Static young's modulus. (b) Static poisson's ratio (Sone and Zoback, 2013)
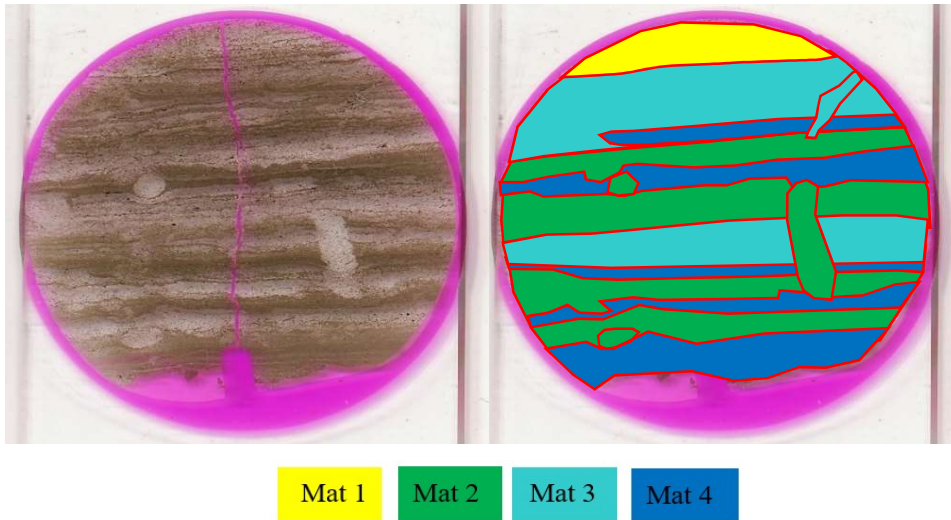
Figure 1111-8 Layer configuration of the sample

Table 11-2 Properties of different identified materials in Brazilian test sample B

Property	Mat 1	Mat 2	Mat 3	Mat 4
Young modulus (GPa)	75	40	20	10
Poisson's ratio	0.27	0.3	0.2	0.15
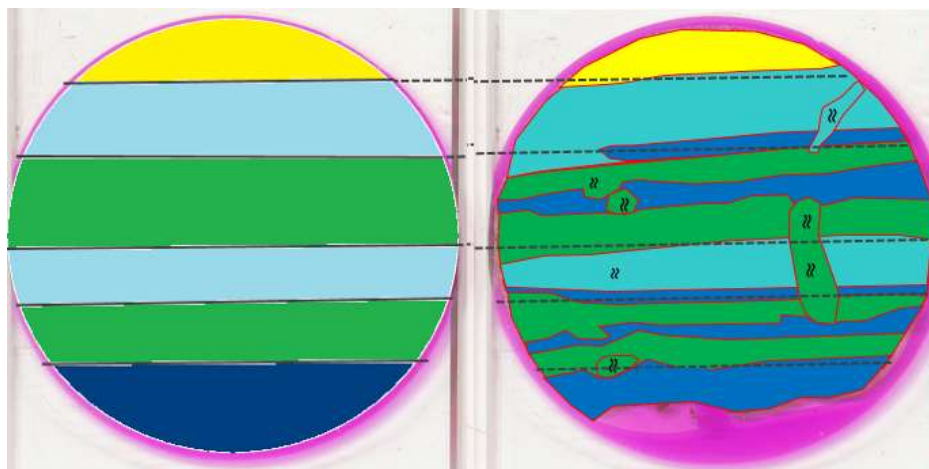
Figure 11-9 Simplified layer configuration of sample B

Chapter XII

Brazilian Test on Shale Rock: Numerical Simulation

12.1 Introduction

A numerical model was developed using Abaqus software in order to simulate the fracture process during Brazilian test. The capability of cohesive fracture model is examined and the importance of considering different elastic modulus in tension and compression was shown. In addition, the results were compared with a model of an anisotropic material.

In the first step, to calibrate the fracture model, Brazilan test was modeled considering an isotropic material for rock and ignoring the layering existed in the rock sample. The model was calibrated based on experimental results of the sample (presented in chapter 3). The outcome of this step was the material properties of rock and cohesive zone.

In the second step, to investigate the effect of considering the laying, a rock sample with multi-layers with distinct Young's modulus was modeled while same properties for cohesive zone as step 1 was considered. Model was calibrated again and results were compared to the model with one material for rock.

In the third step, to investigate the effect of considering different compressive and tensile elastic modulus, a user material subroutine (VUMAT) was adapted into Abaqus based on the work

by McCarty and Newell (2016). In this subroutine, two different elastic modulus for rock, one for tension and one for compression were defined and elastic modulus of each element at each time step was updated based on the stress state of that element. The result of this model was compared to the previous models in order to investigate the effect of different elastic modulus in tension and compression on rock response.

In the last step, the rock was assumed as a transversely isotropic material and its response was compared with isotropic materials considered in previous steps.

In the following sections, details of these simulations are presented.

12.2 Material Models

In this study, rock is considered as a linear elastic material. In the following (section 4.2.1 and 4.2.2), the two linear elastic material used for simulations of this study are explained. The rock response after cracking could be defined using plasticity models or fracture models. Here, the rock response after cracking is modeled using the cohesive zone model, which is explained in section 4.2.3.

12.2.1 Linear elastic model for isotropic material

Linear isotropic material refers to materials in which the properties are independent of direction. In isotropic material, the relation between stress and strain is defined with a line, the slope of which is known as elastic modulus (E) and the compliance matrix can be written as:

$$\begin{Bmatrix} \varepsilon_{xx} \\ \varepsilon_{yy} \\ \varepsilon_{zz} \\ \varepsilon_{yz} \\ \varepsilon_{zx} \\ \varepsilon_{xy} \end{Bmatrix} = \frac{1}{E} \begin{bmatrix} 1 & -\upsilon & -\upsilon & 0 & 0 & 0 \\ -\upsilon & 1 & -\upsilon & 0 & 0 & 0 \\ -\upsilon & -\upsilon & 1 & 0 & 0 & 0 \\ 0 & 0 & 0 & 1+\upsilon & 0 & 0 \\ 0 & 0 & 0 & 0 & 1+\upsilon & 0 \\ 0 & 0 & 0 & 0 & 0 & 1+\upsilon \end{bmatrix} \begin{Bmatrix} \sigma_{xx} \\ \sigma_{yy} \\ \sigma_{zz} \\ \sigma_{yz} \\ \sigma_{zx} \\ \sigma_{xy} \end{Bmatrix} \qquad \text{Eq. 12-1}$$

where ϵ_{ij} and σ_{ij} are strain and stress components, E is the elastic modulus and v is the Poisson's ratio. As it can be seen, such material have only two independent variables in their compliance (or stiffness) matrix. The input parameters of this model in Abaqus, are Elastic modulus (E) and Poisson's ratio (v). Thus, for models with one isotropic material for rock, it is needed to have one elastic modulus and one Poisson' ratio while for models with layers, these two parameters should be defined for each layer.

12.2.2 Linear elastic model for transversely isotropic material

By definition, transversely isotropic material are a special class of orthotropic material that have the same properties in one plane (e.g. the x-y plane) and different properties in the direction normal to this plane (e.g. the z-axis). The compliance matrix for this type of material takes the following form:

$$
\begin{Bmatrix} \varepsilon_{xx} \\ \varepsilon_{yy} \\ \varepsilon_{zz} \\ \varepsilon_{yz} \\ \varepsilon_{zx} \\ \varepsilon_{xy} \end{Bmatrix} = \frac{1}{E}
\begin{vmatrix}
\dfrac{1}{E_p} & -\dfrac{v_p}{E_p} & -\dfrac{v_p}{E_z} & 0 & 0 & 0 \\
-\dfrac{v_p}{E_p} & \dfrac{1}{E_p} & -\dfrac{v_{zp}}{E_z} & 0 & 0 & 0 \\
-\dfrac{v_{zp}}{E_z} & -\dfrac{v_{zp}}{E_z} & \dfrac{1}{E_z} & 0 & 0 & 0 \\
0 & 0 & 0 & \dfrac{1}{2G_{zp}} & 0 & 0 \\
0 & 0 & 0 & 0 & \dfrac{1}{2G_{zp}} & 0 \\
0 & 0 & 0 & 0 & 0 & \dfrac{1+v_p}{E_p}
\end{vmatrix}
\begin{Bmatrix} \sigma_{xx} \\ \sigma_{yy} \\ \sigma_{zz} \\ \sigma_{yz} \\ \sigma_{zx} \\ \sigma_{xy} \end{Bmatrix}
\qquad \text{Eq. 12-2}
$$

where $\dfrac{v_{pz}}{E_p} = \dfrac{v_{zp}}{E_z}$.

As it can be seen, there are 5 independent elastic constants in the compliance matrix including the Young's modulus and Poisson's ratio in the x-y symmetry plane, E_p and v_p, the

Young's modulus and poisson ratio in the z-direction, E_z and ν_{pz}, and the shear modulus in the z-direction G_{pz}. G_{pz} can be found using Equation 12.3 by St. Venant's (1863) formula:

$$\frac{1}{G_{zp}} = \frac{1}{E_z} + \frac{1}{E_p} + 2\frac{\nu_{zp}}{E_z} \qquad\qquad \text{Eq. 12-3}$$

In Abaqus, these five parameters should be defined as input values of material model.

12.2.3 Linear Softening Cohesive Model (LCFM)

Different fracture cohesive models were introduced in section 2.1. For this study, Linear Softening Cohesive Model (LCFM) with maximum stress damage initiation and separation criteria was used as constitutive material for cohesive elements. The model is known as linear elastic traction-separation model in Abaqus. When using this model for cohesive elements, it relates the stress and strains across the interface. The stresses are the force components divided by the original area at each integration point, while strains are the separations divided by the thickness at each integration point. However, the default value of constitutive thickness is 1 (for any unit the Abaqus model is developed for) which is different from geometric thickness (which is typically close or equal to zero) and ensures that strain is equal to the separation (relative displacement of the top and bottom faces of cohesive element).

The input values of model includes interfacial stiffness, which defines the first elastic part of the LCFM behavior and maximum stress and displacement at failure as damage criteria which influences the peak value and the post peak slope. If interfacial stiffness, when multiplied by the thickness of the cohesive zone, be greater than the Young's modulus of the bulk material (here, rock), it will not affect the elastic properties. But it must still be small enough to avoid producing any traction oscillations (Borowski and Newell 2015).

It should be mentioned that, simulation of the fracture using cohesive elements requires substantial experience for determining the mesh requirement and accurate values of parameters which characterize the traction-separation law. For instance, the cohesive zone should have a finite thickness that is small relative to the elastic volume. Meanwhile, the simulation becomes unstable if extremely thin cohesive zone is considered.

12.3 User material subroutine

There is an option in Abaqus to define material properties as a function of field variables such as stress, stain or temperature. For this purpose, a subroutine should be written and linked into the Abaqus input file. In the subroutine, field variable and corresponding criteria are defined while in the input file different values of material properties (here, elastic modulus) corresponding to different field variables were inputted. In this study, two cases were considered. In the first case, the subroutine track the sign of pressure (mean stress) of each element and if it is negative, the field variable will be defined equal to 1 and if it is positive, it will be defined equal to 2. On the other side, in the input file, the compression elastic modulus is related to field variable of 2 and tensile elastic modulus is related to field variable of 1. In the second case, the same procedure would be done except that the maximum of absolute value of minimum and maximum principal stress ($\max(|S_{(principal,max)}|, |S_{(principal,min)}|)$) is considered instead of pressure.

12.4 Mesh Properties

Figure 12.1 shows the 3D Abaqus Finite Element Model (FEM) of the sample that exactly maps the Brazilian test experiment. The model geometry was selected based on the experimental data. In addition, each model was divided into sub-sections based on experimental layer identification and corresponding material properties were assigned to each layer. The cohesive

zone was defined as a 0.1 mm wide band in the center of disk with LCFM as the constitutive material. Trelis mesh generator (from Computational Simulation Software (csimsoft) LLC) was used for creating the geometry and the mesh, while 8 node linear brick elements, i.e. C3D8 and COH3D8, were used for the rock and cohesive elements, respectively. The mesh was considered to be finer in the vicinity of cohesive zone and gradually coarsens farther away from the cohesive zone in radial direction in order to decrease the computational cost. Convergence studies showed that the element sizes of 0.1 x 0.1 x 0.4 mm within the cohesive zone and using the bias ratio of 1.2 in x-direction is sufficient to capture the physics of the problem. The disk model was fixed in z direction at z=0 and loading was achieved by imposing a downward vertical displacement of 0.3 mm over 4 seconds to the two topmost set of nodes at the crown.
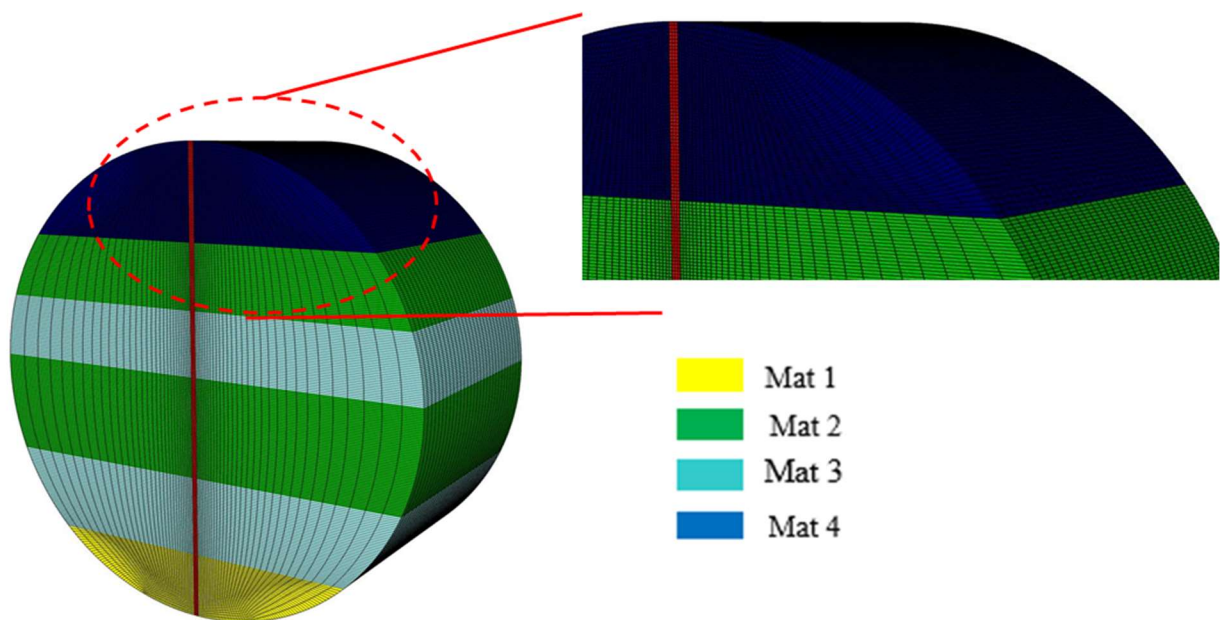
Figure 1212-1 Model geometry, layer and mesh configuration

12.5 Calibration of Material Models

Calibration of material model parameters for both rock and cohesive models were performed using experimental result of Brazilian test. The force-displacement graph was used for

this purpose and input values of material models were estimated so that the numerical results match the experimental ones. The maximum force can be converted into tensile stress using Equation 12.1.

In the first step, the model with an isotropic material was calibrated. Figure 12.2 shows the result of this calibration while Table 12.1 and 12.2 show the properties of material models. The experimental result was shifted into the left as the initial displacement measurements is related to the seating of loading plate, crack closure or other reasons. As it can be seen, the numerical model could predict the rock behavior pretty good both in the initial linear part and also at peak and post failure which proves the capability of models to represent the rock behavior during Brazilian test.
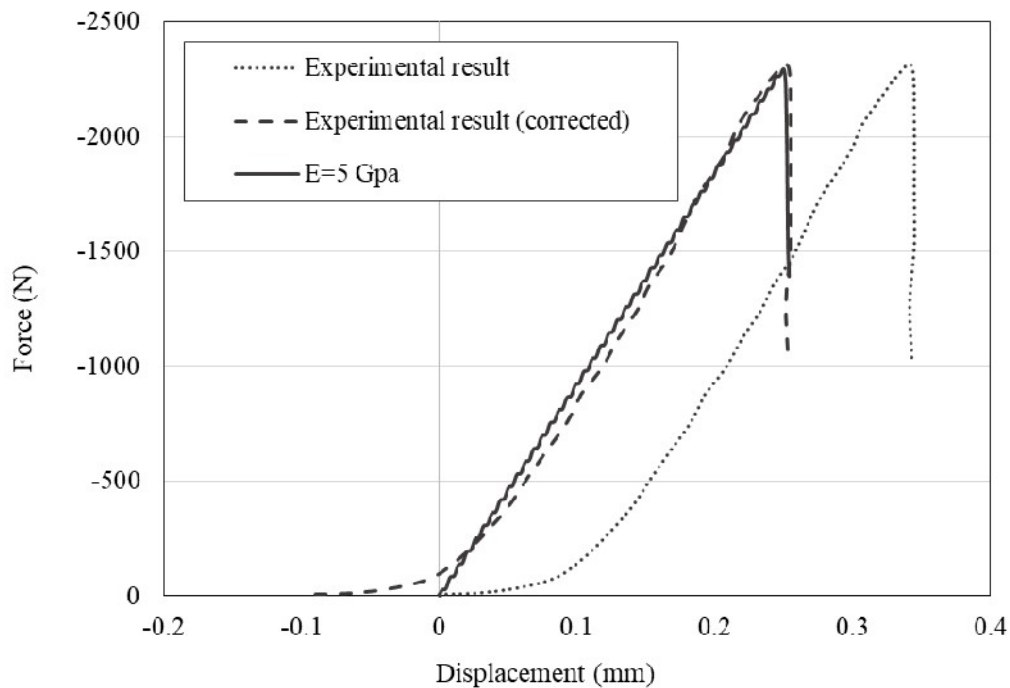
Figure 1212-2 Results of Brazilian test modeling of isotropic rock in comparison with experimental results

Table 12-1 Elastic model parameters for model of isotropic rock

Material	Elastic modulus (GPa)	Poisson ratio
Linear elastic model	5	0.18

Table 12-2 Material models parameters of cohesive model

Material	Interfacial stiffness (GPa)	Maximum stress (MPa)	Maximum displacement (mm)
Linear Softening Cohesive Model	50	4.65	0.045

In the second step, the isotropic model considering different layers in the sample was calibrated. As explained in section 3.3, elastic properties of each layer was estimated based on different material content of each layer based on the study by Sone and Zoback (2013) as presented in Table 12.2. A weighted average was calculated as an equivalent elastic modulus considering the area of each layer in the cross section using Equation 12.4. It should be mentioned that other formulas can be used for calculating the equivalent elastic modulus as well. Based on the calculations, the equivalent elastic modulus is 32 GPa which is high comparing to the estimated elastic modulus in calibration step 1 (5 GPa). This could be because the suggested values are based on data of rocks other than Mancos shale and may not be the best suggested values for it. In addition, these values are compression elastic modulus and so the tensile elastic modulus would be much lower. However in this step of study, one elastic modulus is considered for both tension and compression. Thus, the elastic modulus of all layers were scaled down by a ratio smaller than 1 in the numerical model to match the results with the experimental results. For these simulations, the properties of cohesive zone was considered the same as step 1 (Table 12.2). Thus, the scaling

ratio was the only calibrated parameter. Figure 12.3 shows the calibrated model while Table 12.3 summarizes the calibrated parameters. As presented in Table 12.3, the equivalent elastic modulus is 8.75 GPa which is higher than the value estimated in the first step (5 GPa).

$$E_{ave} = \frac{\Sigma\, A_i E_i}{\Sigma A_i} \approx 32\ GPa \qquad\qquad \text{Eq. 12-4}$$
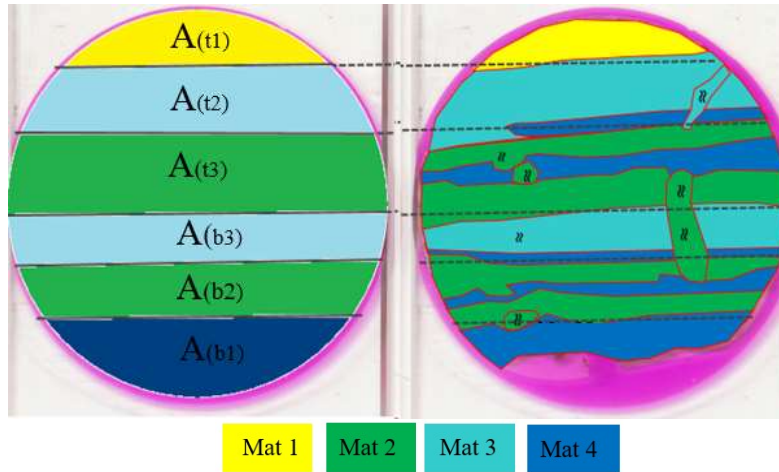
Figure 12-3 Area definition for different layers of rock sample
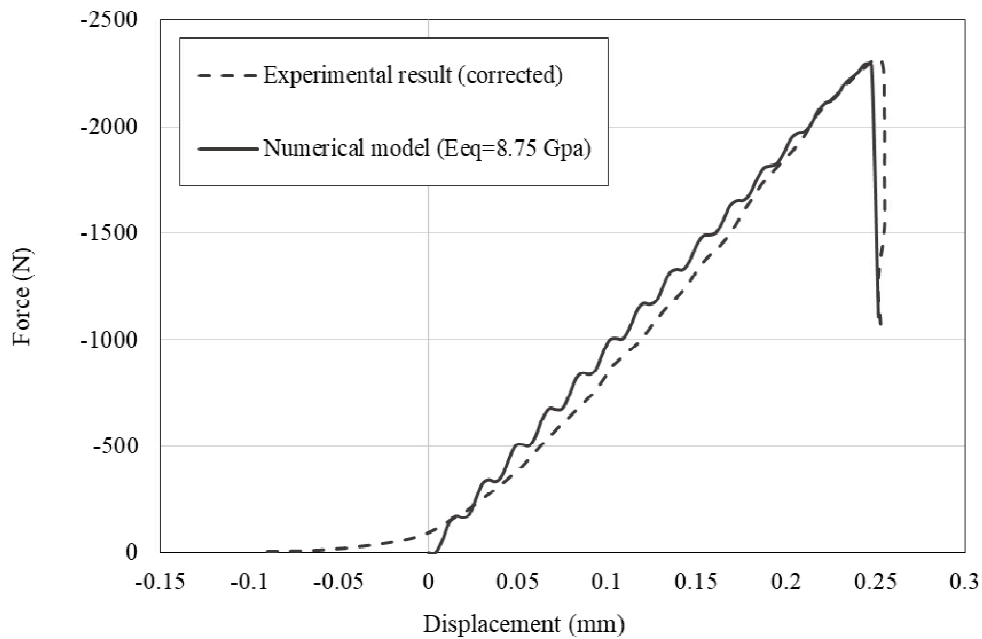
Figure 12-4 Results of Brazilian test modeling of rock with different layers in comparison with experimental results

Table 12-3 Elastic model parameters for model of rock with different layers

Material	Equivalent Elastic modulus (GPa)	Scaling ratio
Linear elastic model	8.75	0.272

It should be mentioned that the transversely isotropic material was not calibrated. The reason was that as explained in section 4.2.2, there are five independent elastic constant and more experimental data was needed to be able to calibrate all of these parameters. Instead, based on study by Mokhtari 2015, the suggested value of elastic modulus and Poisson's ratio in different directions for Mancos shale was used as an input of transversely isotropic material and results were compared with an isotropic model. Details of this simulation and the corresponding results are presented in section 4.6.e.

12.6 **Numerical Results**

In the following, the results of models with different compressive and tensile elastic modulus are presented. It includes isotropic model without layers (pressure dependent/ principal stress dependent) and isotropic model with layers (pressure dependent/ principal stress dependent). In addition, the results of transversely isotropic model is presented as well.

It should be mentioned that in the first two simulations the compressive elastic modulus was considered as 32 GPa. This value was the equivalent elastic modulus calculated for the sample based on the layer identification procedure as described in previous sections. Then, tensile elastic modulus was estimated 16 times smaller than compressive elastic modulus and equal to 2 GPa. This ratio is similar to the work by Borowski and Newell (2015) and is consistent with reported

$(\frac{E_{compresion}}{E_{tension}})$ ratio of 5-20 for different rocks as reported in the literature (Weinberger et al. 1994; Chamis et al).

12.6.1 Isotropic model with no layers and different elastic modulus with pressure criteria

Figure 12.5 shows the result of model with one isotropic rock (no layers) and compressive elastic modulus of 32 GPa and tensile elastic modulus of 2 Gpa. The criteria was the sign of pressure for each element. As it can be seen, the model responds with a high elastic modulus and small axial displacement at failure comparing to experimental results (about 5 times smaller) and the peak force is increased about 15% comparing to experimental vale as well.

Figure 12.6 shows the element pressure distribution while Figure 12.7 shows the field variable distribution in the model. Both figures show a consistent distribution. In black areas, pressure is negative and field variable is 1 while in blue areas, pressure is positive and field variable is 2. This proved that the subroutine and Abaqus model work appropriately together. In addition, as it can be seen in Figure 12.6, only a limited number of elements have negative pressure and so tensile elastic modulus of 2 GPa would be assigned to them and for the rest of the elements, the compression elastic modulus of 32 GPa would be assigned. Thus, the model response as shown in Figure 12.5 is reasonable.
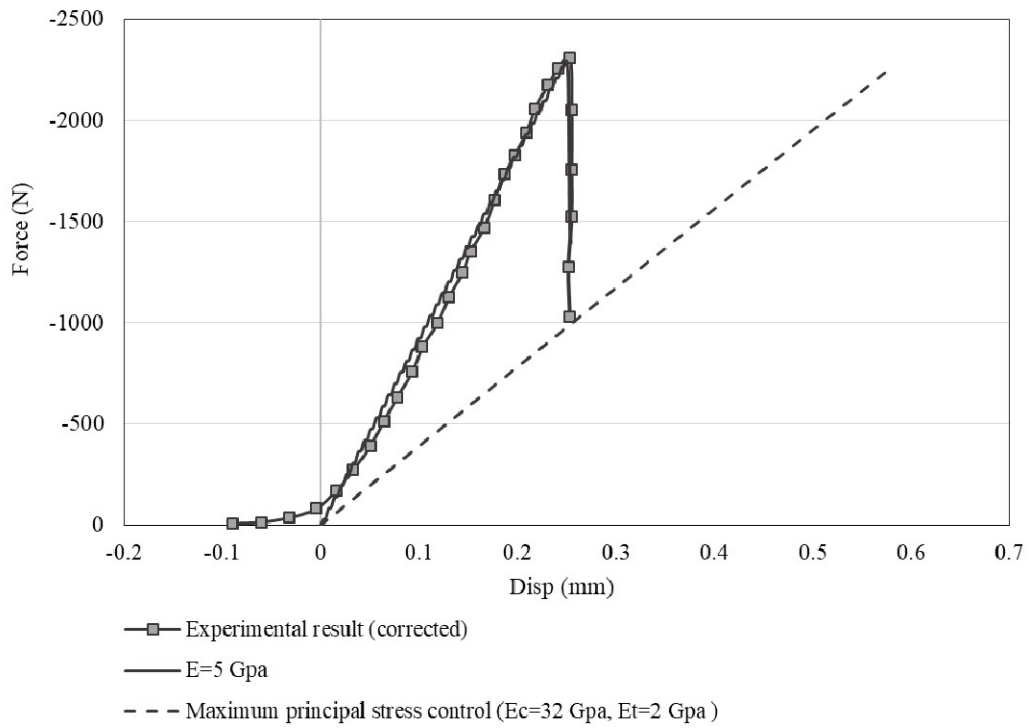
Figure 12-5 Result of model with different compressive and tensile elastic modulus in comparison with isotropic model with one elastic modulus and experimental results
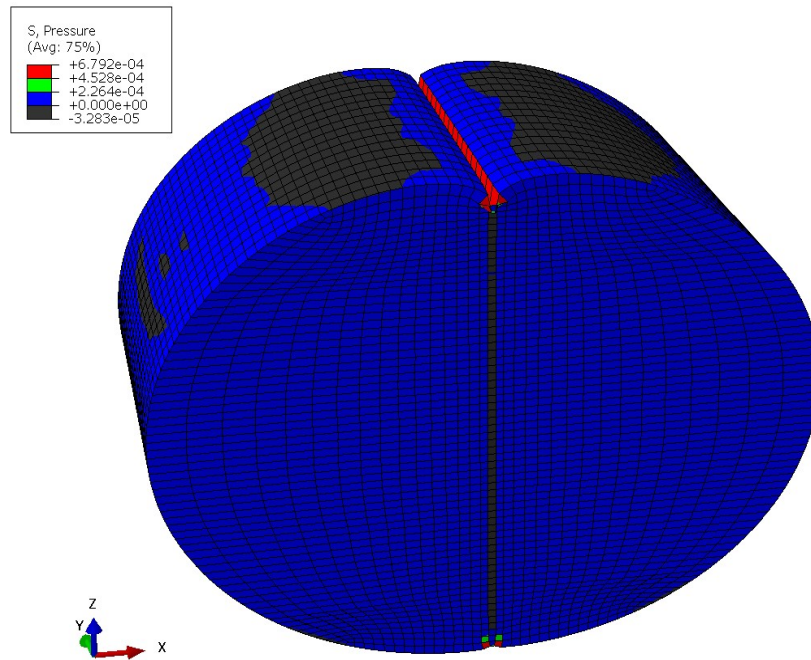
Figure 12-6 Areas of positive and negative pressure in isotropic model (no layering)
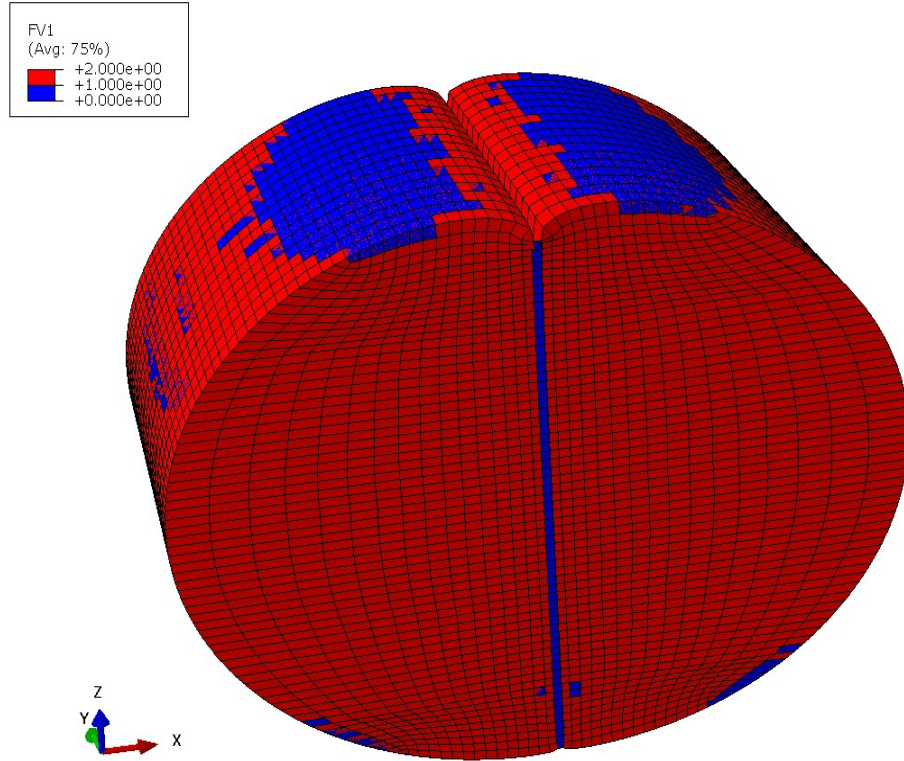
Figure 12-7 Field variable values for different elements

12.6.2 Isotropic model with no layers and different elastic modulus with principal stress criteria

Figure 12.8 shows the result of model with one isotropic rock and compressive elastic modulus of 32 GPa and tensile elastic modulus of 2 Gpa. The criteria is the sign of the maximum of absolute value of minimum and maximum principal stress $(\max(|S_{(principal,max)}|, |S_{(principal,min)}|))$. As it can be seen, model responds with a lower elastic modulus comparing to experimental results and larger axial displacement at failure (about 40% larger). However, the peak force is close to experimental one. Figures 12.9 and 12.10 show the maximum and minimum principal stress contours in the model while Figure 12.11 compares the pressure-dependent and principal stress-dependent models.

165
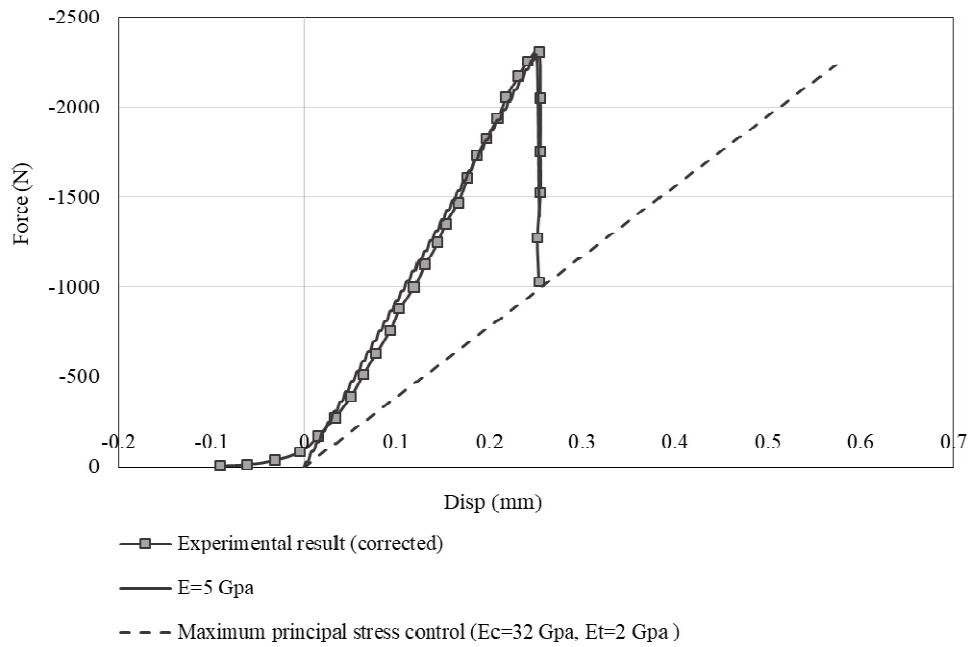
Figure 12-8 Result of model with different compressive and tensile elastic modulus (principal stress dependent) in comparison with isotropic model with one elastic modulus and experimental results
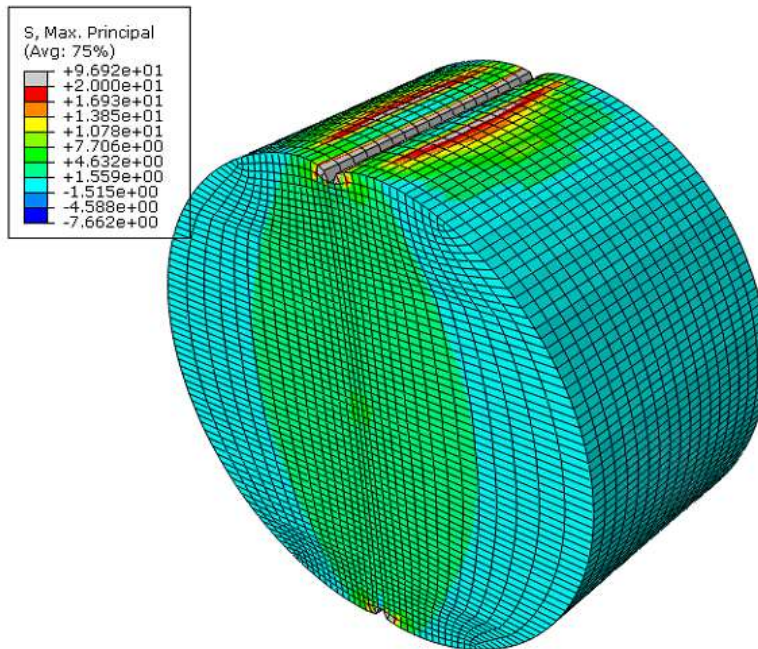
Figure 12-9 Maximum principal stress contour in isotropic model with different compressive and tensile elastic modulus (principal stress dependent)
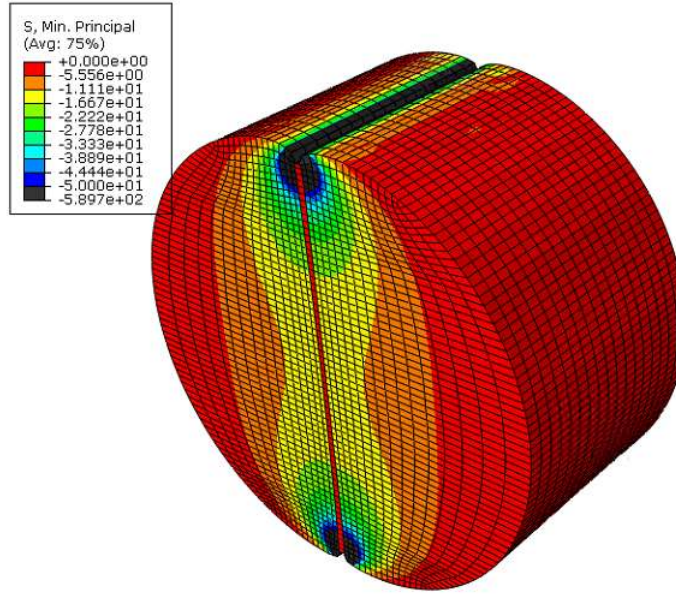
Figure 12-10 Minimum principal stress distribution in isotropic model with different compressive and tensile elastic modulus (principal stress dependent)
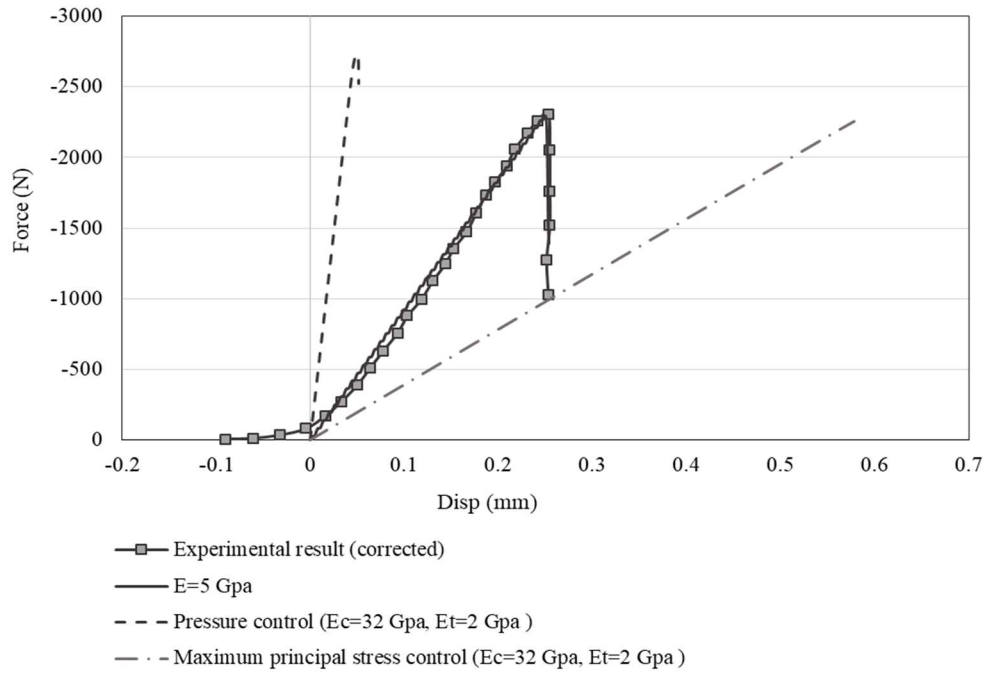
Figure 12-11 Result of model with different compressive and tensile elastic modulus (pressure dependent/principle stress dependent) in comparison with isotropic model with one elastic modulus and experimental results

12.6.3 Transversely isotropic model

For the case of transversely isotropic material, as explained before, the material properties were selected based on the work by Mokhtari (2015). In his study, the elastic modulus for vertical and horizontal samples (lamination angle (β) of 0 and 90 degree) were reported as 6.8 GPa and 9.7 GPa, respectively. Lamination angle is the angle between the loading direction and line normal to the bedding plane (figure 12.12). The in-plane and vertical Poisson's ratios were also estimated based on the stress- stain graph of compression test on samples with different lamination angles. This graph is presented in Figure 12.13. The other parameters were estimated using Equations presented in section 4.2.2. Table 12.4 summarizes the transversely isotropic material properties used in Abaqus model.
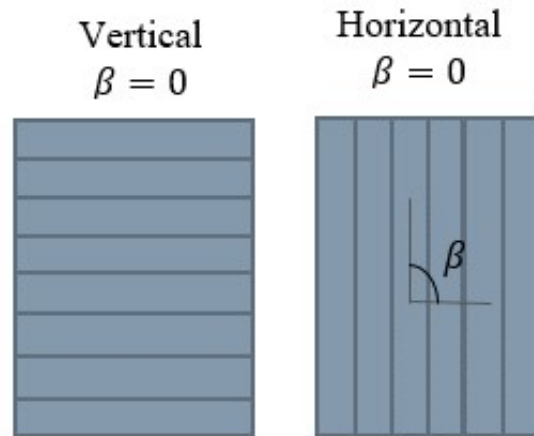
Figure 12-12 Lamination angle in Brazilian test samples (Mokhtari 2015)
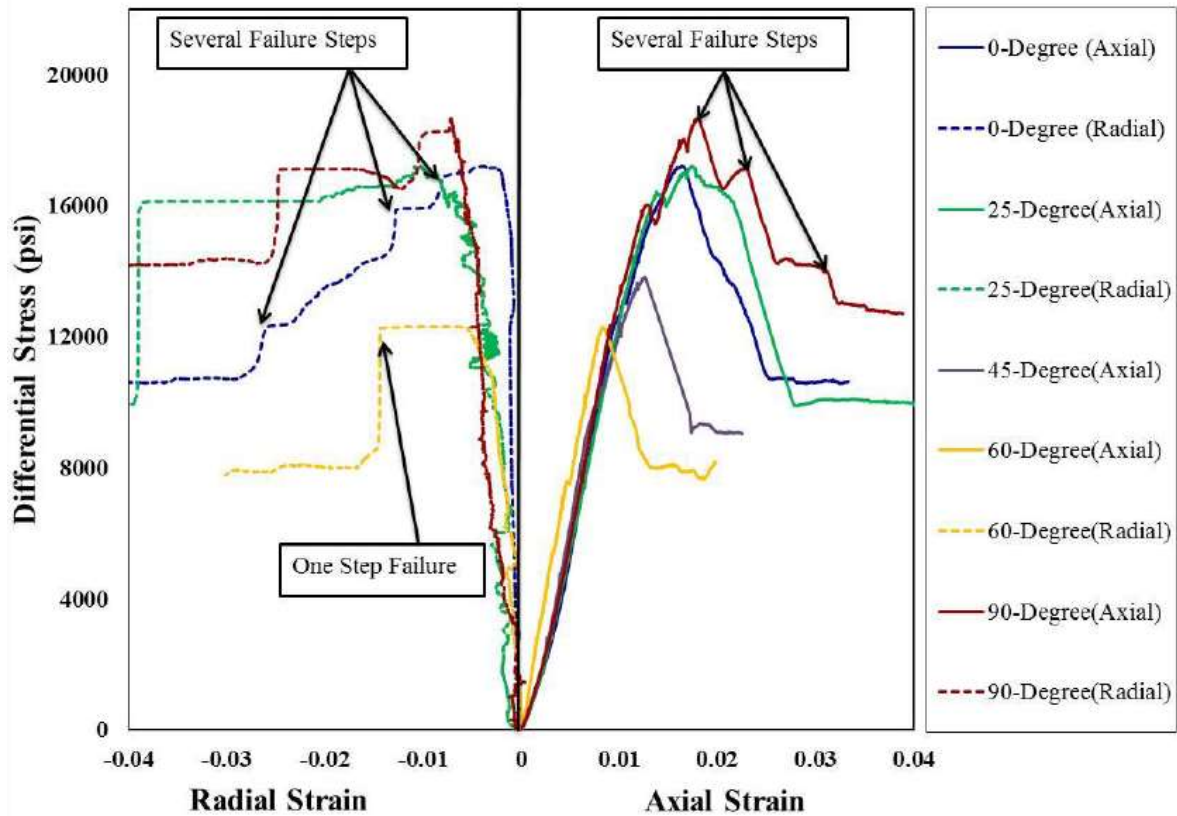
Figure 12-13 Mechanical behavior of Mancos shale samples with various lamination angle Mokhtari 2015)

Table 12-4 Transverse isotropic material model properties

Parameter	E_p (E_h)	E_z (E_v)	G_p	ν_p	ν_{zp}	G_{zp}	ν_{pz}
Value	9.7 GPa	6.8 GPa	3.23 GPa	0.45	0.13	3.47 GPa	0.185

In order to investigate the effect of considering transversely isotropic condition, an isotropic material was developed with an elastic modulus of 6.8 GPa (equal to E_c of transverse isotropic material) and results of that were used for comparison purpose. Figure 12.14 shows the results of these two models. As it can be seen, in both isotropic and transverse isotropic models, the maximum force is reached at a lower axial displacement. This was expected, as the calibrated elastic modulus was 5 GPa which is lower than elastic modulus values of these two models. In

addition, it can be seen that considering the transversely isotropic case causes both the slope and

the maximum force to be changed.
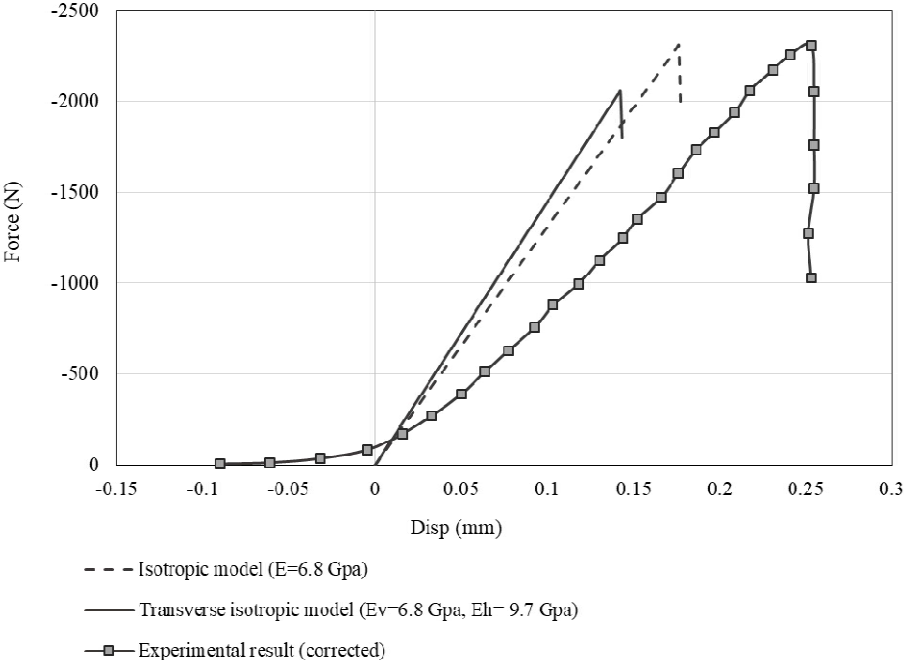
Figure 12-14 Results of Brazilian test modeling of transverse isotropic rock in comparison with experimental results

Chapter XIII

Brazilian Test on Shale Rock: Summary, Conclusion and Recommendation

13.1 Summary and conclusion

The objective of this study was to investigate the effect of considering different elastic modulus in compression and tension on rock fracture during Brazilian test. In addition, this effect was compared with the case of considering anisotropic material for rock. The capability of Linear Softening Cohesive Model (LCFM) in simulating rock fracture during Brazilian test was examined as well.

For this purpose, a finite element model was developed using Abaqus/Implicit and a user-material subroutine was adapted to change the elastic modulus of each element based on its stress state. Two criteria were defined as stress state of the element; pressure of each element and $\max(\left|S_{(principal,max)}\right|, \left|S_{(principal,min)}\right|$ of each element. Thus, based on each criteria, if the element was in tension, tensile elastic modulus was considered and if it was in compression, the compressive elastic modulus was considered.

The finite element model was calibrated based on experimental data of Brazilian test on the same rock sample and force- axial displacement graph was used for this purpose.

Results show that Linear Softening Cohesive Model (LCFM) is capable of simulating the Mancos shale fracture during Brazilian test and rock behavior in the elastic part, at failure and in post-failure were predicted well.

Results of pressure-dependent model and principal stress-model show that considering different compressive and tensile elastic modulus can make a huge difference in rock behavior. It can predict failure at 5 times less displacement or at 50% more displacement (for pressure-dependent and principal stress-dependent models respectively) and make 15% difference in the maximum force at failure (pressure-dependent model).

In addition, it can be concluded that the criteria considered to change the elastic modulus is a key component in the observed behavior. As mentioned, while pressure-dependent model overestimates the rock behavior, the principal stress-dependent model, underestimates the rock behavior.

Results of anisotropic model shows that considering the anisotropic condition can influence both the maximum force and displacement at failure as well.

13.2 Recommendations

A recommendation for future research would be to have a more completed experimental data base such as compression test and triaxial test. It helps to have a more reliable estimation of the rock properties and improves the calibration of numerical model. In this case, different ratios of $\frac{E_{compression}}{E_{tension}}$ could be tried and the most reasonable one be selected.

Another subject that needs to be explored is using other fracture models such as exponential softening fracture models and also other reasonable criteria such as von Mises for changing the elastic modulus for each element. In this study, two criteria were investigated; pressure and

principal stress. Other criteria could be considered as well. In addition, more complicated fracture models can be used instead of Linear Softening Cohesive Model (LCFM) to find the most capable one.

And finally, one interesting subject for future work could be modeling the rock as an anisotropic material and change the elastic modulus in each direction based on the element stress state in that direction. Of course, it needs a more completed experimental data base and would be challenging. However, it gives a much more accurate estimation of the rock behavior.

Chapter XIV

References

14.1 Cone Penetration in Unsaturated Soils

Abaqus-User's Manual- Version 6.13. Dassualt Systems Simulia Crop; 2013.

Alonso, E. E., Gens, A., & Josa, A. (1990). "Aconstitutive model for partially saturated soils." *Geotechnique,* **40**(3), 405-430.

American Petroleum Institute. (1993). Recommended practice for planning, designing and constructing fixed offshore platforms-working Stress Design. *20th edition API RP 2A-WSD, American petroleum Institute*, Washington D.C., 59-61.

Ahmadi, MM., Byrne, PM., & Campanella, RG. (2005). "Cone tip resistance in sand: modeling, verification and applications." *Can. Geotech J.*, **42**:977-993.

Arroyo, M., Butlanska J., Gens A., Calvetti F., & Jamiolkowski, M. (2011) "Cone penetration tests in a virtual calibration chamber." *Geotechnique*, 61(6): 525–531.

Baldi, G., Bellotti, R., Ghionna, V., Jamiolkowski, M., & Pasqualini, E. (1986). "Interpretation of CPTs and CPTUs; 2nd part: drained penetration of sands." *Proceeding of the Fourth International Geotechnical seminar,* Singapore, 143-156.

Bałachowski, L. (2007). "*Size effect in centrifuge cone penetration tests*". Archives of Hydro-Engineering and Environmental Mechanics, 54(3), 161-181.

Baldi, G., Bellotti, R., Ghionna, V., Jamiolkowski, M., Pasqualini, E. (1982). "Design parameters for sand from CPT." *Proceedings of the 2nd European symposium on penetration testing*, Amsterdam, the Netherlands, **2**:425–438.

Baldi, G., Bellotti, R., Ghionna, VN., Jamiolkowski, M. & Lo Presti, D.F.C. (1989). " Modulus of sands from CPTs and DMTs." *Proceedings of the 12th International Conference on Soil Mechanics and Foundation Engineering*, Rio de Janerio, **1**:165-170, Balkema Pub., Rotterdom.

Been, K., Crooks, JHA., Becker, DE. & Jefferies, MG. (1986). "The cone penetration test in sands: part I, state parameter interpretation." *Géotechnique*, **36(2)**:239–249, http://dx.doi.org/10.1680/geot.1986.36.2.239.

Bishop, AW. (1959). "The principle of effective stress." *Teknisk Ukeblad*, **106(39)**: 859–863.

Bolton, MD. (1986). 'The strength and dilatancy of sands." *Géotechnique*, **36(1)**: 65–78.

Bolton, MD., Gui, MW., Garnier, J., Corte, JF., Bagge, G., Laue, J. & Renzi, R. (1999). "Centrifuge cone penetration tests in sand." *Géotechnique,* **49(4)**:543-552

Butlanska, J., Arroyo, M., & Gens, A. (2010b). *"Virtual calibration chamber CPT tests on Ticino sand.".* In Proceedings of the 2nd International Symposium on Cone Penetration Testing, CPT' 10, pp. 217‑224.

Butlanska, J., Arroyo, M., Gens, A., & O'Sullivan C. (2014). 'Multi-scale analysis of cone penetration test (CPT) in a virtual calibration chamber." *Can. Geotech. J.*, 51:51-66.

Calvetti, F., & Nova R. (2005). "Micro-macro relationships from DEM simulated element and in-situ tests". *In Proceedings of Powders & Grains*, pp. 245‑250.

Collins, R., and Miller, G.A. (2014). *"Cone penetration testing in unsaturated soils at two Instrumented test sites."* In Proceedings of the 6th International Conference on Unsaturated Soils, UNSAT, Sydney, Australia, 2‑4 July. Balkema, Lisse, the Netherlands. Vol. 2, pp. 1489‑1494.

El-Sekelly, W., Abdoun, T., & Dobry, R. (2014). "The use of CPT and V s for assessment of saturated soil deposits in the centrifuge." In C. Gaudin, & D. White (Eds.), *Proceedings of the 8th international conference on physical modelling in geotechnics*.

Esquivel, E. R., & Ko, H. Y. (1994). "D*evelopment of a miniature piezocone*". In Proceedings of International Conference Centrifuge (Vol. 94, pp. 89-94).

Falagush, O., McDowell, G. R., & Hai-Sui, Yu. (2015). "Discrete element modeling of cone penetration tests incorporating particle shape and crushing." *Int. J. Geomech.,* 15(6): 04015003.

Geokon Instruction Manual (Model 4500 series-Vibrating Wire Pizeometer).

Ghayoomi, M., & McCartney, JS. (2011). "Measurement of the Small-Strain Shear Moduli of Partially-Saturated Sands During Infiltration in a Geotechnical Centrifuge." *Special Issue on Advances in Experimental Characterization of Unsaturated Soils Volume 1, ASTM Geotechnical Testing Journal*, **34(5)**:503-513.

Ghayoomi M, Wadsworth S. (2014). "*Renovation and reoperation of a geotechnical centrifuge at the university of new Hampshire*". In: Gaudin, White, editors. 8th international conference on physical modelling in geotechnics. Perth: CRC Press; p. 201–5.

Ghayoomi, M., Suprunenko, G., and Mirshekari, M. (2017) "Cyclic Triaxial Test to Measure Strain-Dependent Shear Modulus of Unsaturated Sand", *ASCE International Journal of Geomechanics,* (Accepted, In-Press).

Holmsgaard, R., Nielsen, B. N., & Ibsen, L. B. (2015). Interpretation of Cone Penetration Testing in Silty Soils Conducted under Partially Drained Conditions. *Journal of Geotechnical and Geoenvironmental Engineering,* 142(1), 04015064.

Hryciw, R. D., & Dowding, C. H. (1987). "Cone penetration of partially saturated sands." *Geotech. Test. J.*, **10(3)**:135–141.

Huang, A.B., & Ma M. Y. (1994). "An analytical study of cone penetration tests in granular material." *Can. Geotech. J.*, 31(1):91–103.

Huang, W., Sheng, D., Sloan, S. W., & Yu, H. S. (2004). "Finite element analysis of cone penetration in cohesionless soil." *Computers and Geotechnics,* 31(7), 517-528.

Jarast S. P., Ghayoomi M. (2016). "Simple numerical model to simulate penetration testing in unsaturated soils.". *3rd European conference on unsaturated soils*, Paris, France, In E3S Web of Conferences (Vol. 9, p. 08011). EDP Sciences.

Jarast, S. P., and Majid Ghayoomi (2017). "*Numerical Evaluation of the Effect of Unsaturated Soil above the Water Table on Cone Resistance*". In Geotechnical Frontiers 2017, pp. 623-632.

Jamiolkowski, M., Lo Presti, D. C. F., & Manassero, M. (2003). "Evaluation of relative density and shear strength of sands from CPT and DMT.". In *Soil behavior and soft ground construction* (pp. 201-238).

Jamiolkowski, M., Ladd, C.C., Germaine, J.T., & Lancelotta, R. (1985). "New developments in field and laboratory testing of soils". *Proceedings of 11th International Conference on Soil Mechanics and foundation engineering*, San Francisco, **1**:57-153.

Jiang, M., Yu, H. S., & Harris, D. (2006). "Discrete element modelling of deep penetration in granular soils." Int. J. Numer. Anal. Methods Geomech, 30(4): 335–361.

Keaveny, JM., & Mitchell, JK. (1986). "Strength of fine-grained soils using the piezocone.". In *Use of in situ tests in geotechnical engineering. American Society of Civil Engineers,* Reston, VA, **6**:668–685.

Kiousis, P.D., Voyiadjis, G.Z., Tumay, MT. (1988) "A large strain theory and its application in the analysis of the cone penetration mechanism." *International Journal for numerical and Analytical Methods in Geomechanics*, **12**:45-60.v

Kouretzis, G. P., Shang, D., Wang, D., (2014). "Numerical simulation of cone penetration testing using a new critical state constitutive model for sand.". *Computers and Geotechnics.* **56**: 50-60.

Kouretzis, G.P., Sheng, D., Wang, D. (2014) "Numerical simulation of CPT cone penetration in sand." *Applied Mechanics and Materials*, **553**:416-421.

Kulhawy, F.H., & Mayne, P.H. (1990), "Manual on estimating soil properties for foundation design." *Electric Power Research Institute, EPRI*, August,

Lee, S.Y. (1989), *centrifuge modelling of cone penetration testing in cohesionless soils,* Ph.D. Thesis, Cambridge university.

Lehane, B.M.,, Ismail, M.A., & Fahey, M. (2004). "Seasonal dependence of in situ test parameters in sand above the water table." *Geotechnique*, **54 (3)**:215-218.

Loret, B., & Khalili, N. (2002). "An effective stress elastic-plastic model for unsaturated porous media. *Mechanics of Materials,* **34(2)**:97-116.

Liu, Q. B., and B. M. Lehane (2012). "*The influence of particle shape on the (centrifuge) cone penetration test (CPT) end resistance in uniformly graded granular soils.*" Géotechnique 62, no. 11: 973

Lu, N., & Likos, W.J. (2006). "Suction stress characteristic curve for unsaturated soil." *J. Geotech. Geoenviron. Eng*., **132(2)**: 131-142.

Markauskas, D., kacianauskas, R., & Suksta, M. (2002). "Modeling the cone penetration test by the finite element method." *Foundation of civil and environmental engineering*, (2), 125-140.

Mayne, P.W. (1991). "Determination of OCR in clays by piezocone tests using cavity expansion and critical state concepts." *Soils and foundations*, **31(2)**:65-76

Mirshekari, M., & Ghayoomi, M. (2017). "Centrifuge tests to assess seismic site response of partially saturated sand layers." *Soil Dynamics and Earthquake Engineering*, 94, 254-265.

Nazem, M., Sheng, D., & Carter, JP. (2006). "Stress integration and mesh refinement for large deformation in geomechanics." *International Journal for Numerical Methods in Engineering*, **65**:1002-1027

Pournaghiazar, M., Russell, AR., & Khalili, N. (20011b) "Development of a new calibration chamber for conducting cone penetration testsin unsaturated soils." *Canad. Geotech. J.*, **48(2)**:314-321.

Pournaghiazar, M., Russell, A.R., & Khalili, N. (2012). "Linking cone penetration resistances measured in calibration chambers and the field." *Geotechnique Letters 2,* **2**:29-35.

Pournaghiazar, M., Russell, A.R., & Khalili, N. (2013). "The cone penetration test in unsaturated sands." *Geotechnique* **63(14)**:1209-1220.

Robertson, P.K., & Campanella, R.G. (1983a) "Interpretation of cone penetration tests, Part I: Sand." *Can. Geotech. J.,* **20(4)**:718–733.

Robertson, P.K. (2009). " Interpretation of cone penetration tests-a unified approach. " *Can Geotech J.,* **(46)**: 1337-55.

Roscoe, K.H., Burland, J.B. (1968) "On the generalised stress–strain behaviour of wet clay." In *Heyman, J., Leckie, F.A. (Eds.), Engineering Plasticity. Cambridge University Press*, Cambridge, pp. 535–609

Russell AR, Khalili N. A bonding surface plasticity model for sands exhibiting particle crushing. *Can. Geotech. J.* 2004; **41(6)**:1179-1192.

Russell AR, Khalili N. A unified bounding surface plasticity model for unsaturated soils. *Int. J. Numer. Analyt. Methods Geomech* 2006a; **30(3)**:181–212.

Russell, A.R., & Khalili, N. (2006b). "On the problem of cavity expansion in unsaturated soils." *Comput. Mech.,* **37(4)**:311-330.

Sharp, Michael K., Ricardo Dobry, and Ryan Phillips (2010). "*CPT-based evaluation of liquefaction and lateral spreading in centrifuge*". Journal of geotechnical and geoenvironmental engineering 136, no. 10: 1334-1346.

Sheng, D., Nazem, M., & Carter, J.P., (2009). "Some computational aspects for solving deep penetration problems in geomechanics." *Comput Mech*, **44**:549-561.

Silva, M. F., and M. D. Bolton (2004). "*Centrifuge penetration tests in saturated layered sands."* In Proceedings of 2nd International Conference on Site Characterization, vols, vol. 1, pp. 377-384. 2004.

Susila, E., & Hryciw, R.D., (2003) "Large displacement FEM modeling of the cone penetration test (CPT) in normally consolidated sand." *International Journal for Numerical and Analytical Methods in Geomechanics,* **27(7)**:585-602.

Vanapalli, S.K., Fathi, MO.M. (2013) "Bearing capacity and settlement of footings in unsaturated sands." *Int. J. of GEOMATE.*2013, **5(1)**:595-604.

Van den berg, P. (1994) "Analysis of soil penetration." Ph.D. thesis, Technische Universiteit Delf.

Yang, H., Russell, A.R., (2016). "Cone penetration tests in unsaturated silty sands." *Canadian Geotechnical Journal*, **53**:431-444.

Yi, J.T., Goh, S.H., Lee, F.H., & Randolph, M.F. (2012). A numerical study of cone penetration in fine-grained soils allowing for consolidation effects. *Géotechnique*, 62(8):707–719

Zhou, Y. G., T. Liang, Y. M. Chen, D. S. Ling, L. G. Kong, Y. Shamoto, and A. Ishikawa (2013). "*A two-dimensional miniature cone penetration test system for centrifuge modelling*". In ICPMG2014–Physical Modelling in Geotechnics: Proceedings of the 8th International Conference on Physical Modelling in Geotechnics 2014 (ICPMG2014), Perth, Australia, 14-17 January, p. 301. CRC Press, 2013.

14.2 Brazilian Test on Shale Rock

Barenblatt, G. I. (1962), The mathematical theory of equilibrium of cracks in brittle fracture, Adv. Appl. Mech., 7, 55–129.

Bažant, Z. P., and J. Plaňas (1997), Fracture and Size Effect in Concrete and Other Quasibrittle Materials, CRC Press, Boca Raton, Fla.

Boone, T. J., P. A. Wawrzynek, and A. R. Ingraffea (1986), Simulation of the fracture process in rock with application to hydrofracturing, Int. J. Rock Mech. Min. Sci. Geomechs. Abstr., 23(3), 255–265.

Borowski E., Newell P. (2015) Numerical investigation of fracture in geomaterials. Sandia National Labratories report (SAND2015-7325).

Cai M, Kaiser PK (2004) Numerical simulation of the Brazilian test and the tensile strength of anisotropic rocks and rocks with preexisting cracks. Int J Rock Mech Min Sci 41 (Suppl. 1):2B 03 01-06. doi:10.1016/j.ijrmms.2004.03.086

Chamis C. Analysis of the three-point-bend test for materials with unequal tension and compression properties. National Aeronautics and Space Administration, 1974.

Chen C-S, Pan E, Amadei B (1998) Determination of deformability and tensile strength of anisotropic rock using Brazilian tests. Int J Rock Mech Min Sci 35(1):43–61. doi:10.1016/s0148-9062(97) 00329-x

Chen S, Yue ZQ, Tham LG (2004a) Digital image-based numerical modeling method for prediction of inhomogeneous rock failure. Int J Rock Mech Min Sci 41(6):939–957

Chen S, Yue ZQ, Tham LG, Lee PKK (2004b) Modeling of the indirect tensile test for inhomogeneous granite using a digital image-based numerical method. Int J Rock Mech Min Sci 41 (Suppl. 1):2B 01 01-06.

Chen, Z., A. P. Bunger, X. Zhang, and R. G. Jeffrey (2009), Cohesive zone finite element-based modeling of hydraulic fractures, Acta Mech. Solida Sin., 22(5), 443–452.

csimsoft LLC, Trelis 6.0.

Dugdale, D. S. (1960), Yielding of steel sheets containing slits, J. Mech. Phys. Solids, 8, 100–108.

Exadaktylos GE, Kaklis KN (2001) Applications of an explicit solution for the transversely isotropic circular disc compressed diametrically. Int J Rock Mech Min Sci 38(2):227–243. doi: 10.1016/s1365-1609(00)00072-1.

Fairhurst C (1964) On the validity of the 'Brazilian' test for brittle materials. Int J Rock Mech Min Sci Geomech Abstr 1(4): 535–546. doi:10.1016/0148-9062(64)90060-9.

Fahimifar A., Malekpour M, (2012) Experimental and numerical analysis of indirect and direct tensile strength using fracture mechanics concepts. Bull Eng. Geol Envirom (2012) 71:269-283. doi 10.1007/s10064-011-0402-7.

Galvez JC, Cervenka J, Cendon DA, Saouma V. A discrete crack approach to normal/shear cracking of concrete. Cem Concr Res 2002;32:1567–85.

Gross, D., and T. Seelig (2011), Fracture Mechanics: With an Introduction to Micromechanics, 2nd ed., Springer, New York.

Gui Y., Bui H.H., Kodikara J. (2015), An application of a cohesive fracture model combining compression, tension and shear in soft rocks. Computers and Geotechnics 66: 142–157

Hillerborg, A., M. Modéer, and P. E. Petersson (1976), Analysis of crack formation and crack growth in concrete by means of fracture mechanics and finite elements, Cem. Concr. Res., 6, 773–782.

Jaeger, J. C., N. G. W. Cook, and R. Zimmerman (2007), Fundamentals of Rock Mechanics, 4th ed., Wiley-Blackwell, Malden, Mass.

Lanaro F, Sato T, Stephansson O (2009) Microcrack modelling of Brazilian tensile tests with the boundary element method. Int J Rock Mech Min Sci 46(3):450–461. Doi :10.1016/j.ijrmms.2008. 11.007

McCarty S, Newell P, (2015) Impact of Elastic Moduli in Tension and Compression in Geomaterials Sandia National Labratories report.

Mokhtari, M. (2015), Characterization of anisotropy in organic-rich Shale: shear and tensile failure, wave velocity, matrix and fracture permability. PhD thesis, Colordo School of mine.

Abdul Mwanga *, Jan Rosenkranz and Pertti Lamberg (2015), Testing of Ore Comminution behavior in the Geometallurgical Context—A Review, *Minerals*, *5*(2), 276-297

Perras, M. A., & Diederichs, M. S. (2014). A review of the tensile strength of rock: concepts and testing. Geotechnical and geological engineering, 32(2), 525-546.

Plaňas, J., M. Elices, G. V. Guinea, J. Gómez, D. A. Cendón, and I. Arbilla (2003), Generalizations and specializations of cohesive crack models, Eng. Fract. Mech., 70, 1759–1776.

Rinehart, AJ, JE Bishop, and T Dewers (2015), Fracture propagation in Indiana Limestone interpreted via linear softening cohesive fracture model. J. Geophys. Res. Solid Earth, 120, 2292–2308.

Rutqvsist, J., J. T. Birkholzer, and C. F. Tsang (2008), Coupled reservoir-geomechanical analysis of the potential for tensile and shear failure associate with CO_2 injection in multilayers reservoir-caprock systems, Int. J. Rock Mech. Min. Sci., 45, 132–143.

Rocco C, Guinea GV, Planas J, Elices M (1999a) Size effect and boundary conditions in the Brazilian test: Experimental verification. Mater Struct/Materiaux et Constructions 32(3):210–217.

Rocco C, Guinea GV, Planas J, Elices M (1999b) Size effect and boundary conditions in the Brazilian test: theoretical analysis. Mater Struct/Materiaux et Constructions 32(6):437–444

Rubin, A. M. (1993), Tensile fracture of rock at high confining pressure: Implications for dike propagation, J. Geophys. Res., 98(B9), 15,919–15,935, doi:10.1029/93JB01391.

Sone, H., & Zoback, M. D. (2013). Mechanical properties of shale-gas reservoir rocks—Part 1: Static and dynamic elastic properties and anisotropy. Geophysics.

Steen et al 2005

Timoshenko, Goodier (1990) Elastic theory (Xu Zhilun, Trans.). Higher Education Press, Beijing, 1:330.

Trelis FEA™ user's manual, 2016.

Thuro K, Plinninger RJ, Zah S, Schutz S (2001) Scale effects in rock strength properties. Part 1: unconfined compressive test and Brazilian test. In: Balkema AA (ed) Proceedings of the EUROCK 2001 Symposium. Rock Mechanics-A Challenge for Society, Rotterdam

Weinberger, R., Z. Reches, A. Eidelman, and T. E. Scott (1994), Tensile properties of rocks in four-point beam tests under confining pressure, in Rock Mechanics: Models and Measurements Challenges from Industry, edited by P. Nelson and S. E. Laubach, pp. 435–442, Balkema, Rotterdam, Germany.

Yao, Y. (2012), Linear elastic and cohesive fracture analysis to model hydraulic fracture in brittle rock and ductile rocks, Rock Mech. Rock Eng., 45, 375–387.

Yue ZQ, Chen S, Tham LG (2003) Finite element modeling of geomaterials using digital image processing. Comput Geotech 30(5):375–397